



**Max-Planck-Institut für Metallforschung**  
Stuttgart

---

**Deposition of Metal Oxide Thin Films  
from Solutions Containing Organic Additives**

Peter Lipowsky

Dissertation  
an der  
**Universität Stuttgart**

---

Bericht Nr. 204  
September 2007



**Deposition of Metal Oxide Thin Films  
from Solutions Containing Organic Additives**

**Dissertation**

Von der Fakultät Chemie der Universität Stuttgart

zur Erlangung der Würde eines

Doktors der Naturwissenschaften (Dr. rer. nat.)

genehmigte Abhandlung

Vorgelegt von

**Peter Lipowsky**

geboren in Erlangen

Hauptberichter : Prof. Dr. rer. nat. Fritz Aldinger

Mitberichter : Priv.-Doz. Dr. rer. nat. habil. Joachim Bill

Tag der mündlichen Prüfung : 24. September 2007

Institut für Nichtmetallische Anorganische Materialien der Universität Stuttgart

Max-Planck-Institut für Metallforschung, Stuttgart

Pulvermetallurgisches Laboratorium

Stuttgart, 2007



## Abstract

In bio-inspired materials synthesis the principles of biomineralization are employed for the fabrication of materials with favourable functional properties at near-ambient temperature and with little expenditure: Organic templates direct the formation of inorganic matter. In aqueous solution, zinc compounds with manifold morphologies are produced by thermal hydrolysis of zinc nitrate in the presence of biomolecules like amino acids and dipeptides. In methanol, ZnO films are deposited by hydrolysis of zinc acetate in the presence of polymers like polyvinylpyrrolidone (PVP) and polyethylene glycol. With PVP, particularly smooth, uniform and stable films are fabricated. Their thickness is determined by the deposition time and the polymer concentration. Various microscopic and spectroscopic measurements prove that the films consist of textured nanocrystalline zinc oxide. Selected properties of the films, such as their photoluminescence, are investigated. Film deposition is possible on substrates with organic coatings bearing certain functional groups. Patterned films can be deposited after local decomposition of the organic coating by UV light. The mechanism of film formation is treated in detail. Like in biomineralization, an amorphous transient state of matter occurs before crystallization. This state succumbs to ZnO nanocrystals, which either aggregate in solution or adsorb to the substrate. It is demonstrated in what way the additive controls the reaction. Sulfonate-modified polystyrene beads are coated with zinc oxide and used as sacrificial templates for the fabrication of zinc oxide hollow spheres. Laminates of alternating layers of zinc oxide and poly(amino acids) are deposited and exhibit an improved mechanical performance compared to the monolithic zinc oxide.



---

## Index of contents

1.	<b>Introduction and overview</b>	11
1.1	Motivation	11
1.2	Scope of the work	12
2.	<b>Mineralization from aqueous solutions of zinc salts directed by amino acids and peptides</b>	17
2.1	Introduction	19
2.2	Experimental	20
2.2.1	Substrate preparation	20
2.2.2	Deposition experiments	20
2.2.3	Film characterization	21
2.3	Results and discussion	22
2.4	Conclusions	37
2.5	Acknowledgements	37
3.	<b>Thin film formation by oriented attachment of polymer-capped nanocrystalline ZnO</b>	39
3.1	Introduction	41
3.2	Experimental	42
3.2.1	Preparation of the deposition solutions	42
3.2.2	Substrate preparation and film deposition	44
3.2.3	Film characterization	44
3.3	Results and discussion	45
3.4	Conclusions	54
3.5	Acknowledgements	54
4.	<b>Site-selective deposition of nanostructured ZnO thin films from solutions containing polyvinylpyrrolidone</b>	57
4.1	Introduction	59
4.2	Results and discussion	60
4.2.1	Film growth and morphology	60
4.2.2	Patterning	65
4.2.3	Composition	66
4.2.4	Microstructure and texture	68
4.2.5	Optical properties	71

---

4.2.6	Deposition mechanism	74
4.3	Conclusions	74
4.4	Experimental	75
4.4.1	Substrate preparation and patterning	75
4.4.2	Deposition solution and deposition	76
4.4.3	Sample characterization	77
4.5	Acknowledgements	78
5.	<b>Time evolution of zinc oxide particle formation and assembly of oriented nanocrystalline films in methanol</b>	81
5.1	Introduction	83
5.2	Experimental	85
5.2.1	Substrate preparation, deposition solution and deposition	85
5.2.2	Sample characterization	86
5.3	Results and discussion	88
5.3.1	Three stages of particle formation	88
5.3.2	Initial stage at room temperature	90
5.3.3	Intermediate stage after heating-up to 60 °C	92
5.3.4	Final stage	94
5.3.5	Composition of the particles in solution	96
5.3.6	Interactions of PVP with ions, particles and aggregates	97
5.3.7	Influence of the substrate on the film deposition	100
5.3.8	Influence of the polymer on the film deposition	101
5.3.9	Deposition kinetics	102
5.3.10	Influence of the molecular weight of the polymer	103
5.4	Conclusion	104
5.5	Acknowledgements	107
6.	<b>Zinc oxide microcapsules obtained via a bio-inspired approach</b>	109
6.1	Introduction	111
6.2	Experimental	112
6.2.1	Templates	112
6.2.2	Precursor solution	113
6.2.3	ZnO coating	113
6.2.4	Removal of the polymer templates	114
6.2.5	Sample characterization	114



---

6.3	Results	115
6.4	Discussion and outlook	119
6.5	Acknowledgements	120
7.	<b>Laminates of zinc oxide and poly(amino acid) layers with enhanced mechanical performance</b>	123
7.1	Introduction	125
7.2	Experimental section	125
7.3	Results and discussion	129
7.4	Conclusion	136
7.5	Acknowledgements	136
8.	<b>Kurzfassung der Dissertation</b>	139
8.1	Einleitung und Überblick	139
8.2	Von Aminosäuren und Dipeptiden gesteuerte Mineralisation in wässrigen Zinksalzlösungen	140
8.3	Schichtbildung durch orientierte Anlagerung von mit Polyvinylpyrrolidon überzogenen Zinkoxid-Nanokristallen	142
8.4	Ortsselektive Abscheidung von nanostrukturierten Zinkoxid-Dünnschichten aus polyvinylpyrrolidonhaltigen Lösungen	143
8.5	Zeitliche Entwicklung der Bildung von Zinkoxidteilchen und des Aufwachsens orientierter nanokristalliner Schichten in Methanol	145
8.6	Nach einer bioinspirierten Methode hergestellte Zinkoxid-Mikrokapseln	148
8.7	Laminate aus Zinkoxid- und Polyamino säurenschichten mit verbesserten mechanischen Eigenschaften	149
	<b>References</b>	153
	Curriculum vitae	163
	Danksagung	165



## **Publication of the individual chapters in scientific journals**

The present thesis has a cumulative structure, i. e. the individual chapters are independent papers which have been published in scientific journals or which are designated for publication in scientific journals.

### **Chapter 2: “Mineralization from aqueous solutions of zinc salts directed by amino acids and peptides”**

*Peter Gerstel, Rudolf C. Hoffmann, Peter Lipowsky, Lars P. H. Jeurgens, Joachim Bill, Fritz Aldinger*  
Chemistry of Materials **2006**, *18*, 179.

### **Chapter 3: “Thin film formation by oriented attachment of polymer-capped nanocrystalline ZnO”**

*Peter Lipowsky, Shijun Jia, Rudolf C. Hoffmann, Neng Yun Jin-Phillipp, Joachim Bill, Manfred Rühle*  
International Journal of Materials Research **2006**, *97*, 607.

### **Chapter 4: “Site-selective deposition of nanostructured ZnO thin films from solutions containing polyvinylpyrrolidone”**

*Peter Lipowsky, Rudolf C. Hoffmann, Udo Welzel, Joachim Bill, Fritz Aldinger*  
Advanced Functional Materials, **2007**, *17*, 2151.

### **Chapter 5: “Time evolution of zinc oxide particle formation and assembly of oriented nanocrystalline films in methanol”**

*Peter Lipowsky, Niklas Hedin, Joachim Bill, Rudolf C. Hoffmann, Anwar Abniyaz, Fritz Aldinger, Lennart Bergström*  
Journal of Physical Chemistry C, *submitted*. (The present thesis contains a preliminary version.)

### **Chapter 6: “Zinc oxide microcapsules obtained via a bio-inspired approach”**

*Peter Lipowsky, Michael Hirscher, Rudolf C. Hoffmann, Joachim Bill, Fritz Aldinger*  
Nanotechnology **2007**, *18*, 165603.

### **Chapter 7: “Laminates of zinc oxide and poly(amino acid) layers with enhanced mechanical performance”**

*Peter Lipowsky, Žaklina Burghard, Lars P. H. Jeurgens, Joachim Bill, Fritz Aldinger*  
Nanotechnology **2007**, *18*, 345707.



# 1. Introduction and overview

## 1.1 Motivation

Traditional ways of synthesizing ceramic materials are, for example, sintering, molecular beam epitaxy, plasma spraying, physical and chemical vapour deposition, polymer thermolysis, and sol-gel processes. [1] All these processes require either high energies or complex equipment permitting the application of high temperatures and very high or very low pressures, which makes them costly. Except for the polymer thermolysis, these methods can only be used for the fabrication of thin films on planar surfaces or of bulk items with simple geometries, so that subsequent machining is indispensable. It is obvious that there is a demand for procedures of materials synthesis which can, on the one hand, be realized at near-ambient conditions, i. e. low temperature, and which permit, on the other hand, the production of materials with a higher degree of complexity. Nature teaches us how to reconcile these two requests: Biominerals like nacre, bone or enamel are formed at the body temperature of the organisms producing them, which is more or less equivalent to ambient temperature. [2,3] At the same time biominerals show very favourable material properties. An outstanding example is nacre (mother-of-pearl), whose main constituent is calcium carbonate. Because of its specialized structure it is both harder and tougher than pure calcium carbonate. Nacre consists of calcium carbonate platelets with a diameter of a few micrometers and a thickness of a few hundred nanometers, which are embedded in a matrix of proteins. [4] When cleaved, the protein “sheets” between the platelets divert the crack, and much higher forces must be applied to break the sample. The protein matrix also plays a crucial role in the formation of nacre.

Bio-inspired materials synthesis is an attempt to adopt the principles of biomineralization in order to exploit its advantages for the production of synthetic materials, [5] preferably materials which do not occur in nature, but can be used for special applications. The aim of the bio-inspired approach is to realize materials synthesis with little expenditure and at low costs. The process should be efficient and environmentally friendly, and it should permit the production of materials with superior properties for manifold applications. Bio-inspired materials synthesis is conducted at temperatures below 100 °C, and at ambient pressure. Thus even temperature-sensitive substrates can be coated. Nature shows that organic templates are essential for the formation of biominerals. [6,7] The bio-inspired method adopts these principles: Inorganic minerals are deposited on organic substrates, and organic additives are dissolved in the deposition solution in order to control the process. [8]

When a bio-inspired process for the formation of an oxidic coating on a substrate is realized, [9] one may start with a support, for example a silicon wafer or a glass slide. The support is coated with an organic layer, which is modified by functional groups, and which serves as the substrate for deposition. The substrate is immersed in a solution containing a precursor for the desired target material. When the system is adjusted to its specific reaction conditions, ions or particles from solution begin to assemble on the substrate, and gradually a film of a ceramic material is formed, which can be dried and supplied to investigations or applications subsequently.

Chemical bath deposition (CBD) is a method for the deposition of thin films of metal compounds, in which the principles of bio-inspired materials synthesis can be implemented. CBD was first developed for the deposition of chalcogenides like CdS [10] and CdSe, [11] and later it was also applied to transition metal oxides such as ZnO. [12] In a CBD process, a substrate is immersed in a solution of a metal salt and a chalcogenide source, possibly containing further additives to direct structure formation, and a film is formed on the substrate without any redox reactions taking place. [13]

Zinc oxide is a material for which the development of a bio-inspired route for its synthesis appears profitable. Zinc oxide is a semiconductor with favourable and useful electrical and optical properties. An overview of the properties and their possible applications, including references to relevant literature, is given in the introduction to Chapter 4 of this work. Due to the variety of applications, and as bulk single-crystalline ZnO is expensive and only available in small quantities, the fabrication of both thin coatings and nanostructures of zinc oxide has attracted much interest. Achieving the synthesis of this promising material with a low-cost and low-effort method applying the principles of bio-inspired materials synthesis seems a rewarding challenge.

## 1.2 Scope of the work

In the present work, methods for the chemical bath deposition of zinc oxide in the presence of organic additives are developed. The properties of the resulting films are investigated and optimized. Both the deposition products and the deposition solutions are studied in order to elucidate the deposition mechanism, with special emphasis on the question how the additives control the process. Attempts to exploit the process for applications and to further enhance the versatility of the films are presented.

Chapter 2 of this work gives an impression of the multitude of products which can be obtained from zinc containing precursor solutions. In particular, experiments with the deposition of

zinc compounds from aqueous solutions containing amino acids or dipeptides are presented. Some additives have little effect and do not prevent the growth of micron-sized, hexagonal ZnO crystals; others induce the formation of nanostructures consisting of amorphous ZnO or layered basic zinc salts (LBZ). Beside smooth uniform thin films, a vast variety of morphologies is obtained, among them ribbon-like structures, sheet stacks, and spongy structures.

The effects of other additives such as synthetic polymers and sugars are tested in Chapter 3, and instead of water, different kinds of alcohols are used as solvents in order to slow down the reaction and make control of the process easier. It is shown that polyvinylpyrrolidone (PVP) is the most promising candidate for inducing the deposition of smooth ZnO films on self-assembled monolayers (SAM) of alkylsiloxanes. The composition and microstructure of the films deposited in the presence of PVP are investigated in detail. Based on the results of the study, it is suggested that oriented attachment of the crystallites plays a major role in film formation.

In Chapter 4, an optimized deposition process is presented, which takes place in a PVP solution in methanol. The parameters of the process are varied, and their influence on the deposition product is demonstrated. The microstructure and properties of the films are investigated, and it is shown that particularly smooth and thick nanocrystalline ZnO films with a texture can be obtained when the deposition conditions are optimized. Deposition occurs only on SAM-modified substrates. This is exploited for the fabrication of laterally structured films by deposition on a substrate carrying a SAM which was partially disintegrated by UV light.

The mechanism and the kinetics of the deposition of ZnO films from methanolic solutions containing PVP are discussed in Chapter 5 as well as analogies to biomineralization processes. The processes in solution are investigated extensively since it was recognized that detailed knowledge about them is indispensable for understanding the deposition mechanism. An intermediate state of amorphous spicular particles acting as a reservoir of zinc ions is reported, and it is clarified in what way the polymer influences the reactions. The PVP induces the formation of the intermediate particles, controls their dissolution and promotes the aggregation of the finally forming ZnO nanocrystals both towards films on the substrate and towards aggregates in solution. The competition between the various processes explains the differences of the deposits obtained at different PVP concentrations.

The Chapters 6 and 7 of this work show how the deposition of the ZnO films can be enhanced towards possible future applications. Chapter 6 deals with the fabrication of hollow spheres of zinc oxide applying a sacrificial template route, i. e. a zinc oxide film is deposited on polystyrene microspheres with a sulfonate-modified surface, and the polystyrene core is finally removed by thermal disintegration in an oven or by dissolution in a solvent.

Chapter 7 comprises an attempt to improve the mechanical properties of the ZnO films by mimicking the microstructure of nacre. Stacks of alternating layers of organic material and zinc oxide are deposited. The organic interlayers consist of polyelectrolytes and poly(amino acids). Compared to monolithic films of a similar thickness, the composite films exhibit an improved mechanical performance.







**2. Mineralization from aqueous solutions of zinc salts  
directed by amino acids and peptides**

## **Abstract**

The suitability of amino acids and dipeptides as structure-directing agents for the deposition of coatings from aqueous solutions of zinc salts is discussed. According to a bio-inspired approach the influence of these biomolecules was investigated with respect to the evolution of architectures based on zinc oxide and basic zinc salts. The small molecules were able to trigger the morphology of these materials ranging from grain-like via two up to three-dimensional features. Besides morphological aspects the structural characterization of these solids by means of electron and atomic force microscopy, by photoelectron and infrared spectroscopy, and X-ray diffraction are discussed in order to extract the function of the biomolecules with regard to the formation of the inorganic phases.

## 2.1 Introduction

Zinc oxide and zinc oxide-based materials or devices are promising candidates for several functional applications such as UV light emitters, gas sensors or acoustic wave devices, which accounts for many attempts to miniaturization and nanostructuring. [14,15] As an alternative and complement to conventional routes for the deposition of thin films the method of chemical bath deposition (CBD) was introduced. [16] CBD here refers to the thermohydrolysis (or “forced hydrolysis”) of metal salts for the fabrication of oxidic films. However, in the case of zinc oxide the deposition behaviour is strongly influenced by the tendency to form elongated micron-long crystals (sometimes termed “nanorods”) that made the formation of smooth homogeneous nanostructures so far impossible. [16,17] Recently, the preparation of zinc oxide-based nanostructured films without these insufficiencies was reported. [18,19] The applied method involved macromolecular organic additives like graft copolymers [18] or homopolymers, [19] which are added to the deposition medium. Owing to the interaction of these polymers with zinc oxide in solution the growth of micron-sized crystals is suppressed and organic/inorganic hybrid nanoparticles are formed within the deposition solution. The subsequent assembly of these particles can be controlled by organically modified surfaces and yields nanostructured films with luminescent properties. [19]

The interaction of organic molecules with inorganic phases is also observed in living nature, e. g. in the case of biomineralization processes that lead to the formation of complex organic/inorganic structures. [20] Furthermore, there are examples, where metal ions interact with bioorganic molecules. In this connection, amino acids like histidine are involved, e. g. within the so-called zinc finger, a configuration of a DNA-binding protein. [21] Accordingly, a large number of zinc complexes with amino acid ligands were investigated, [22] which might be suitable starting materials for solid state structures.

In the present paper the hydrolysis of zinc salts in the presence of amino acids and dipeptides was investigated, whereby the suitability of such organic molecules as structure-directing agents was revealed. The main aim was to demonstrate that this bio-inspired approach provides a means for the deposition of a variety of morphologies ranging from grain-like via two- up to three- dimensional features.

---

## 2.2 Experimental

### 2.2.1 Substrate preparation

Substrates consisted of surface oxidized silicon, whereby further modification with layer-by-layer assemblies (LBLs) of polyelectrolytes was also employed. Deposition experiments were carried out on both types of surfaces.

Silicon wafers were cleaned and surface oxidized in Piranha solution [conc.  $\text{H}_2\text{SO}_4 : \text{H}_2\text{O}_2$  (30 wt.-% in water) = 70 : 30, v:v], washed abundantly with distilled water and dried in an argon stream prior to use. LBLs of polyelectrolytes were prepared, if applied in the deposition experiment, by dipping the silicon wafer in an aqueous 0.5 weight-% solution of the desired polyelectrolyte for 20 minutes, followed by immersion in distilled water for 5 minutes. Subsequent layers were obtained without intermediate drying between the immersions in oppositely charged polyelectrolytes according to published procedures. [23] Aqueous polyelectrolyte solutions were obtained from commercially available products by dilution with water (Polyethyleneimine - PEI (Aldrich,  $M_r = 70\,000$ ); Poly(sodium 4-styrenesulfonate) - PS (Aldrich,  $M_r = 70\,000$ ) and Poly(allylamine hydrochloride) - PAH (Aldrich,  $M_r = 70\,000$ )). The pH of the PEI solution was adjusted to 3 with hydrochloric acid, PS and PAH solutions were used without further conditioning. All LBLs in this work had the sequence (PEI/PSS)(PAH/PSS)<sub>7</sub>.

### 2.2.2 Deposition experiments

Several series of deposition experiments were carried out with zinc nitrate and hexamethylenetetramine (HMTA) concentrations in the reaction solution of either 15 or 30 mM, respectively, with a constant ratio of  $[\text{Zn}] : [\text{HMTA}]$  of 1 : 1 but varying ratios of amino acids or dipeptides. The stereo configuration of all amino acids including those in dipeptides was L in all cases. To ensure optically clear starting solutions all compounds were mixed always freshly prior to use. Therefore amino acids or peptides were dissolved in an HMTA stock solution and mixed with according volumes of a zinc nitrate solution to obtain the above-mentioned concentrations.

Substrates were immersed in 2 ml aliquots of the reaction solution at 343 K until the onset of visible turbidity in the case of His and Gly-His. Longer reaction times did not lead to significantly thicker films and larger agglomerates from the solution sedimented on the substrate. In the case of  $[\text{Zn}] = 15$  mM turbidity was observed after 4.5 h for  $[\text{Zn}] : [\text{His}] = 1 : 1$ , 5.5 h for  $[\text{Zn}] : [\text{His}] = 2 : 1$ , 6.5 h for  $[\text{Zn}] : [\text{His}] = 4 : 1$  and 3.5 h for  $[\text{Zn}] : [\text{Gly-His}] = 2 : 1$ , respective-

ly. In the case of  $[\text{Zn}] : [\text{His}] = 8 : 1$  no turbidity was observed till the termination of the reaction after 6.75 h. Depositions with all other amino acids or peptides were carried out for 48 hours at 333 K.

For comparison of the before-mentioned films from His-containing solutions with a reference substance,  $\text{Zn}(\text{His})_2$  powder was synthesized [24] and compacted to pellets.

### 2.2.3 Film characterization

*X-ray photoelectron spectroscopy (XPS):* XPS analysis was performed with a Thermo VG Theta-probe 300 system using monochromatic incident Al  $K\alpha$  radiation ( $h\nu = 1486.68$  eV; spot size 400  $\mu\text{m}$ ; base pressure  $< 10^{-7}$  Pa; average detection angle of  $53^\circ$  with respect to the sample surface). Energy calibration, removal of contaminations and charge compensation during the measurements were carried out according to established procedures. [25] Spectral decomposition of the as-measured spectra was performed by subtraction of a Shirley-type inelastic background over the concerned binding energy (BE) range for each spectral region, and subsequent, constrained, linear-least-squares fitting with one or more symmetric (mixed Gaussian-Lorentzian) peak components (while taking the same Gaussian-Lorentzian fraction and full-width-at-half-maximum (FWHM) for each component in the fitted spectrum). Finally, the BE scales for each set of resolved Zn 2p were aligned by shifting the spectra according to the difference between the resolved, lowest-BE oxidic Zn  $2p_{3/2}$  main peak and the corresponding reference value of  $1021.9 \pm 0.1$  eV for pure ZnO, [26] whereby this approach also lead to reasonable values for the accordingly shifted set of O 1s, N 1s and C 1s signals. In the spectra recorded from the  $\text{Zn}(\text{His})_2$  reference, the oxidic Zn  $2p_{3/2}$  peak corresponding to the chemical environment of Zn in ZnO is absent and the alignment of the BE-scales was done by shifting the resolved Zn  $2p_{3/2}$  main peak to the value of  $1027.8 \pm 0.1$  eV as determined above. This approach also lead to reasonable values for the binding energies of the lighter elements and the contributions to the C 1s, O 1s and N 1s peaks could be determined in a curve-fitting procedure.

*Atomic force microscopy (AFM):* Images were recorded using a Digital Instruments Nanoscope III applying tapping mode with silicon cantilevers.

*Scanning electron microscopy (SEM):* Micrographs were taken with a Zeiss DSM 982 Gemini at 1.7 kV or a Jeol 6300F at 2 kV.

*X-ray diffraction (XRD):* Diagrams were measured with a Siemens D5000 Kristalloflex diffractometer in Bragg-Brentano geometry using Cu  $K\alpha 1$  radiation.

*Infrared spectroscopy (IR):* Samples were obtained by collecting deposition products from several wafers, mixing with KBr and compaction to pellets. Transmission spectra were measured using a Nicolet Avatar 360.

*Zeta potential measurements:* A Zetasizer Malvern 3000 HSA was used to measure the electrophoretic mobility. Measurements were carried out for reaction solutions from 30 mM [Zn], 30 mM HMTA and 30 mM His after the onset of turbidity, which showed a potential of +22.0 mV at pH 6.7. To improve the reliability, a series of three separate measurements (298 K) was collected.

### 2.3 Results and discussion

The addition of glycyl-glutamine (Gly-Gln), citrulline (Cit) and proline (Pro) lead to the formation of micrometer-sized crystals, presumably multiple twins of zincite (Figure 2.1). Such twinning of zincite was found to be typical for precipitation in the presence of additives containing carboxylate functions. [27] A control experiment without the addition of biomolecules, though, yielded a similar precipitate consisting of hexagonal crystals of zincite. This might indicate a rather weak interaction of the above-mentioned amino acids and dipeptides with the mineralization product in comparison to the other employed additives.

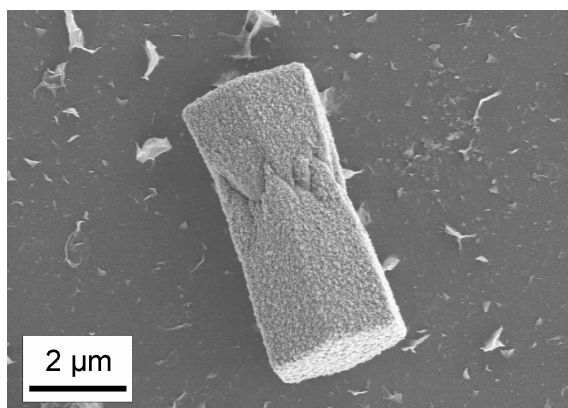


Figure 2.1: SEM micrograph of zincite from solutions containing 30 mM [Zn], 30 mM HMTA and 3.75 mM Pro.

In the presence of histidine (His) or glycyl-histidine (Gly-His) films were formed, whereby SEM micrographs revealed a complete and uniform surface coverage for low [Zn] : [His] ratios (Figure 2.2a-c). Below a threshold concentration of His, though, the deposition of larger colloids



instead of film formation was observed (Figure 2.2d). The cross sections of the interference coloured films exhibited a thickness between 160 (Figure 2.2a), 140 (Figure 2.2b) and 50 nm (Figure 2.2c). As indicated by these SEM investigations and moreover according to AFM measurements the ratio of roughness to thickness of the films increased with higher  $[\text{Zn}] : [\text{His}]$  ratios (Figure 2.3), suggesting that the presence of histidine minimizes the tendency of zinc oxide to form larger, elongated crystals. This corresponds to earlier investigations in which graft copolymers were used to inhibit the growth of zincite microcrystals and stabilize nanoparticles for uniform film growth. [16,17]

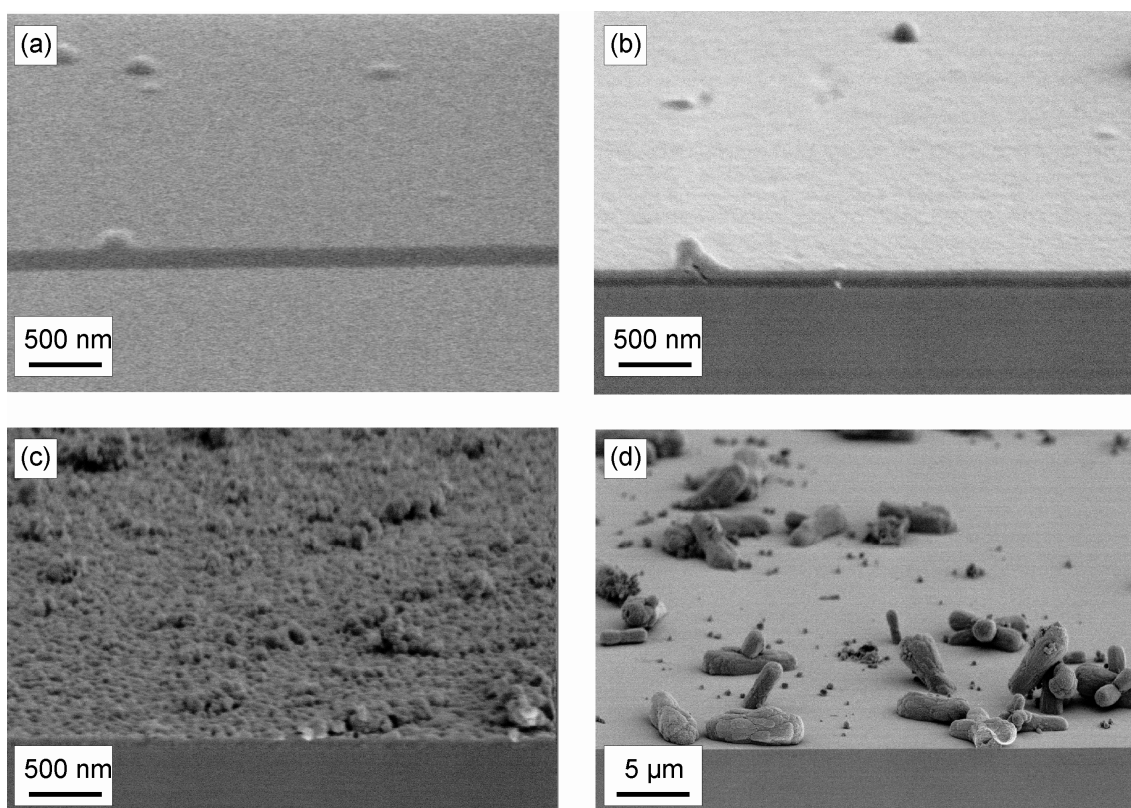


Figure 2.2: SEM micrographs of as-deposited films grown on silicon from solutions containing 15 mM  $[\text{Zn}]$ , 15 mM HMTA and various amounts of His at 343 K (reaction time): (a)  $[\text{Zn}] : [\text{His}] = 1 : 1$  (4.5 h), (b)  $[\text{Zn}] : [\text{His}] = 2 : 1$  (5.5 h), (c)  $[\text{Zn}] : [\text{His}] = 4 : 1$  (6.5 h) and (d)  $[\text{Zn}] : [\text{His}] = 8 : 1$  (6.75 h).

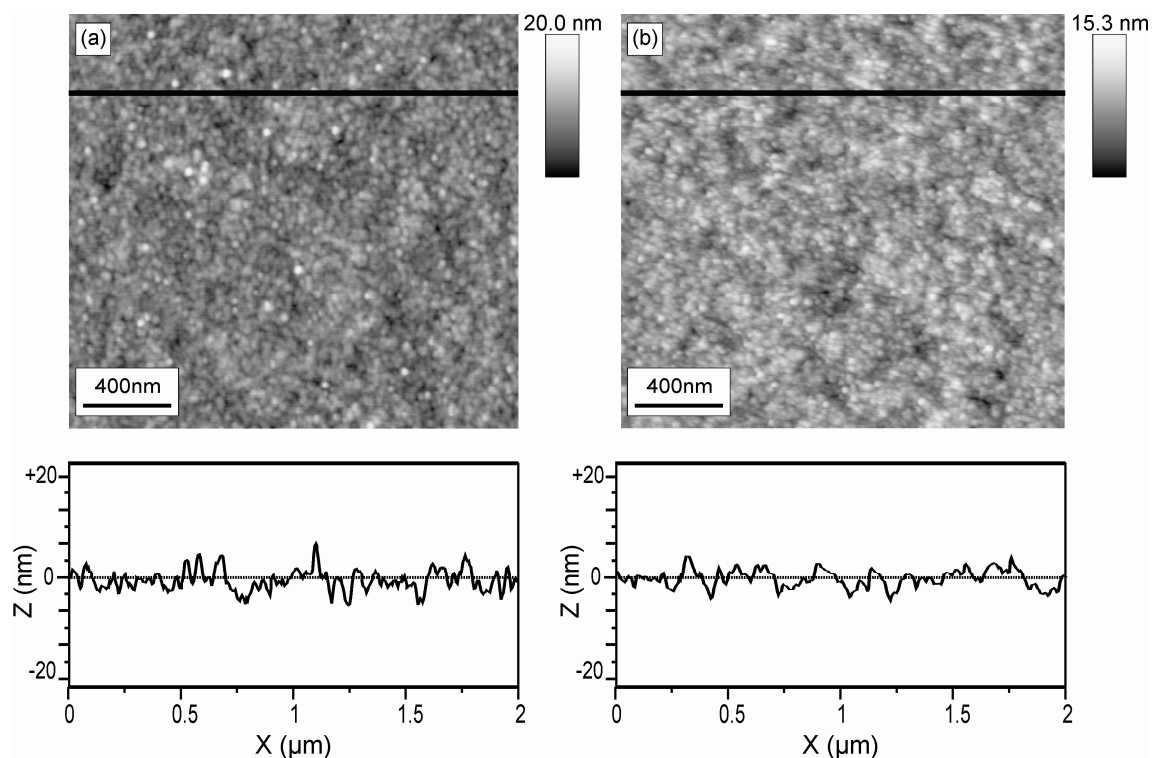


Figure 2.3: AFM images and cross sections of as-deposited films grown on silicon from solutions containing 15 mM [Zn], 15 mM HMTA and various amounts of His at 343 K: (a) [Zn] : [His] = 1 : 1 (RMS 2.0 nm); (b) [Zn] : [His] = 2 : 1 (RMS 1.7 nm). The reaction conditions correspond to the samples in Figure 2.2a-b.

XPS was applied to investigate the effect of the organic additives His and Gly-His in the reaction solution on the chemical constitution of the resulting thin films (Figures 2.4 and 2.5). To this end, detailed spectra of the Zn 2p, O 1s, N 1s and C 1s photoelectron lines, as well as survey spectra over a wide BE range from 0 to 1400 eV, were recorded for films obtained from reaction solutions containing His and Gly-His. To establish the chemical states of the constituent atoms in the oxide products, the different spectral components constituting the measured Zn 2p<sub>3/2</sub>, C 1s, O 1s and N 1s spectra were resolved by constrained peak-fitting. The BE values of the thus resolved peak components are reported in Tables 2.1 and 2.2. For all cases studied, the XPS analysis indicated the presence of Zn, C, O and N within the formed products (for an example see Figure 2.4), thereby confirming the incorporation of amino acids in the films for all cases studied.

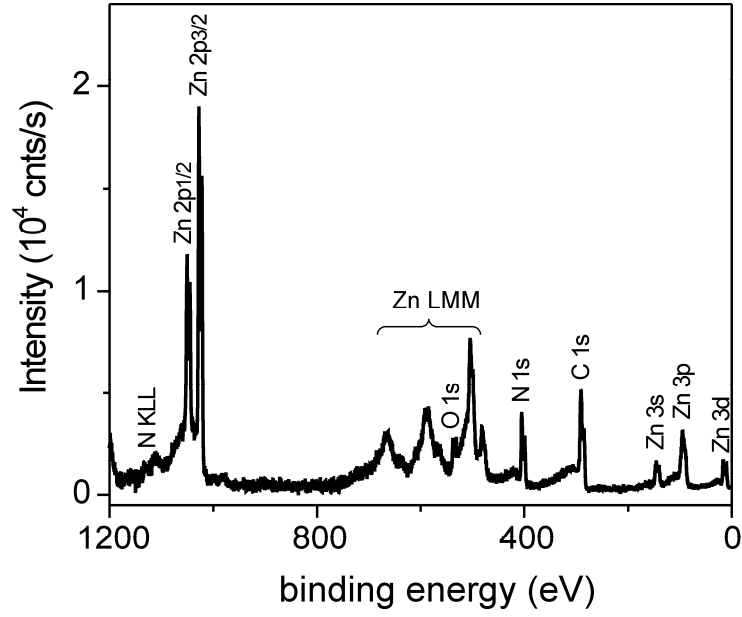


Figure 2.4: XPS spectrum (after charge correction and subtraction of a universal Tougaard background) recorded from an as-deposited oxide film grown on silicon from a solution containing 15 mM [Zn], 15 mM HMTA and 15 mM His. The different photoelectron and Auger lines originating from the various oxide-film constituents are indicated.

	additive	Zn 2p <sub>3/2</sub> BE [eV]			
(a)	Zn:His 2:1	1021.9	1024.1		
(b)	Zn:His 1:1	1021.9	1023.9	1025.8	1027.8
(c)	Zn:Gly-His 2:1	1021.9	1023.6	1025.1	
(d)	Zn(His) <sub>2</sub>		1023.3	1025.4	1027.8

Table 2.1: Binding energies (BE; in eV) of the Zn 2p<sub>3/2</sub> peak components as resolved by constrained peak fitting of the charge-corrected XPS spectra of the prepared oxide films. The estimated error in the determination of the BE positions is about 0.2 eV.

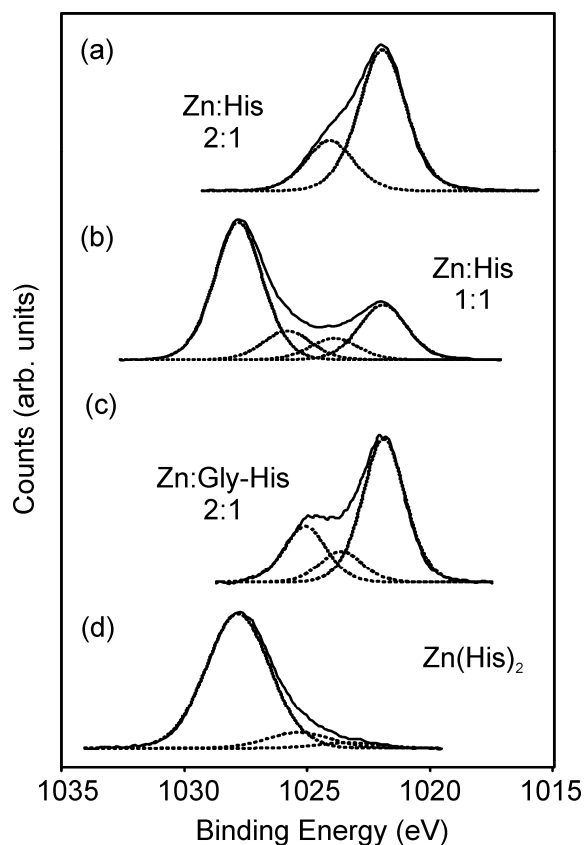


Figure 2.5: XPS spectra of the as-deposited films from solutions containing (a) 15 mM [Zn], 15 mM HMTA and 7.5 mM His; (b) 15 mM [Zn], 15 mM HMTA and 15 mM His; (c) 15 mM [Zn], 15 mM HMTA and 7.5 mM Gly-His; and (d) spectrum of the  $\text{Zn}(\text{His})_2$  reference for comparison.

The measured Zn  $2p_{3/2}$  spectra could be accurately fitted with up to four different peak components (Figure 2.5). The resolved Zn  $2p_{3/2}$  peak positioned at the lowest BE of  $1021.9 \pm 0.1$  eV corresponds to Zn in crystalline ZnO (Figure 2.5a-c; see also Ref. [26]). After comparison with the corresponding  $\text{Zn}(\text{His})_2$  reference spectrum (compare Figure 2.5b with Figure 2.5d), the resolved Zn  $2p_{3/2}$  peak component at the highest BE position of  $1027.8 \pm 0.2$  eV could be identified with the local chemical environment for Zn atoms in the mononuclear complex  $\text{Zn}(\text{His})_2$  (as characterized by Zn atoms tetrahedrally surrounded by the oxygen atoms of two carboxylate groups [24,28]). This BE value of  $1027.8 \pm 0.2$  eV can be compared with the corresponding BE value of 1027.0 eV, as reported for zinc acetate. [29] As reflected by comparison of Figures 2.5a and 2.5b, an increasing His concentration in the reaction solution results in a relative increase of Zn atoms being incorporated as  $\text{Zn}(\text{His})_2$  in the developing oxide film. Accordingly, a decrease of the His concentration results in an increasing contribution of ZnO to the reaction product. In addition to the two aforementioned main components, up to two relatively weaker components with intermediate BE values of  $1025.5 \pm 0.4$  eV and  $1023.6 \pm$

0.5 eV (i.e. between that for Zn in ZnO and Zn in Zn(His)<sub>2</sub>; see Table 2.1) were resolved from the measured Zn 2p<sub>3/2</sub> spectra. These components were less well-defined, which indicated the presence of Zn ions in a mixed environment.

	additive	C 1s BE (eV)			O 1s BE (eV)			N 1s BE (eV)		
(a)	Zn:His 2:1	284.7	287		531.5	533.7		398.9	401.1	
(b)	Zn:His 1:1	285.3		290.5	531.2	534.0	537.2	399.0	402.3	404.8
(c)	Zn:Gly-His 2:1	284.6	286.7	288.7	531.6	534.7		399.0	401.8	
(d)	Zn(His) <sub>2</sub>			290.6		534.5	537.7		402.1	404.7

Table 2.2: Binding energies (BE; in eV) of the C 1s, O 1s and N 1s peak components (corresponding with the resolved Zn 2p<sub>3/2</sub> peak components in Table 2.1) as resolved by constrained peak fitting of the charge-corrected XPS spectra of the prepared oxide films. The estimated error in the determination of the BE positions is about 0.2 eV.

Other amino acids or peptides, which were investigated for the use as additives, lead to more complex morphologies. The addition of tryptophyl-glycine (Trp-Gly) caused the formation of rather opaque films, which showed sponge-like shapes (Figure 2.6). Remarkably a hierarchical organization of the surface morphology was built up in this self-assembly process. Whereas hemispherical features existed on a micrometer scale (Figure 2.6a-b), also explicit structuring was observed in the nanometer regime (Figure 2.6c). This particular morphology resembles the multiple roughness structure of self-cleaning surfaces, which can be found for example in the water repellent leaves of *Colocasia esculenta* or *Nelumbo nucifera*. [30,31] Accordingly the coated surfaces obtained with Trp-Gly as additive show superhydrophobicity with a contact angle of  $165 \pm 5^\circ$  (Figure 2.6d).

The employment of arginine (Arg) resulted in the formation of deposits consisting of layers of nanoscale platelets (Figure 2.7a), resembling the nacreous plate structure in seashells. In the case of all the before-mentioned amino acids or dipeptides (Figures 2.1, 2.2 and 2.6), the deposits or coatings exhibited the same morphology with or without LBL modification of the silicon substrate. From reaction solutions containing glycyl-glutamic acid (Gly-Glu), however, ribbon-like morphologies were found (Figure 2.7b) on LBL-modified substrates, whereas no significant deposition occurred on unmodified surface oxidized silicon (Figure 2.7c). This is the only, yet most interesting, example in this work where a difference between LBL modified and unmodified substrates was found.

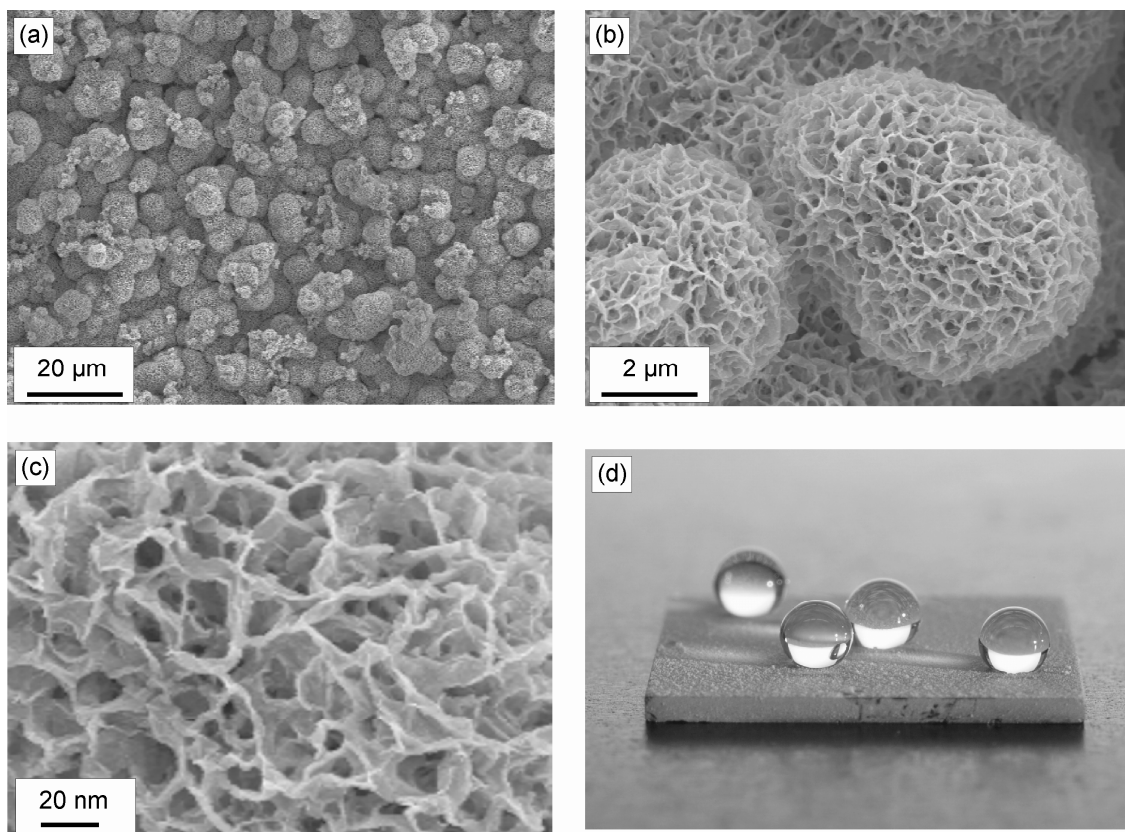


Figure 2.6: (a)-(c) SEM micrographs of deposition products grown on polyelectrolyte multilayers from solutions containing 30 mM [Zn], 30 mM HMTA and 7.5 mM Trp-Gly for 48 h at 333 K. The different magnifications reveal the hierarchical structure of the film. (d): Water droplets on the coated substrate (1x1 cm<sup>2</sup>).

Further characterization of the deposition products obtained from the reaction solutions containing Trp-Gly, Arg and Gly-Glu was carried out by means of XRD measurements (Figure 2.8). The X-Ray patterns had features typical of incompletely ordered lamellar compounds related to the brucite structure, which revealed the presence of layered basic zinc salts (LBZs). LBZs possess a specific layered structure that could be determined by structure analysis of  $Zn_5(OH)_8A_2 \cdot n H_2O$  for  $A = Cl^-$  [32] and  $NO_3^-$  [32] or  $Zn_5(OH)_6(CO_3)_2$ . [33] The structure is best described in terms of  $[(Zn_{octa})_3(Zn_{tetra})_2(OH)_8]^{2+} \cdot 2 (A^-) \cdot n H_2O$  and consists of infinite brucite layers, where one quarter of the zinc atoms in the octahedral interstices are omitted. On both sides of the empty octahedra Zn atoms are located that are tetrahedrally coordinated. Thus the ratio of octahedral to tetrahedral zinc is 3:2. In the case of the monovalent anions  $A^-$  the tetrahedral zinc sites are coordinated by three  $OH^-$  ions of the brucite layers. The fourth apex of these coordination tetrahedra point into the interlayer space and can then be occupied either by the anion (for  $Cl^-$  or  $CO_3^{2-}$ ) or by a water molecule, whereby the anion is freely situated in the interlayer (in the case of  $NO_3^-$ ). [32,33,34]

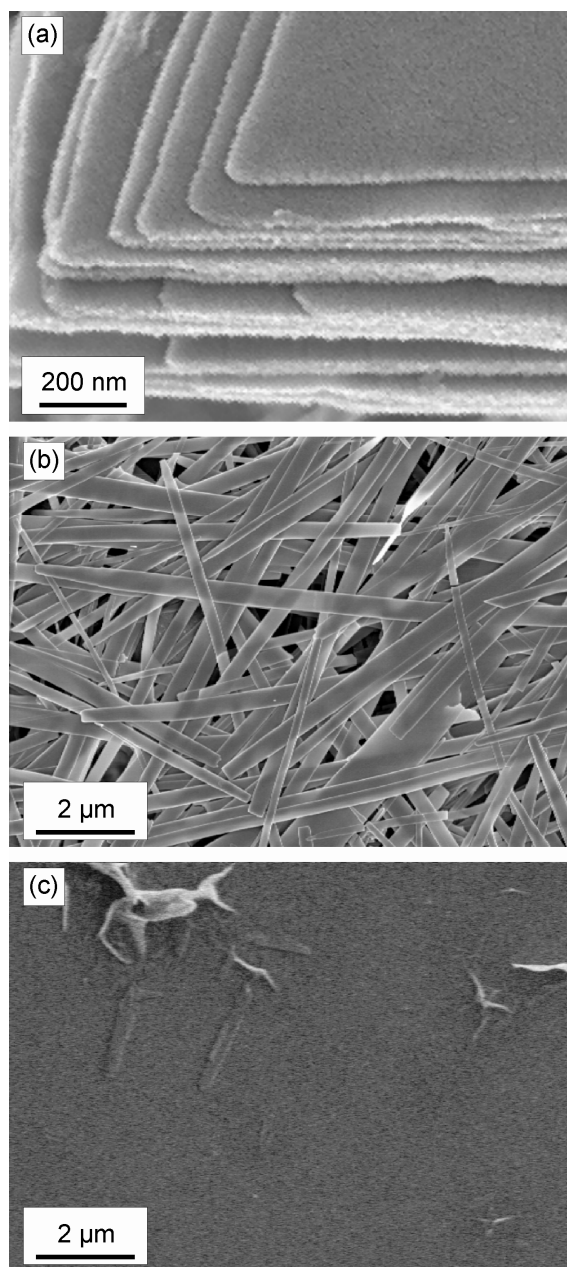


Figure 2.7: SEM micrographs of deposition products grown on polyelectrolyte multilayers from solutions containing (a) 30 mM [Zn], 30 mM HMTA and 3.75 mM Arg, (b) 15 mM [Zn], 15 mM HMTA and 1.88 mM Gly-Glu as well as (c) on surface oxidized silicon from solutions of 15 mM [Zn], 15 mM HMTA and 1.88 mM Gly-Glu. All samples were grown for 48 h at 333 K.

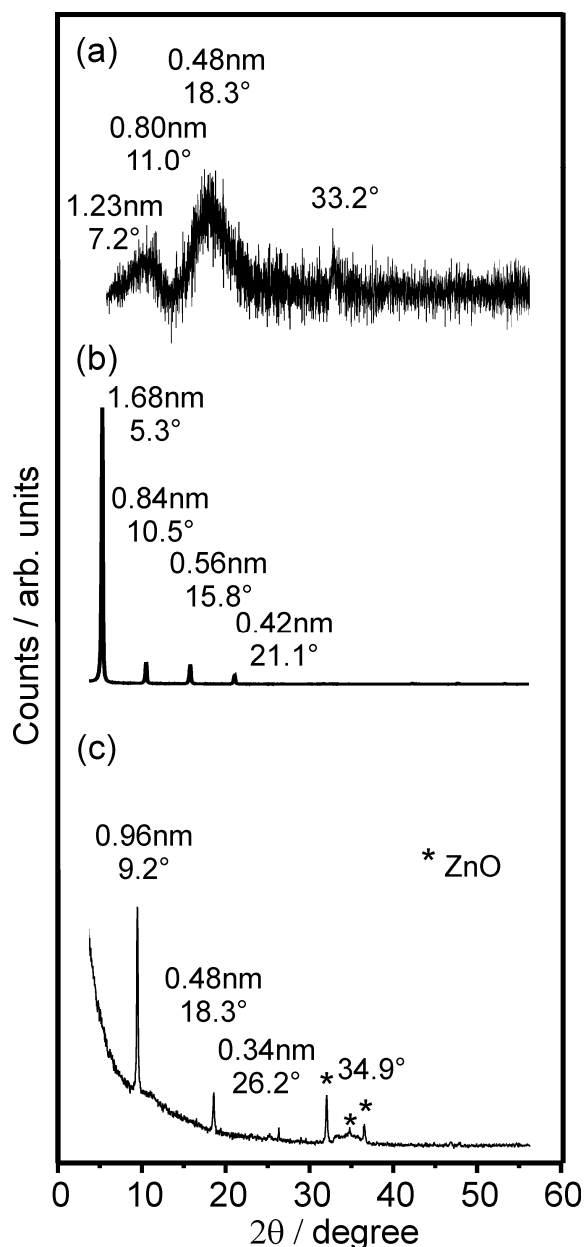


Figure 2.8: XRD diagrams of deposition products from solutions of (a) 15 mM [Zn], 15 mM HMTA and 1.88 mM Gly-Glu, (b) 30 mM [Zn], 30 mM HMTA and 7.5 mM Trp-Gly as well as (c) 30 mM [Zn], 30 mM HMTA and 3.75 mM Arg.

Whereas the before-mentioned LBZs comprise ordered stacking of the brucite layers, the intercalation of carboxylate anions leads to turbostratic disorder as in the case of basic zinc acetate. [35,36] The resulting diffraction pattern consists of sharp reflections in the range of small diffraction angles and broad asymmetric peaks at high angles. [35] These reflections correspond to the (00l) and (hk0) peaks, respectively, as all of the mixed (hkl) peaks are suppressed completely by the randomness in translation and rotation. [37]

In the present study the overall crystal structure could be indexed in the hexagonal system



---

corresponding to the procedure for the basic zinc acetate. [38,39] Accordingly the peaks at the lowest diffraction angles corresponded to the (00l) reflections. Thereby the crystal lattice plane distance of the (001) reflection was commonly attributed to the interlammellar distance in the LBZ structure. The values of 1.68 nm (Gly-Glu) and 1.23 (Trp-Gly) were comparable to the corresponding distance in basic zinc acetate, [38] which varied from 1.31 to 1.43 depending on the conditions of the synthesis, whereas the value for 0.96 (Arg) was slightly smaller.

These findings can also be compared to interlayer bonding of amino acids in layered double hydroxides (LDHs). In LDHs di- and trivalent cations occupy the octahedral sites of brucite layers, between which various types of anions can be situated. [39,40] Rather low interlayer distances were interpreted in the way that the amino acids adopted orientations, in which the longest molecule chords were approximately parallel to the inorganic layers. [40,41]

The rather broad peaks at diffraction angles above  $33.2^\circ$  (Trp-Gly) or  $34.9^\circ$  (Arg), respectively, were assigned to the (hk0) reflections. Such peaks were not observed in the case of Gly-Glu, which indicated oriented growth of the deposition product on the substrate. Weak diffraction peaks of zincite in Figure 2.8c corresponded to minor amounts of co-deposited micrometer-sized crystals with morphologies as shown in Figure 2.1.

The LBZs obtained from the reaction solutions of Trp-Gly, Arg, and Gly-Glu were also characterized by IR spectroscopy (Figure 2.9). The spectra exhibited the typical bands for carboxylate functions, i.e. the  $\nu_{as}$  and the  $\nu_s$  stretching modes, which demonstrated the presence of the amino acids or dipeptides (Table 2.3). The deposition products of solutions containing Trp-Gly and Arg further showed a sharp peak at  $1385\text{ cm}^{-1}$ , which is characteristic for nitrate anions (Figure 2.9a and c). [36] This signal, however, did not appear in samples from solutions with Gly-Glu (Figure 2.9b). The insertion of nitrate was also reported for the above-mentioned LDH compounds, which shows the flexibility of this structure concerning storage and ion exchange properties. [39] The amount of nitrate with respect to the organic anions in the interlayer space was correlated to the charge density of the organic molecules. Thereby amino acids or dipeptides with anionic side groups are more easily intercalated than those with apolar or cationic functions. [39] Correspondingly, Gly-Glu is preferably intercalated compared to Trp-Gly and Arg.

	additive	$\nu_{as}(\text{C=O})$	$\nu_s(\text{C=O})$	$\nu_{as}(\text{NO}_3^-)$
(a)	Trp-Gly	1599	1411 (sh)	1386
(b)	Gly-Glu	1594	1409	
(c)	Arg	1595	1410 (sh)	1383

Table 2.3: Position of the symmetric and asymmetric C=O stretching vibration of deposition products from solutions of (a) 30 mM [Zn], 30 mM HMTA and 7.5 mM Trp-Gly; (b) 15 mM [Zn], 15 mM HMTA and 1.88 mM Gly-Glu; and (c) 30 mM [Zn], 30 mM HMTA and 3.75 mM Arg.

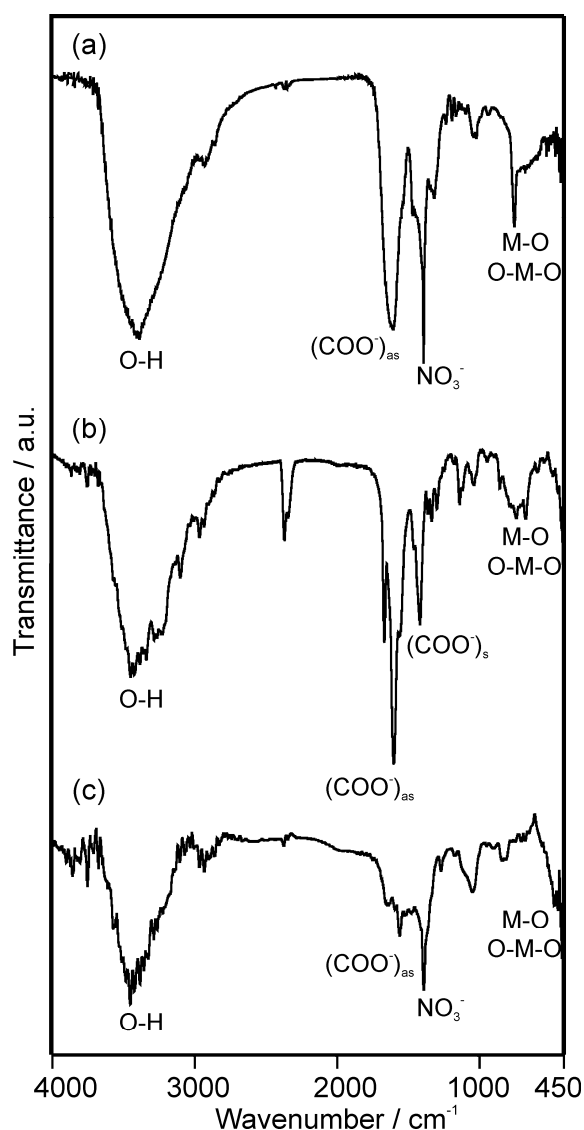


Figure 2.9: IR spectra of deposition products from solutions of (a) 30 mM [Zn], 30 mM HMTA and 7.5 mM Trp-Gly; (b) 15 mM [Zn], 15 mM HMTA and 1.88 mM Gly-Glu; and (c) 30 mM [Zn], 30 mM HMTA and 3.75 mM Arg.

Layered basic zinc salts are not thermally stable and are known to transform into zinc oxide over 423 K. [38] After oxidative calcination of the deposition products only ZnO remained (Figure 2.10). Thereafter films from solutions of Gly-Glu revealed an explicit texture, as only the (002) reflection of the zincite structure was present in the XRD diagrams (Figure 2.10a). Here the  $c$ -axis of the crystallites runs normal to the substrate surface. As mentioned above, the LBZ material derived from Gly-Glu exhibited already preferential orientation to the substrate, which then might have induced oriented growth of zincite in the calcination process. Films from solutions of Trp-Gly exhibited further reflections of zincite after calcination, thus revealing a rather statistical orientation of the crystallites within the film (Figure 2.10b).

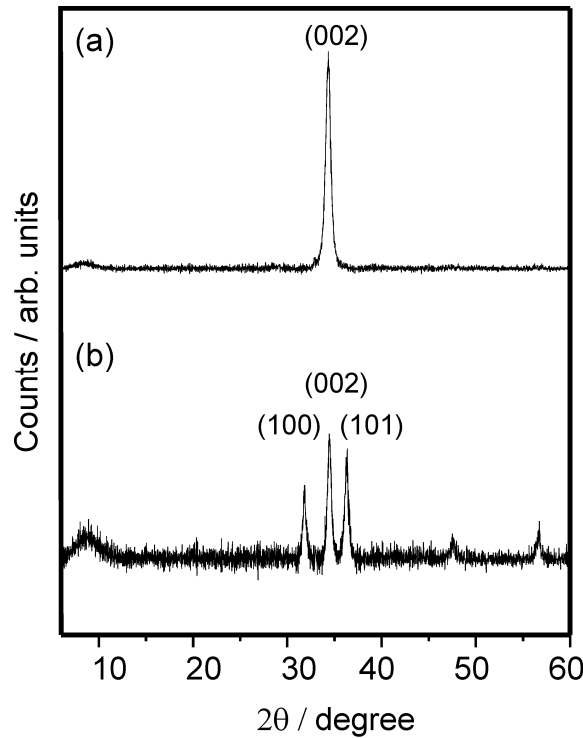


Figure 2.10: XRD diagrams of deposition products after calcinations at 723 K for 4 h in air of films from solutions of (a) 15 mM [Zn], 15 mM HMTA and 1.88 mM Gly-Glu and (b) 30 mM [Zn], 30 mM HMTA and 7.5 mM Trp-Gly.

The distinct morphologies, though, were maintained after annealing (Figure 2.11). This is in agreement with investigations concerning the calcination of films on glass slides of basic zinc acetates with the above-mentioned LBZ structure, which kept a nest-like morphology after heating. The ZnO films obtained in this way did not show preferential orientation with respect to the substrate. [42]

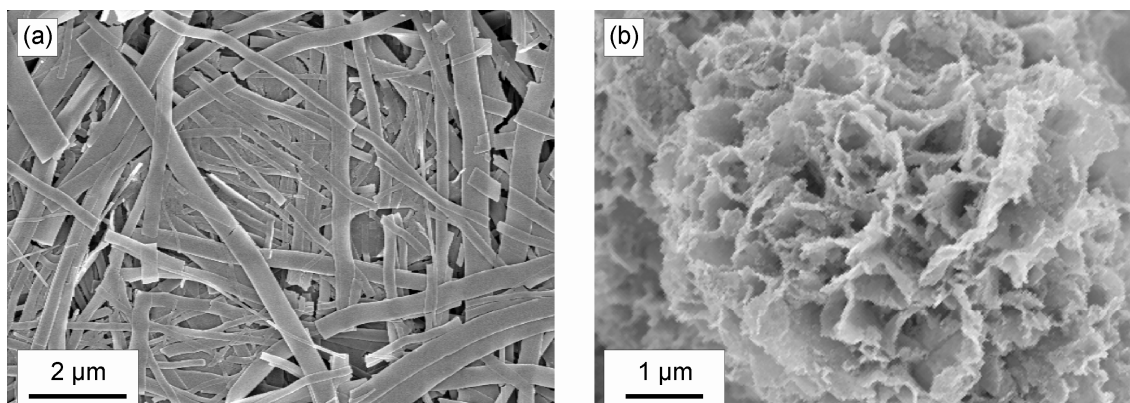


Figure 2.11: SEM micrographs of deposition products after calcinations at 723 K for 4 h in air. As-deposited materials were obtained after 48 h at 333 K from solutions of (a) 15 mM [Zn], 15 mM HMTA and 1.88 mM Gly-Glu and (b) 30 mM [Zn], 30 mM HMTA and 7.5 mM Trp-Gly.

Coatings obtained in the presence of Gly-Glu were further investigated after the annealing treatment. [43] Samples were heated at 723 K for 4 h in air. Bright field (BF) images (Figure 2.12a and 2.12c) acquired with the TEM show the cross section of the coated substrate before and after, respectively, the annealing treatment. The BF micrograph 2.12a displays no observable diffraction patterns while in micrograph 2.12c the nano-size of the ZnO crystals can be observed. The corresponding selected area diffraction (SAD) patterns (Figure 2.12b and 2.12d) confirm these observations. The diffraction pattern (DP) of the non-annealed sample (Figure 2.12b) is characteristic of an amorphous or low-crystalline material. On the contrary, the DP acquired from the dark zone of the annealed sample is formed by the superimposition of the diffracted signals originated from each ZnO nano-crystal (Figure 2.12d). It appears that the ZnO crystals have a strong orientation relation; in fact all the grains illuminated by the electron beam are in the  $\langle 010 \rangle$  zone axis. The broadening of the signal of the reflections shows that the  $\{001\}$  planes of the ZnO nano-crystals, which are parallel to the substrate, have a misorientation between the different grains of approx.  $\pm 10^\circ$ . Consequently, LBZs ribbons formed and stacked on the substrate in the presence of Gly-Glu are transformed into ZnO nano-crystals with a defined orientation and the general morphology of the coating is maintained.

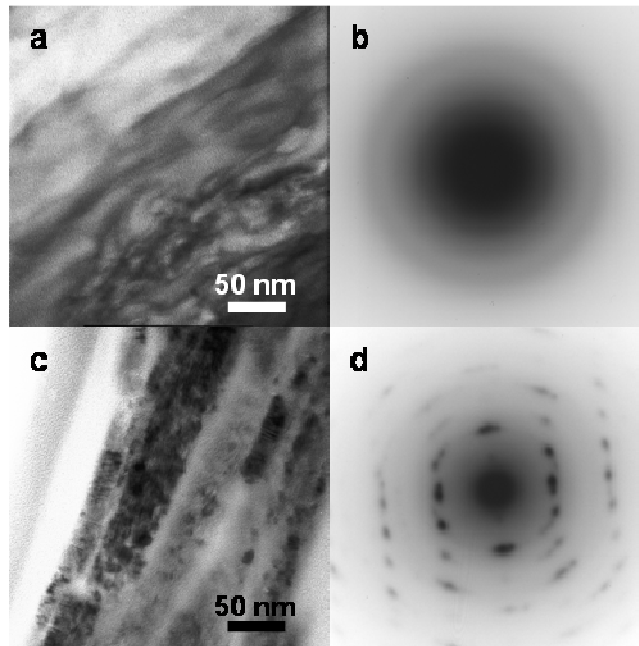


Figure 2.12: [43] TEM bright field images and diffraction patterns of deposits on polyelectrolyte multilayers, obtained from solutions of 15 mM [Zn], 15 mM HMTA and 1.88 mM Gly-Glu before (a and b) and after (c and d) annealing at 723 K for 4h.

For the formation of coatings or deposits by the CBD process, two mechanisms are discussed in the literature, whereby mixed pathways are of course also imaginable. The first route describes the deposition in terms of formation of colloids in the reaction solution (homogeneous nucleation) and their subsequent attachment on the substrate, which can be understood in terms of the DLVO (Derjaguin, Landau, Verwey and Overbeck) theory. Alternatively the successive attachment of ions to the surface (heterogeneous nucleation) can lead to the growth of the coating. [16,17]

In the investigations presented here an important influence of the substrate was revealed for depositions from solutions containing Gly-Glu. In this case the oriented growth of the LBZ on the substrate is observed, which is commonly associated with heterogeneous nucleation. [16] In contrast, the films grown using His as additives seemed to have formed by the attachment of spherical colloidal particles from the solution. To confirm this finding zeta potential measurements were carried out. In accordance with the DLVO theory favourable electrostatic interactions exist with both LBL modified and unmodified silicon, which both show a negative surface charge at the pH value of the reaction. (Van der Waals interactions between the particles then contribute to proceeding film growth.) [16,25]

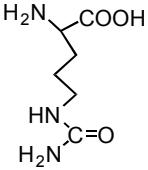
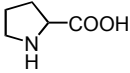
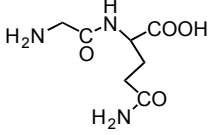
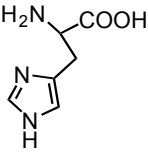
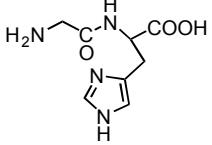
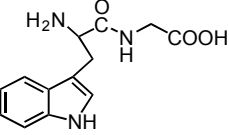
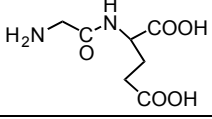
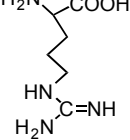
Additive	Structural Formula	Morphology of Deposit	Deposition Product
Cit		micrometer sized crystals	zinc oxide
Pro		micrometer sized crystals	zinc oxide
Gly-Gln		micrometer sized crystals	zinc oxide
His		uniform film	zinc oxide
Gly-His		uniform film	zinc oxide
Trp-Gly		sponge-like coating	LBZ
Gly-Glu		ribbon-like coating	LBZ
Arg		nanoscale platelets	LBZ

Table 2.4: Morphological overview.

## 2.4 Conclusions

Amino acids and peptides provide a strong influence on the morphology of the deposition products formed during mineralization in aqueous zinc salt solutions (Table 2.4). The employment of Pro, Cit, and Gly-Gln yielded micron-sized zincite crystals. This was similar to the mineralization behaviour of ZnO in aqueous solutions of zinc salts and thus indicated a rather weak interaction of these biomolecules with ZnO. His or the peptide Gly-His, though, provided functionalities, which suppressed the formation of larger crystal and stabilized nanosized product particles. This led to the formation of smooth and uniform thin films. The formation of compounds rather than ZnO was observed in the presence of the amino acid Arg as well as the peptides Gly-Glu and Trp-Gly. In these cases sheet-like structures that consisted of layered basic zinc salts were formed. The morphologies resembled the architecture of biomaterials like the nacreous plate structure in seashells or the surface of water-repellent leaves of plants. Accordingly, the properties of such biomaterials like the superhydrophobicity could be mimicked by these synthesized counterparts.

Weak interactions between the biomolecules and zinc compounds yield the classically micrometric ZnO crystals while stronger interactions in solution or at the crystal seeds interface lead to the formation of ZnO-containing thin films. [43] Layered basic zinc salt formation is favoured in the presence of biomolecules that can be intercalated as anions in that structure. The high variability of the morphologies obtained for the basic salts indicates the chelation of the biomolecules to the zinc ions in solution. These morphologies are preserved during heat treatment that permits the formation of oriented ZnO nanocrystals.

## 2.5 Acknowledgements

This project was supported by the KSB foundation. The help of Dr. H.-P. Lamparter, Dr. S. Wildhack and Mr. H. Labitzke with the XRD, Zeta potential and SEM measurements, respectively, is gratefully acknowledged.





**3. Thin film formation by oriented attachment of polymer-capped nanocrystalline ZnO**

## Abstract

Chemical bath deposition has been introduced as a means to produce films of inorganic substances with low engineering expenditure and close to ambient temperature. Organic additives have been used to control the growth of zinc oxide particles in solution and prevent the formation of the typical rod-like morphology. In the present work the attempt is made to combine these two approaches in order to produce thin films of zinc oxide. In the presence of  $\beta$ -cyclodextrin spherical nano-crystalline deposits were obtained from solution; polyethylene glycol induced the formation of nano-structured thin films. With polyvinylpyrrolidone as an additive, uniform films are deposited. The structure of these films is analysed by X-ray diffraction and transmission electron microscopy, which reveals the presence of domains of locally oriented nanocrystals. A mechanism of oriented attachment is proposed to explain the formation of domained ZnO films.

### 3.1 Introduction

The quest for new preparation techniques has led to the so-called “Soft Solution Processing” (SSP). SSP has a broad meaning and refers to any solution processing at, or near, ambient conditions. These methods are promising for the fabrication, shaping, sizing, and orientation of various oxide ceramics with comparatively low technical effort. [44] The synthesis of oxidic thin films from aqueous solutions at low temperatures is of special interest since it provides a possible alternative to vapour-phase processes, which need relatively high effort, or chemical precursor techniques, which require subsequent calcinations. [45,46]

For this purpose the so-called chemical bath deposition (CBD) process was developed, which uses the thermohydrolysis of metal salts to deposit thin films at low temperatures ( $< 100\text{ }^{\circ}\text{C}$ ). [47] The fabrication of zinc oxide films commonly started from solutions of various water-soluble zinc salts. The deposition was induced by an increase in pH, often in combination with slight heating of the solution. [48] In spite of the careful choice of the substrates, only inhomogeneous assemblies of micron-sized elongated crystals could be obtained from such experiments. [49,50,51]

The shape of inorganic crystals is related to the crystallographic unit cell. The diverse crystal morphologies of the same compound arise from differences of the crystal faces in their surface energies, and from different external growth environments. [52] The crystal faces with the highest surface energies are perpendicular to the directions with the highest growth rates; these faces have the tendency to vanish in the final morphology in order to minimize the total surface energy of the crystal. Thus the morphology of a crystal is related to the respective growth rates  $R_{\langle lmn \rangle}$  along the crystallographic directions  $\langle lmn \rangle$ . For ZnO, the growth rates of the directions  $\langle 001 \rangle$ ,  $\langle 101 \rangle$ ,  $\langle 100 \rangle$  have the relationship  $R_{\langle 001 \rangle} > R_{\langle 101 \rangle} > R_{\langle 100 \rangle}$ . These differences cause the commonly found shape of ZnO crystals to be rod or wire-like. [53]

During the last years, organic additives have increasingly been employed to control the growth of zinc oxide crystals in solution. Addition of ethylenediamine to the reaction solution results in precipitates consisting of crystallites with significantly lowered aspect ratio. [12,54] Water-soluble copolymers successfully inhibit crystal growth along the  $\langle 001 \rangle$  direction. [27,55,56] When a precursor of zinc acetate is coated with  $\beta$ -cyclodextrin, almost spherical ZnO particles were obtained. [57] Very small ZnO nanoparticles of variable shape resulted when the seed crystals were capped with polyvinylpyrrolidone (PVP) with an average molecular weight  $M_r$  of 10 000. [58,59,60,61] In contrast, polyethylene glycol (PEG) with an average molecular weight  $M_r$

of 200 as an additive caused even longer and thinner rods or wires to grow than without additive. [62]

The target of the present work in this field is to combine the technique of chemical bath deposition for zinc oxide thin films on plane substrates with the usage of organic additives in order to obtain smooth and homogeneous films. In this connection, films of zinc compounds with a vast number of morphologies can be obtained on silicon substrates covered with polyelectrolyte multilayers if amino acids or peptides are present within the deposition solution. [63,64] Another success was the preparation of homogeneous zinc oxide films from aqueous solutions in the presence of PMAA-graft-PEO polymers. [18] Only recently, the deposition of widely homogeneous nanostructured ZnO thin films on silicon wafers, modified with self-assembled monolayers (SAMs), from alcoholic solutions containing PVP, [19] was achieved.

This paper deals with the deposition of zinc oxide from solutions containing PEG,  $\beta$ -cyclodextrin, and PVP. We present experimental evidence that PEG with an average molecular weight of 8 000 and  $\beta$ -cyclodextrin prevent ZnO particle growth in solution. These compounds aid the formation of nanocrystalline particles and their precipitation on SAM-modified substrates. As ZnO films of the highest uniformity were obtained with PVP, the microstructure of these films was then investigated using X-ray diffraction (XRD) and transmission electron microscopy (TEM). Based on these results, a mechanism involved in the growth of the films is discussed.

## 3.2 Experimental

### 3.2.1 Preparation of the deposition solutions

For the deposition solution containing PEG, 0.264 g (1.2 mmol)  $\text{Zn}(\text{CH}_3\text{COO})_2 \cdot 2 \text{H}_2\text{O}$  (Sigma-Aldrich) was dissolved in 30 ml methanol, and, with the aid of ultrasound, 9.6 g (1.2 mmol) PEG-8000 (average molar weight  $M = 8000 \text{ g}\cdot\text{mol}^{-1}$ , Sigma-Aldrich) was dissolved in 60 ml Methanol, or 2 ml (approx. 9 mmol) PEG-200 (average molar weight  $M = 200 \text{ g}\cdot\text{mol}^{-1}$ , Sigma-Aldrich) was diluted with methanol to a total volume of 60 ml. In order to make up for the lower molecular weight of PEG-200, a higher concentration of this compound was used. The two solutions were mixed, and under gentle stirring 30 ml of a 0.1 M solution of tetraethylammonium hydroxide (3 mmol) was added dropwise using a peristaltic pump at a flow rate of  $1.5 \text{ ml}\cdot\text{min}^{-1}$ .

For deposition in the presence of  $\beta$ -cyclodextrin, 0.34 g (0.3 mmol)  $\beta$ -cyclodextrin (Fluka) was dissolved in 9 ml distilled water at  $70 \text{ }^\circ\text{C}$  with the aid of ultrasound, followed by gradual

---

cooling to room temperature. To this solution, first 42 mg (0.3 mmol) hexamethylenetetramine (urotropine, Merck) were added, then 1 ml of a 0.03 M solution of zinc nitrate (0.03 mmol). This solution was used for deposition immediately after preparation. Pursuant solutions were prepared with a zinc nitrate concentration of 15 mmol·l<sup>-1</sup> instead of 3 mmol·l<sup>-1</sup>, keeping the concentrations of all other ingredients constant. Aqueous deposition solutions with PEG or PVP as additives were prepared according to the same recipe and with the same molar quantities, except for the usage of 30 mmol·l<sup>-1</sup> zinc nitrate.

The precursor solution containing PVP was prepared in 2-propanol solvent. 0.110 g (0.5 mmol) Zn(CH<sub>3</sub>COO)<sub>2</sub> · 2 H<sub>2</sub>O was dissolved in 0.12 ml distilled water. Under vigorous stirring at 50 °C, the solution was diluted with 2-propanol first to a total volume of 20 ml, then without stirring to 50 ml, followed by chilling to 0 °C. Again at room temperature, PVP with an average molecular weight of 10 000 g·mol<sup>-1</sup> (PVP K15, Fluka) was dissolved in the above solution with a molar ratio [PVP] : [Zn<sup>2+</sup>] = 3 : 5, aided by ultrasound. Finally, 0.04 g (1 mmol) NaOH pellets were dissolved in 0.264 ml distilled water. This solution was diluted to 8 ml with 2-propanol. Under continuous stirring, it was added dropwise to the first solution of zinc acetate and PVP using a peristaltic pump. Having been sonicated for 10 min, the solution is ready for deposition. The above preparation method yields a precursor solution with a [Zn] concentration about five orders of magnitude higher than reported in literature for the preparation of nanoparticles. [58,60,61]

Three different approaches were applied for the synthesis: Hydrolysis of soluble zinc salts is faster in water than in organic solvents, and hence more difficult to control. When aqueous, instead of alcoholic, solutions containing PEG or PVP were used, micrometer-sized ZnO crystals occurred irrespective of the average molar weight of the polymer. Therefore, if possible, alcoholic solutions were employed. Due to the poor solubility of β-cyclodextrin in alcohols, in this case deposition was done in aqueous environment. A previously published method [18] was adapted for this purpose. For the polymeric additives, the deposition process in n-propanol has already been presented; [19] the process in methanol is an optimized one which was developed only recently. Experiments with PVP in methanolic solution are under way; results will be published shortly. It has no influence on the deposition product whether zinc acetate or zinc nitrate is applied as a precursor.

### 3.2.2 Substrate preparation and film deposition

The substrates were p-type single-crystal Si (100) wafers with one side polished. They were cleaned and oxidized in piranha solution (70 vol.-% conc. H<sub>2</sub>SO<sub>4</sub> and 30 vol.-% of 30 wt.-% H<sub>2</sub>O<sub>2</sub>) and washed abundantly with distilled water afterwards. The substrates were immersed in a 1 vol.-% solution of 1-thioacetato-16-trichlorosilyl hexadecane in bicyclohexyl under argon atmosphere, so that a self-assembled monolayer (SAM) grew on the polished side. Finally, the thioacetate functionality was converted into sulfonate (–SO<sub>3</sub>H) in a concentrated aqueous solution of potassium hydrogen monopersulfate. The procedure was described in detail by Collins et al. [65]

In the cases of the alcoholic deposition solutions, sulfonate-functionalized substrates were immersed in 10 ml aliquots of the deposition solution, covered and placed in an oil bath at 55 °C (PVP) or 60 °C (PEG). The solution was removed after 1 – 1.5 h. Thicker films were obtained by repeating this procedure. In the case of the aqueous deposition solutions, the sulfonate-modified substrates were again immersed in a 10 ml aliquot each, but this time they were heated to 85 °C and kept at this temperature for 48 h. All solutions became turbid during the deposition process, indicating the formation of relatively large agglomerates in solution. As a final step, all samples were washed with distilled water and dried in a stream of argon.

### 3.2.3 Film characterization

The obtained ZnO films were characterized by scanning electron microscopy (SEM) (JEOL JSM-6300 F at 3 kV). Their structural properties were examined using a JEOL JEM-4000 FX transmission electron microscope (acceleration voltage 400 kV). X-ray diffractograms were taken on a Philips X'pert K $\alpha_1$  diffractometer equipped with a primary beam monochromator to select only K $\alpha_1$  radiation, and on a Siemens diffractometer D5000, again using Cu K $\alpha_1$  radiation with  $\lambda = 0.15406$  nm. Scherrer analysis of the diffraction diagrams was done in the following way: The full width at half maximum (FWHM)  $\gamma$  of the diffraction peaks was obtained by fitting three Gaussian maxima with interdependent standard deviations  $\sigma$  to the (100), (002), and (101) peaks of the ZnO diffraction diagram, and by computing  $\gamma$  from  $\sigma$ . The average crystallite diameter  $d$  was then calculated using the well-known Scherrer formula:  $d = \frac{0.94 \cdot \lambda}{\gamma \cdot \cos \theta}$ ,

where  $\lambda$  is the source wavelength, and  $2\theta$  the peak position. A Zetasizer Malvern 3000 HSA was

used to measure the zeta potential of ZnO particles in the deposition solution.

For preparation of cross-sectional TEM specimens, slices of ZnO/Si with a width of approximately 3.5 mm were cleaved from the wafers. Two sample slices were glued together by epoxy resin with the coated sides facing each other. Special care was taken to avoid high temperature during TEM specimen preparation, which might change the film structure. Therefore the glue was cured under pressure at room temperature for two days. Subsequently two pieces of silicon were glued to both sides of the sample sandwich, so that the cross-section of the whole sandwich reached about 3 mm in diameter. Finally a thin slice with a thickness of 0.8 mm was cut with a wire saw. Both sides of the sample were ground and polished until the sample thickness was 80 – 100  $\mu\text{m}$  and smooth planes were obtained. One side was further ground and polished on a Gatan 656 Dimple Grinder until the thickness reached about 10 – 20  $\mu\text{m}$ . The sample was sputtered with  $\text{Ar}^+$  ions at 4 keV in a Gatan Duo 691 ion-milling machine on both sides till perforation.

For preparation of a plan-view ZnO/Si sample, the uncoated side of the substrate was ground until the thickness of the sample reached approximately 90  $\mu\text{m}$ , followed by dimple grinding and polishing to a thickness of below 25  $\mu\text{m}$ . The same side was then further thinned with  $\text{Ar}^+$  ions at 4 keV till perforation.

### 3.3 Results and discussion

In this section of the paper, results will be presented which indicate that PEG and  $\beta$ -cyclodextrin as well as PVP are able to inhibit grain growth of ZnO crystallites and direct the formation of ZnO nanostructures under suitable conditions. Figures 3.1a and 3.1b show the morphologies resulting from deposition of ZnO from precursor solutions containing PEG-8000 and  $\beta$ -cyclodextrin, respectively. In the case of PEG-8000 (i. e. using PEG-molecules significantly larger than Li et al. [62]), the substrate was fully covered. However the roughness of the film is high. By comparing the height of ZnO deposits on the substrate close to the fracture surface and the scale bar of Figure 3.1a, the maximum film thickness could be determined to be about 200 nm. Scherrer analysis of the X-ray diagram was impossible, since the intensity of the diffraction peaks was too low due to the small amount of ZnO on the substrate. This implies that the film is highly porous. Deposition from alcoholic solutions containing PEG-200 led to films with similar morphology, but with an even higher roughness. Their large grains are about 37 nm in diameter, as determined by X-ray diffraction.

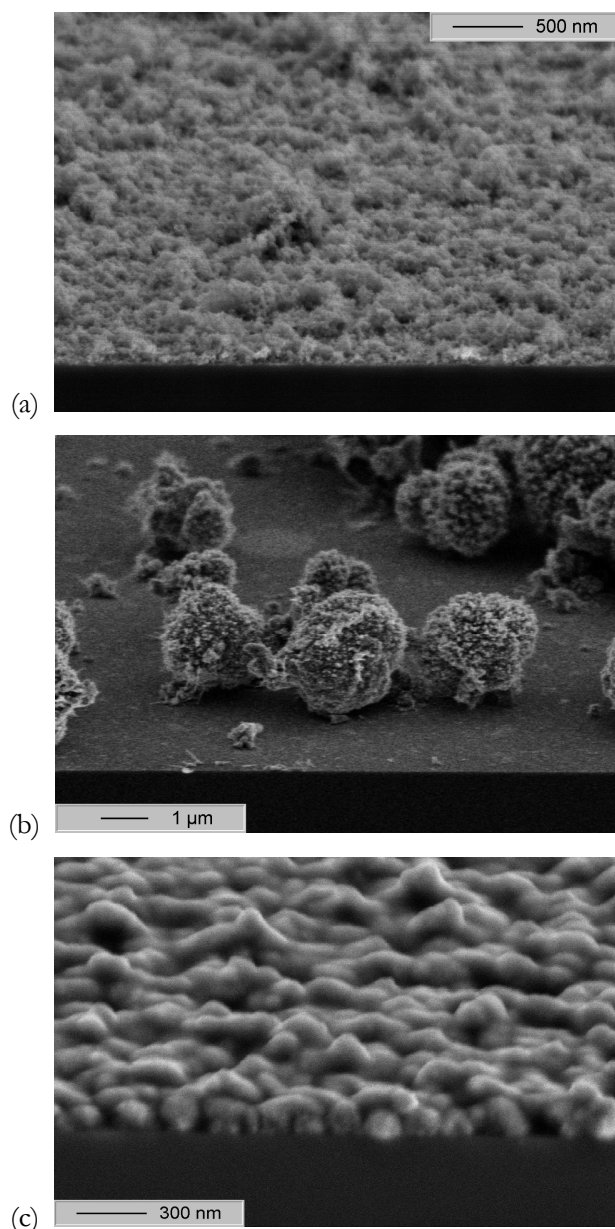


Figure 3.1: SEM micrographs (cross-sections tilted by  $20^\circ$ ) of ZnO deposited on sulfonate-modified Si substrates: (a) in the presence of PEG-8000; (b) in the presence of  $\beta$ -cyclodextrin; (c) in the presence of PVP.

In the case of  $\beta$ -cyclodextrin no cohesive film was formed at all. Instead, a hierarchically structured morphology was observed. After deposition from the solution with 3 mM zinc nitrate, almost spherical aggregates with a diameter of about  $2 \mu\text{m}$  were adhering to the substrate. Both the overall appearance of the aggregates in Figure 3.1b and SEM images of fractured aggregates, with higher magnification, indicate that the large, micron-sized aggregates are composed of much smaller nanocrystals. Most of these nanocrystals have an only slightly elongated, angular shape, whereas truly long, hair-like nanocrystals protruded only from few of the large spherical



aggregates. Scherrer analysis of X-ray diffractograms confirmed that ZnO nanocrystals with an average size of 23 nm are present in the deposits. Yang et al. [58] had already observed the ability of  $\beta$ -cyclodextrin to inhibit the formation of elongated, rod-like ZnO crystals. However the aggregation of the resulting nanoparticles to spherical deposits on a substrate covered with a sulfonate-modified SAM was unexpected. When the deposition solution with the ten times higher zinc nitrate concentration was used, aggregates consisting of micrometer-sized platelets and needle-shaped ZnO crystals were deposited on the substrate.

When PVP is applied as an additive in the CBD process for the deposition of zinc oxide, the thin films are smoother and more uniform than with the other additives (Figure 3.1c). Figure 3.2a shows a TEM image of the cross-section of a ZnO film deposited in the presence of PVP. A mean film thickness of 130 nm is observed. An intermediate layer with bright contrast may be seen between the ZnO film and the silicon substrate, which is in accordance with the modification of the substrate with the SAM and the amorphous silicon oxide layer induced by piranha cleaning. (The intermediate layer can be seen more clearly in the high-resolution TEM images in Figure 3.5.) The corresponding selected area electron diffraction (SAD) pattern (Figure 3.2b) and the X-ray diffraction (XRD) diagram (Figure 3.3) indicate that the ZnO film consists of polycrystalline zincite. Scherrer analysis of the XRD diagram (Figure 3.3) indicates that the crystallites forming the film have an average size of about 8 nm. Analysis of HRTEM micrographs (see below) confirms this result and hence justifies the disregard of stresses in the evaluation of the XRD diagrams. The fractured rings of the SAD pattern suggest oriented alignment of the crystallites since SAD patterns of a polycrystalline substance with randomly arranged grains would consist of a series of continuous rings. Especially the pronounced 100 and  $\bar{1}00$  peaks instead of a complete (100) ring are evidence of the presence of a texture in the area which corresponds to the diffraction pattern. More SAD patterns taken from different areas of the film exhibit the same tendency. Therefore it is concluded that portions of the film have a local texture.

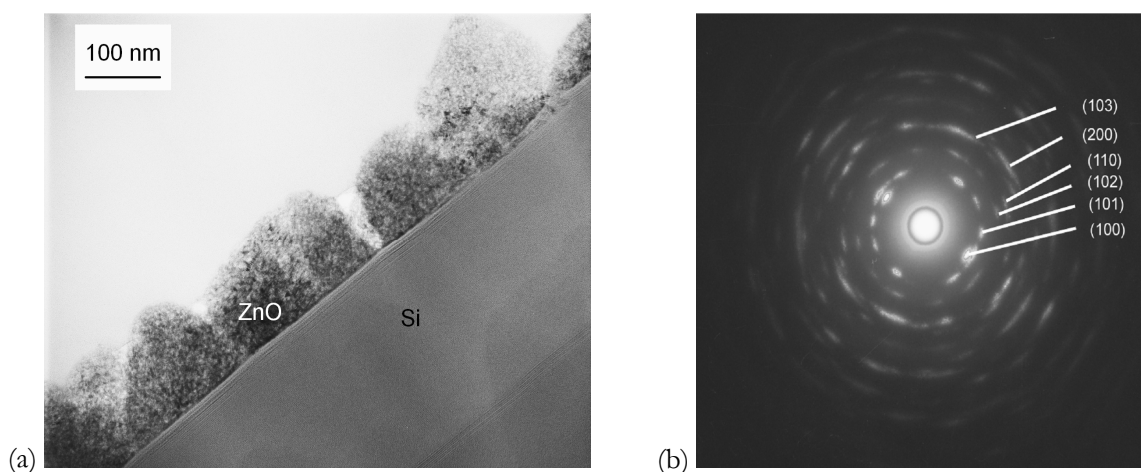


Figure 3.2: (a) Bright-field TEM image of a ZnO film deposited in the presence of PVP; (b) corresponding SAD pattern.

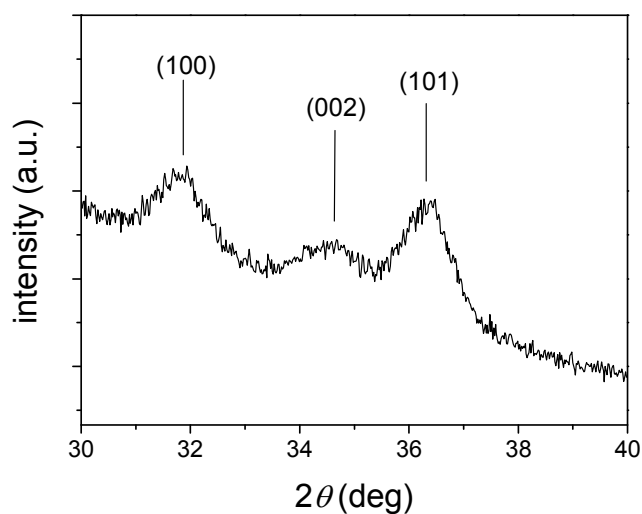


Figure 3.3: XRD diagram of a ZnO film deposited in the presence of PVP.

Even though XRD as an averaging technique does not reveal any texture of the film (Figure 3.3), domains of about 135 nm in size comprising equably oriented nanometer-sized ZnO crystallites can be seen in dark field cross-sectional TEM images (Figure 3.4a). The dark-field plan-view TEM micrograph (Figure 3.4b) shows that the ZnO film is composed of domains with average size of 140 nm, in agreement with the cross-sectional image.

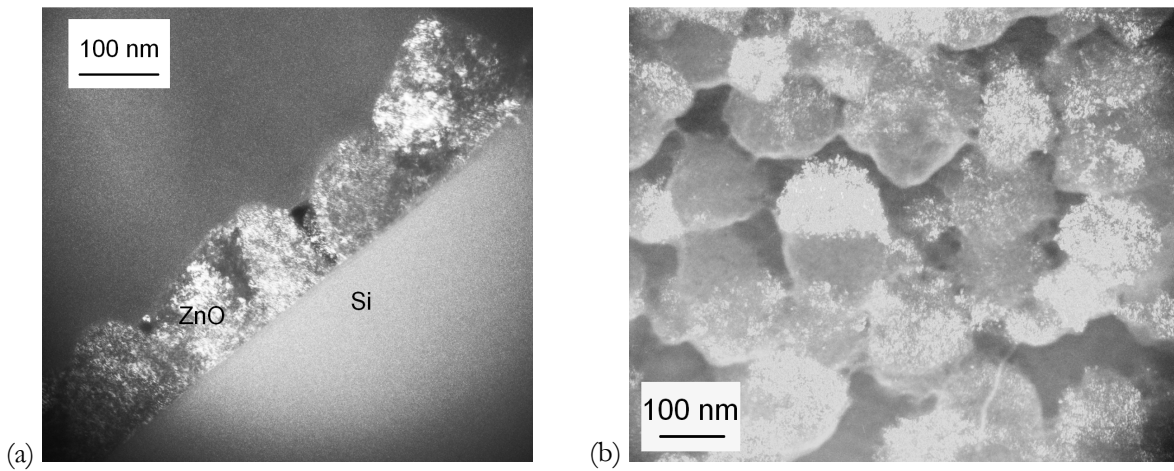


Figure 3.4: Dark-field TEM images of ZnO films deposited in the presence of PVP: (a) cross section showing the same region of the same sample as Figure 3a; (b) plane view.

High-resolution TEM (HRTEM) investigations were conducted to elucidate the structure of the nanocrystalline ZnO film. Cross-sectional HRTEM micrographs of the ZnO film in the vicinity of the substrate are shown in Figure 3.5. They clearly show that adjacent ZnO nanocrystallites in the same domain have almost the same crystallographic orientation. Nevertheless, the common crystallographic planes are slightly misoriented in the neighbouring nanocrystals to form small-angle grain boundaries, e. g. near the centre of Figure 3.5d. This allows the individual grains to be distinguished. The size of the grains is in the range of 5 – 10 nm. More evidence is provided by the moiré fringes perpendicular to the crystallographic planes, indicating an orientation mismatch between two neighbouring grains stacked along the path of the electron beam. From the fringe spacing of the moiré pattern in Figure 3.5a, an angular misalignment of  $4^\circ$  between the two grains was calculated.

Recently, a concept of oriented particle aggregation was developed. [66] This theory describes the self-assembly of colloidal primary particles into aggregates and the subsequent internal restructuring, which then leads to a crystallographically continuous and ordered structure. This mechanism has already been observed experimentally using HRTEM investigations of the interaction between single nano-sized ZnO rods in solution. [67] Endorsing this concept also for larger assemblies, our experimental results provide evidence of oriented aggregation of nanocrystals as building blocks of compact ZnO films.

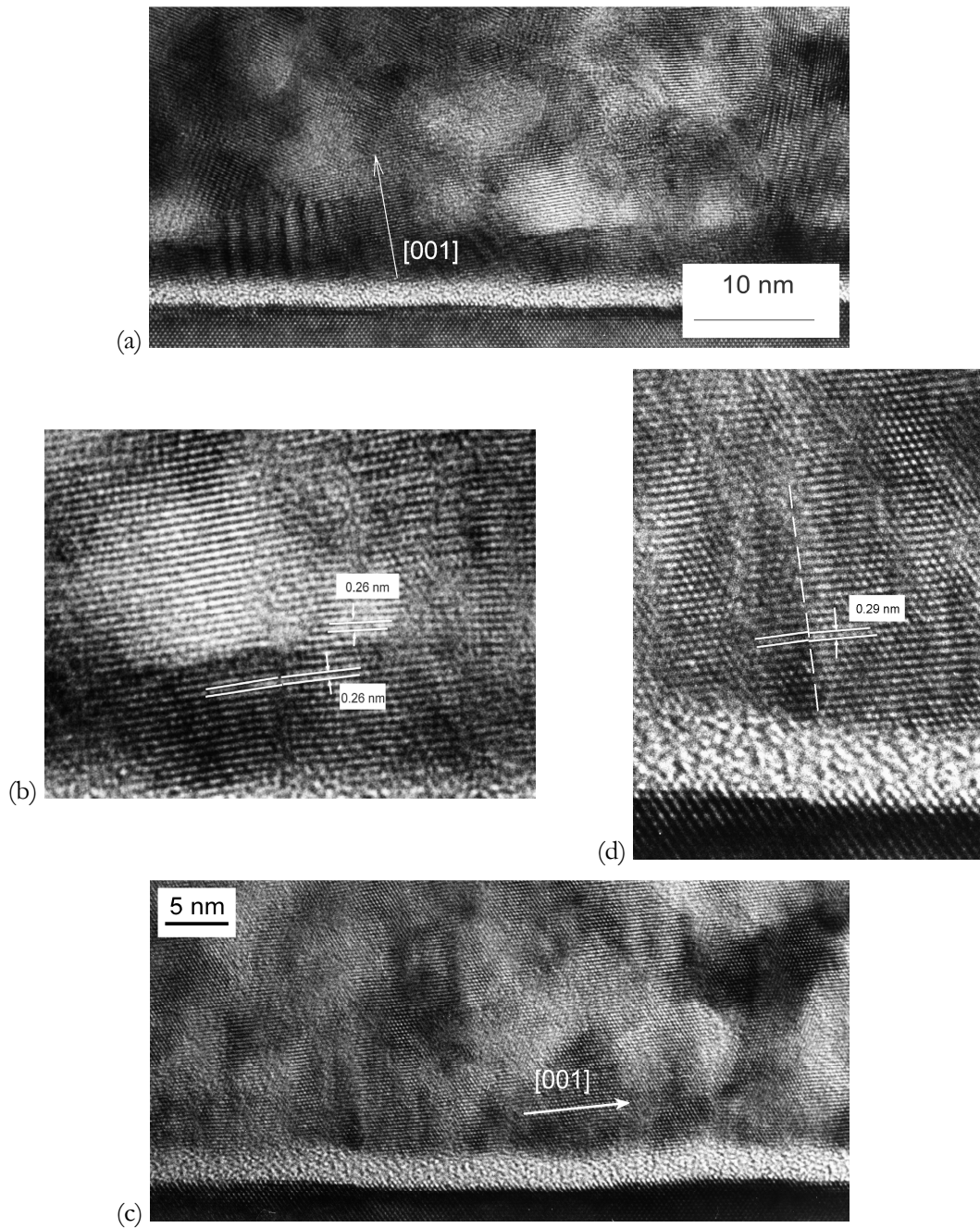


Figure 3.5: HRTEM images of ZnO films deposited in the presence of PVP: (a)  $c$ -axis of the crystal grains is preferentially oriented perpendicular to the substrate; (b) detail of (a); (c)  $c$ -axis of crystal grains is preferentially oriented parallel to the substrate; (d) detail of (c), where a small angle grain boundary is indicated by a dashed line. In (a) and (c), the [001] direction is indicated with an arrow.

For elucidation, film formation can be split up into two stages: In the first stage, single nanocrystallites adsorb on the previously bare substrate and hereby initiate aggregation at diverse sites on the substrate simultaneously. The nanocrystallites are assumed to have formed in solution previously. Evidence of homogeneous nucleation is the observed turbidity of the solu-

tion and the polycrystalline structure of the films with nearly spherical grains. In this stage various orientations occur, and the orientation in one place is unrelated to that in other places. In a second stage, further nanocrystallites attach to the ones which have adsorbed previously and adopt their orientation. Thus domains consisting of nanocrystals having preferred orientation develop. Finally, a continuous thin film containing differently oriented domains of aligned nanocrystallites forms (Figure 3.6).

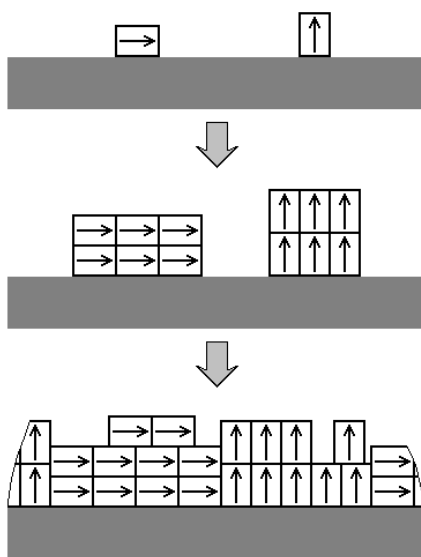


Figure 3.6: Schematic model of oriented aggregation of polar nanoparticles on a substrate, exemplarily showing two possible orientations of the resulting domains.

Step 1 (above): First particles attach to the substrate independently of each other. Step 2 (centre): The orientation of subsequent particles is determined by the first particles. Step 3 (below): Gradually a domained film is formed. The arrows indicate crystallographic polarity and orientation of the crystallites; they are parallel to the  $\langle 001 \rangle$  direction and point from the positive to the negative plane. Small-angle misalignments between the grains are neglected in the sketch.

The substrate surface is negatively charged due to the sulfonate-modified SAM, and the zeta potential of the particles was determined to be positive. Therefore ZnO particles adsorb on the substrate easily during the initial stage of film formation. They attach with variable orientations. As suggested by the XRD diffractograms (see above), there is no indication that one orientation is favoured above others. Two possible orientations are presented in Figure 3.5. Figure 3.5a shows the ZnO crystallites of the first layer of the film to be arranged on the substrate with the (001) plane nearly parallel to the substrate surface, i. e. with the  $c$ -axis more or less perpendicular to the substrate, whereas in Figure 3.5c the (100) planes of the grains are almost

---

parallel to the substrate surface, i. e. the  $c$ -axis is parallel to the substrate. The difference in orientation is verified by the different spacings of the lattice planes which are nearly parallel to the substrate surface (Figure 3.5b and 3.5d). Lattice spacings were determined using two-dimensional Fast Fourier Transformation (FFT) of selected areas of the HRTEM images, and compared with the well-known Si lattice. The spacing of 0.29 nm (Figure 3.5c and 3.5d) reflects the dimension of the zincite unit cell in [100] direction, whereas the spacing of 0.26 nm (Figure 3.5a and 3.5b) corresponds to the minimum distance between two zinc-packed or two oxygen-packed planes along the [001] direction.

Oriented aggregation [66,67] is the concept favoured to describe the second stage of film formation: The way in which the particles of the first layer arrange themselves on the substrate determines the alignment of other particles adsorbing subsequently. This is due to a particularity of the hexagonal crystal structure of ZnO: The basal plane (001) of ZnO is a polar surface, whereas the prismatic planes  $\{100\}$  are non-polar surfaces. Therefore, selective oriented attachment, i.e. polar surface to polar surface and non-polar surface to non-polar surface, can occur.

The nanometer-sized ZnO grains in the deposits confirm that all three additives are able to inhibit crystal growth. A mechanism explaining the formation of thin films instead of micrometer-sized crystals is proposed enhancing the suggestions of Hoffmann et al.: [18] In semi-dilute polymer solutions, metastable nanoparticles are formed, which are fixed among the interpenetrating polymer chains. The nature of the interaction between nanoparticles and polymers has not yet been elucidated; in the case of PEG it is possibly merely steric, [68] while in the case of PVP probably chemical interaction with the nitrogen and/or oxygen atoms of PVP is involved. [69] Surface hydroxylation of the ZnO was detected by XPS [19] and may also play a role. As the observed nanocrystals are nearly spherical, involvement of particular crystal planes in the interaction is not favoured. At low polymer concentrations the seed crystals are able to grow towards large hexagonal prisms. At sufficiently high polymer concentrations, however, the ubiquity of polymers impedes crystal growth, so that the size of the crystallites remains in the range of few nanometers. The so formed nanocrystals can attach to the substrate to form a thin film. Alternatively, they can form aggregates in solution, which accounts for the observed turbidity. Overly high polymer concentrations do not allow for crystallization at all. With  $\beta$ -cyclodextrin, a different mechanism is at work: Complex formation between  $\beta$ -cyclodextrin and zinc ions has been reported, [57] whereas in this case of course no polymer network is present in solution.

XPS measurements revealed no nitrogen signal from the films obtained with PVP. [19] Therefore the interaction between the ZnO nanocrystals and the polymers must be relatively weak. Possible chemical bonds must be broken when the ZnO nanocrystals adsorb on the

substrate or on previously attached ZnO grains, so these bonds must be weaker than the electrostatic and van der Waals forces which direct adsorption. It is concluded that the polymers influence the growth of colloidal particles in solution, but have hardly any impact on the subsequent aggregation process.

The films deposited in the presence of PVP showed photoluminescent behaviour (Figure 3.7). [70] The spectra were typical for nanocrystalline ZnO, revealing an emission at about 360 nm (Figure 3.7a), which is usually attributed to the exciton band, and a very broad signal at 580 nm (Figure 3.7b), which is generally discussed with respect to oxygen vacancies at the surface. [71]

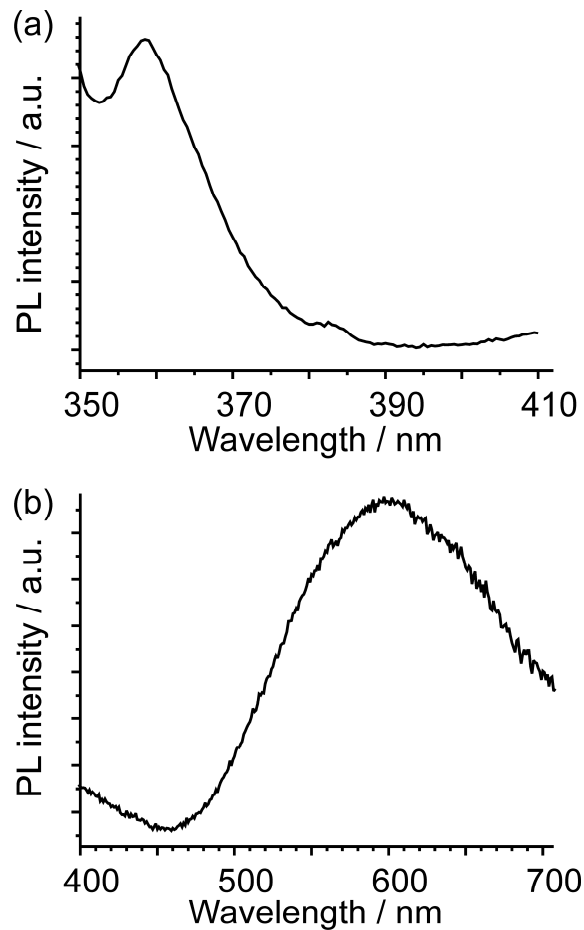


Figure 3.7: [70] Photoluminescence spectra of ZnO thin films in Figure 1 and 2: (a) UV emission spectrum in the range of 350-410 nm; (b) visible emission spectrum in the range of 400-750 nm.

### 3.4 Conclusions

In the present work, the influence of selected organic additives onto the deposition of zinc oxide from solution at ambient temperature was investigated. In the presence of long-chained PEG molecules, rough ZnO films form. In contrast,  $\beta$ -cyclodextrin induced the formation of novel spherical aggregates of ZnO nanoparticles on a substrate. The deposition of ZnO films from alcoholic solution of a zinc acetate precursor in the presence of PVP has already been published. [19] Now it is proven that the ZnO films so obtained consist of nanometer-sized zincite crystals. TEM results show that the ZnO films consist of domains of nanocrystallites with preferential orientations. The formation of films containing such domains is explained by the following mechanism: ZnO seed crystals are formed in the deposition solution. The presence of PVP permits the formation of nanometer-sized particles, but inhibits their growth towards micrometer-sized crystals. The first crystal grains attaching to the substrate show different orientations, and the orientation of a crystallite attached in one place is unrelated to the orientation of a crystallite attached in another place. Alignment of the  $c$ -axis of the unit cell parallel or perpendicular to the substrate was observed. The orientation of the first crystallites adhering to the substrate determines the orientation of subsequently adsorbed grains according to the process of oriented attachment proposed for polar nanoparticles. PVP influences the growth behaviour of the ZnO crystal grains in solution; its direct impact on the aggregation of ZnO grains on the substrate seems improbable.

### 3.5 Acknowledgements

We thank Dr. Hannes-Peter Lamparter for recording the X-ray diffraction data and Marion Kelsch for technical support at the transmission electron microscope and help with TEM-specimen preparation.







**4. Site-selective deposition of nanostructured ZnO thin films from solutions containing polyvinylpyrrolidone**

## Abstract

When soluble zinc salts are hydrolysed in water, usually elongated micron-sized zincite crystals are formed. In this study polyvinylpyrrolidone (PVP) in a methanolic solution is used as an agent to control the morphology of the deposition product. It prevents crystal growth and yields zinc oxide nanocrystals. Thin films consisting of zinc oxide nanocrystals are formed on self-assembled monolayers (SAM) of sulfonate-terminated alkylsiloxanes. Patterned films are deposited after local decomposition of the SAM by UV irradiation. The films fabricated from methanolic solutions containing PVP are particularly smooth, uniform and stable. Their thickness is determined by the deposition time and the molar ratio  $[PVP] : [Zn^{2+}]$ , so that films of arbitrary thickness and nearly constant roughness can be obtained. The crystal grains are oriented preferentially with the  $\langle 001 \rangle$  direction perpendicular to the substrate surface. The films show ultraviolet, orange-red and green-yellow photoluminescence; the latter is quenched by heat treatment. Based on the obtained experimental results, a deposition mechanism is suggested.

## 4.1 Introduction

Zinc oxide is a semiconductor with a wide band gap of 3.37 eV at room temperature. Due to its luminescence properties and its ability to retain a highly efficient emission even at low excitation, [72] it has gained much attention as a promising phosphor material with various applications such as displays, [73] UV-light-emitting diodes, [74] and laser diodes. [75] As a semiconductor which exhibits significant photoconductivity, [76] ZnO is interesting for electronic applications as well. Its use has been explored in gas sensors, [77] varistors, [78] piezoelectric devices such as electroacoustic transducers, [79] and highly transparent conducting windows for solar cells and displays. [80] It absorbs destructive ultraviolet rays better than most other minerals. [81] Due to this wide field of applications of zinc oxide, [82] the fabrication of both thin coatings and nanostructures of zinc oxide has attracted considerable interest.

As a gentle and inexpensive alternative to conventional routes for the deposition of thin films, the method of chemical bath deposition (CBD) was introduced [47] and applied for the production of ZnO thin films. [12] CBD here refers to the thermohydrolysis of metal salts for the fabrication of oxidic films. However, in the case of zinc oxide, the hydrolysis of the soluble precursors tends to result in the formation of oblong hexagonal crystals with lengths of up to several micrometers, so that the deposition of smooth homogeneous nanostructures has remained impossible for a long time. [16] Additionally, without the control of the crystal morphology, improvement of the luminescence properties is impossible. [83] Recently, the preparation of zinc oxide based nanostructured films without these insufficiencies was reported. [17,18] Two innovations provide for this success: dissolution of macromolecular organic substances in the deposition medium as growth-controlling additives, and surface-modification of the substrate with thin organic layers. The presence of the additives in solution inhibits the growth of micron-sized crystals in the deposition solution, and only small crystallites with diameters of few nanometers are formed. On organic self-assembled monolayers (SAMs) with appropriate terminal functionalities, these particles assemble into nanostructured films with luminescent properties. [19]  $\beta$ -cyclodextrin, polyethylene glycol (PEG), and polyvinylpyrrolidone (PVP) are additives that were employed for the preparation of nanocrystalline ZnO deposits on substrates modified with sulfonate-SAMs. [84] Although PVP had already been used as a binder in sol-gel processes, [85,86] its ability to direct mineralization has not been exploited before. Recently it was demonstrated that PVP was the most suitable among several additives for inducing the formation of homogeneous thin films. [19] However the films were still rough and irregular, with a limited thickness, and a long-range texture could not be achieved – features which would have rendered application of

the deposits impossible for many purposes.

For optical and electronic applications, often patterned thin films of ZnO are required. Conventionally, they are prepared by etching processes using photoresist and lithography techniques. However, the fabrication of high-resolution patterns using such subtractive methods implicates the risk of damaging the substrate. To solve such problems, site-selective deposition was proposed in 2001 for the first time for ceramics. [87] First attempts with ZnO employed crystal growth from gas-phase reactions induced by catalysts; [88] however these additively patterned deposits did not show visible-light luminescence. Recently chemical bath deposition techniques have been developed for an additive micropatterning of ceramic thin films, [89] and it was shown that micropatterns fabricated at low temperature, i. e. ellipsoids, multineedles and hexagonal cylinders with lengths of about 0.5  $\mu\text{m}$  deposited on self-assembled monolayers (SAMs), were light-emitting. [90]

In the present paper, a new process of making use of PVP as additive in the deposition of ZnO thin films is reported, which successfully overcomes the shortcomings of earlier deposition processes. Additionally, attempts are conducted to integrate the concept of non-destructive patterning into the chemical bath deposition of ZnO based on the modified PVP-directed control of the microstructure of the films generated as introduced above.

In particular, it is shown that the deposition of polycrystalline ZnO films happens specifically on SAMs of sulfonate-modified alkylsiloxanes, which may be carried by a silicon or glass support. Thin films of zinc oxide are formed on such substrates at only slightly elevated temperatures when the substrates are immersed in a deposition solution containing a soluble zinc salt, the polymer PVP, and a base. For deposition of patterned films, the SAM was destroyed by UV irradiation in selected areas, so that no ZnO could be deposited in these places.

## **4.2 Results and discussion**

### **4.2.1 Film growth and morphology**

Sulfonate-SAMs as substrates for deposition were prepared according to the routines described in the experimental section at the end of this chapter. The deposition solution was prepared by mixing solutions of zinc acetate and PVP in methanol and dropwise addition of a solution of tetraethylammonium hydroxide (TEAOH) in methanol, so that the final concentrations were  $[\text{Zn}^{2+}] = 10 \text{ mM}$ ,  $[\text{PVP}] \approx 10 \text{ mM}$ , and  $[\text{TEAOH}] \approx 25 \text{ mM}$ . In order to

determine the influence of PVP in solution on certain properties of films, the concentration of PVP was varied. For film deposition, a substrate was immersed in the deposition solution, and the solution was heated to 60 °C. In order to obtain thicker films in spite of exhaustion of the deposition solution, the substrate was placed in fresh solution every 1.5 hours. Experimental details of the deposition process are also given in the final section of the paper.

When the deposition solution is heated to 60 °C, particles are formed. Their mean size was measured by dynamic light scattering (Figure 4.1). One can clearly distinguish two stages of the process in solution. The first stage lasts about 1.5 to 2 hours. During this stage the particle size is constant. During the subsequent second stage, the particle diameter grows linearly. Obviously ZnO nanocrystals are present in solution during the first stage. In the second stage, these nanocrystals aggregate. According to Hansen et al. [91] heterogeneous aggregation is favoured over homogeneous aggregation. Therefore aggregation in solution does not happen immediately since aggregation on the substrate, i. e. film formation, is favoured over aggregation in solution. However formation of some aggregation nuclei in solution can never be prevented, and after a certain period of time they will also come into question as aggregation sites: on the one hand, at some point there will be so many of them that their total surface is much larger than the surface of the substrate, so the higher number of collisions with aggregates in solution will more than counterbalance the smaller sticking probability; on the other hand they grow in size so that the sticking probability increases for the adsorption of further nanoparticles. Finally the aggregates grow at the expense of film growth on the substrate; [92] hence film growth is disrupted in the second stage of the process, after some incubation time. Obviously the point when aggregation in solution takes over is reached after about 1.5 hours in the present deposition solutions. This limitation must be overcome for the deposition of thicker films, so the solution is removed from the reaction vessel after every 1.5 hours and replaced by fresh solution in order to circumvent aggregation in solution.

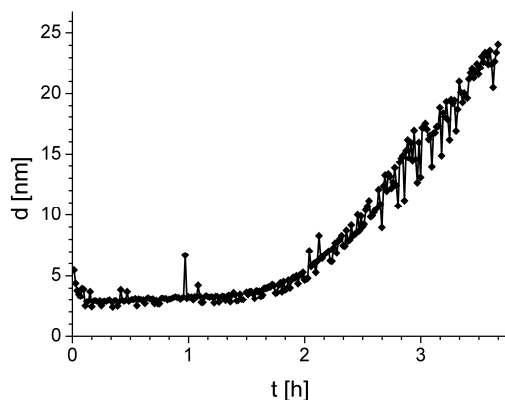


Figure 4.1: Evolution of the mean particle diameter at 60 °C in a solution initially containing 10 mM  $\text{Zn}(\text{CH}_3\text{COO})_2$ , 25 mM TEAOH and 10 mM PVP in methanol.

Aggregation in solution also accounts for another observation: The resulting film thickness does not improve if the volume of deposition solution in the reaction vessel is increased. Until the time when aggregation in solution takes over and film formation ceases, only a tiny share of the available amount of precursor is consumed even in small volumes of deposition solution.

The deposition process yields films which exhibit interference colours depending on their thickness. Scanning electron microscopy (SEM) images (Figure 4.2a) of the films show uniform coating, a rather smooth surface, and some residual porosity within the cross-section. The film appears to consist of grains with a size of only a few nanometers. The root of the mean squared deviation (RMS) in height as measured with atomic force microscopy (AFM) is used as a measure of roughness. According to Figure 4.2b, RMS values as low as 5 nm are found at film thicknesses of about 100 nm. Clearly this deposition method yields smoother films, a more uniform thickness, and a more homogeneous microstructure compared to previous approaches. [19,84] The reason is that the new routine rules out the formation of large aggregates in solution during the whole process, since the solution is exchanged before substantial growth of aggregates begins. When the substrates are left in the same deposition solution for longer times, the solution gradually turns turbid after a few hours at 60 °C, and only very rough films with thicknesses below 50 nm are deposited. The increased roughness is likely caused by sedimentation of aggregates from solution.



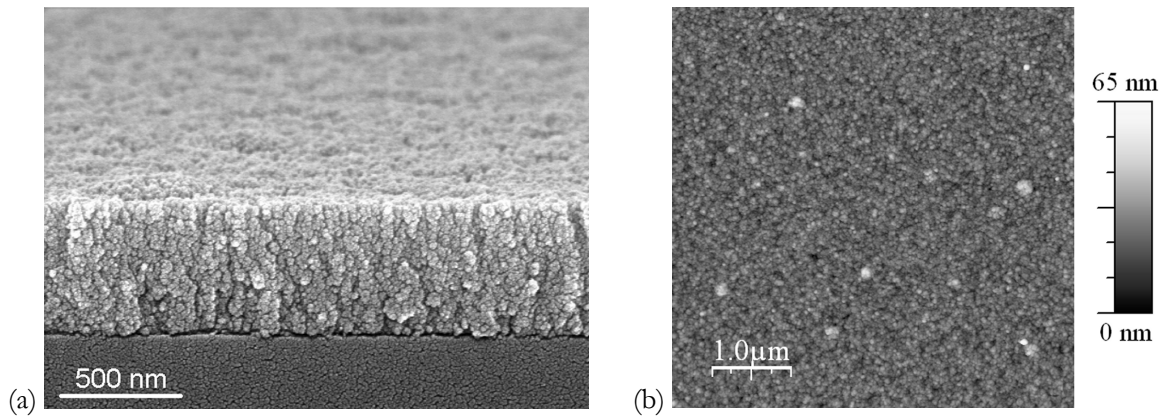


Figure 4.2: (a) Scanning Electron Microscopy image of a ZnO film made applying 20 deposition cycles. Cross-section tilted by  $10^\circ$ . (b) Atomic Force Microscopy image (height plot) of a ZnO film made applying nine deposition cycles, with a film thickness of 106 nm and a RMS roughness of 5.3 nm. Both samples were deposited from solutions with  $[\text{PVP}] : [\text{Zn}^{2+}] = 1 : 1$  at  $60^\circ\text{C}$ .

The average film thickness as obtained by evaluation of the SEM images depends nearly linearly on the number of deposition cycles, with an increment of 10 to 30 nm per deposition cycle for a molar ratio  $[\text{PVP}] : [\text{Zn}^{2+}] = 1$  in the deposition solution (Figure 4.3a). The increment is observed to be marginally higher in later deposition cycles than in earlier ones. The minor discrepancy is attributed to aging of the deposition solution during storage between preparation and application. The thickest films, which were produced, reach a thickness of nearly 600 nm after 20 deposition cycles of 1.5 hours each and a RMS value of 14 nm. It is apparent that even these films would have grown further if more deposition cycles had been applied. The roughness increases only very slightly with increasing film thickness (Figure 4.3a), which also indicates that it is governed mainly by the aging of the deposition solution.

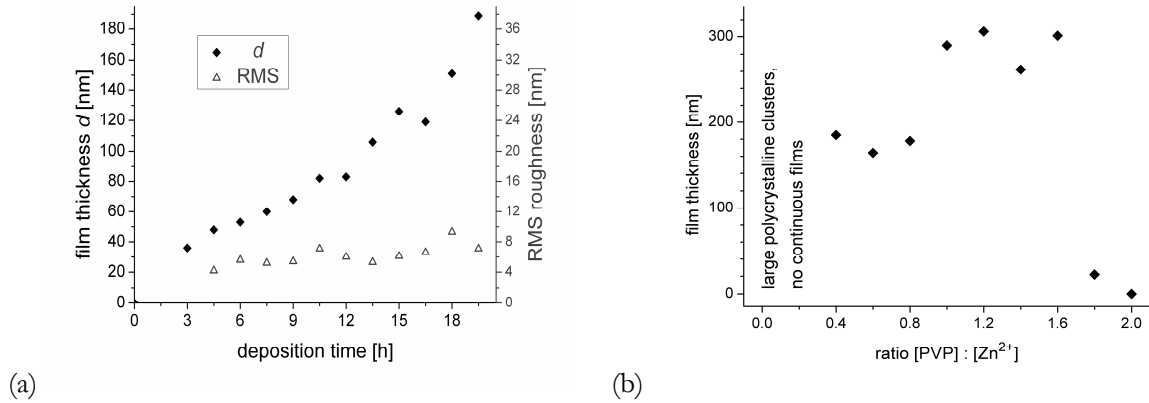


Figure 4.3: (a) Dependence of the film thickness and RMS roughness on the deposition time. A deposition time of  $n$  times 1.5 hours corresponds to  $n$  applied deposition cycles. The samples were deposited from solutions with  $[\text{PVP}] : [\text{Zn}^{2+}] = 1 : 1$  at  $60\text{ }^\circ\text{C}$ .

(b) Dependence of the film thickness on the PVP-Zn molar ratio in the deposition solution. The samples were made applying 20 deposition cycles at  $60\text{ }^\circ\text{C}$ .

The film thickness depends strongly on the molar ratio  $[\text{PVP}] : [\text{Zn}^{2+}]$  in the deposition solution, as it can be seen in Figure 4.3b. The maximum thickness occurs at a ratio of around  $[\text{PVP}] : [\text{Zn}^{2+}] \approx 1$ . Practically no continuous film is formed when the ratio is below 0.2 or above 2. This phenomenon can be explained as follows: Güner et al. have shown that the presence of block-copolymers in the deposition solution suppresses the crystal growth of ZnO: [27] without polymer, a broad distribution of particle sizes is obtained, including very large particles which make the formation of homogeneous nanostructured films impossible. With increasing polymer content in solution, the size distribution becomes narrower, and the average size becomes smaller, until finally only the smallest particles continue to be formed. It has also been reported that PVP is even more efficient in suppressing crystal growth of ZnO than block-copolymers: [60,84] It reduces the resulting crystallite size to a few nanometers only. Accordingly the concentration of the nanoparticles, which serve for the formation of the films, increases with increasing polymer content in solution, and thicker films will be the result of higher polymer contents. Very high polymer concentrations, however, favour the formation of amorphous matter in solution, [55] so that the deposition of crystalline ZnO thin films is not possibly any more above a certain critical polymer content.

The other parameters were optimized as well: The thickest films are obtained when the molar ratio  $[\text{TEAOH}] : [\text{Zn}^{2+}]$  is about 2.5, which is in agreement with the well-established fact that a slightly elevated pH promotes ZnO formation. [93] An increase in temperature results in

faster deposition and thicker films. However the highest temperature which could be applied was about 60 °C, due to the boiling point of methanol at 65 °C. At temperatures of 45 °C or below, no appreciable deposition occurs.

The adherence of the films was investigated qualitatively. The films are neither detached from the substrate by a simple tape-peel test with commercial adhesive tape (Tesa), nor by ultrasonication in water or in organic solvents, nor by heat treatment at several hundred °C. Furthermore, the films can be subjected to a standard sample preparation routine for cross-sectional TEM micrographs without delamination.

#### 4.2.2 Patterning

The deposition of zinc oxide films depends very sensitively on the surface properties of the substrate; the sulfonate-modified SAM is a suitable substrate for deposition, yet not the native silicon oxide layer on bare silicon. Therefore site-selective decomposition of the sulfonate-modified SAM using UV irradiation and a photomask proved to be a suitable means to pretreat the substrates in such a way that zinc oxide was deposited in selected areas only (Figure 4.4). When irradiated with deep UV light, the Si–C bond in the alkylsiloxane breaks and a silanol group is formed. [94] Hence the sulfonate functionality is removed from the illuminated areas. When the thus pretreated substrates undergo the usual deposition process, a uniform thin film of zinc oxide is deposited in the areas with intact SAM, which have been shadowed from irradiation, just as on unexposed samples. In contrast, no deposition at all occurs in the areas which have been irradiated (Figure 4.4a). So after deposition and rinsing with distilled water, no other chemical or physical after-treatment is necessary to remove possible surplus zinc oxide or other contamination from the irradiated areas; a highly selective deposition process takes place. A sharp step between uncoated and coated areas can be achieved when the photomask sits solidly on the substrate during irradiation, when the incident light is close to parallel (defocused), and when the irradiation time is long enough. The fringe region along coated areas was studied in detail with SEM (Figure 4.4b) and AFM. The width of the fringe region is only around 300 nm. In this region, partial coverage of the substrate and an increased roughness of the ZnO coating are observed. The uneven course of the boundary between empty and coated areas is in accordance with the roughness of the edges of the photomask, indicating that masks with smoother edges would provide even sharper fringes.

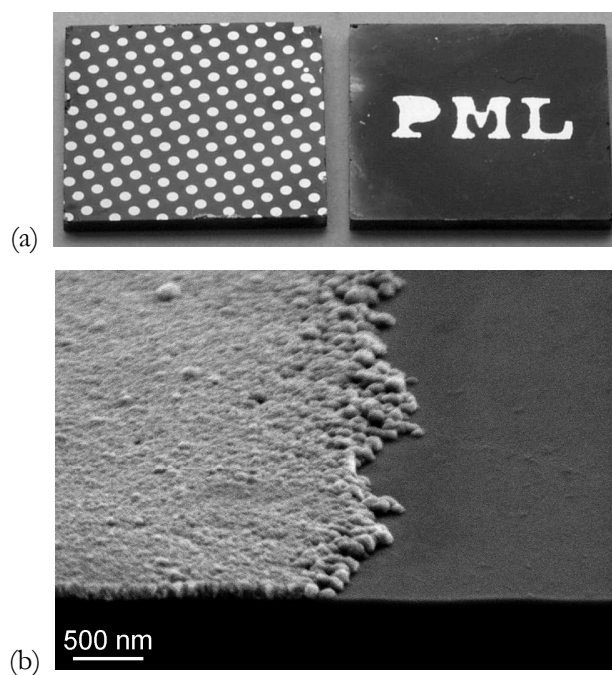


Figure 4.4: (a) Photograph of two  $10 \times 10 \text{ mm}^2$  silicon wafers coated with patterned ZnO films. The dark areas are the ZnO coating, while the bright areas are the blank Si wafer. (b) SEM image (cross-section tilted by  $20^\circ$ ) of the fringe region between the coated and uncoated areas of a patterned sample. The film thickness is 85 nm in the coated areas. All samples were deposited from solutions with  $[\text{PVP}] : [\text{Zn}^{2+}] = 1 : 1$  at  $60^\circ\text{C}$ , applying varied numbers of deposition cycles.

### 4.2.3 Composition

X-ray diffraction (XRD) and X-ray photoelectron spectroscopy (XPS) demonstrate that the films consist of ZnO. The X-ray diffraction diagram exhibits the peaks typical of ZnO with zincite structure: In Figure 4.5, the (100) reflection at about  $2\theta = 31.9^\circ$ , the (002) reflection at about  $34.7^\circ$ , and the (101) reflection at about  $36.6^\circ$  are clearly visible.

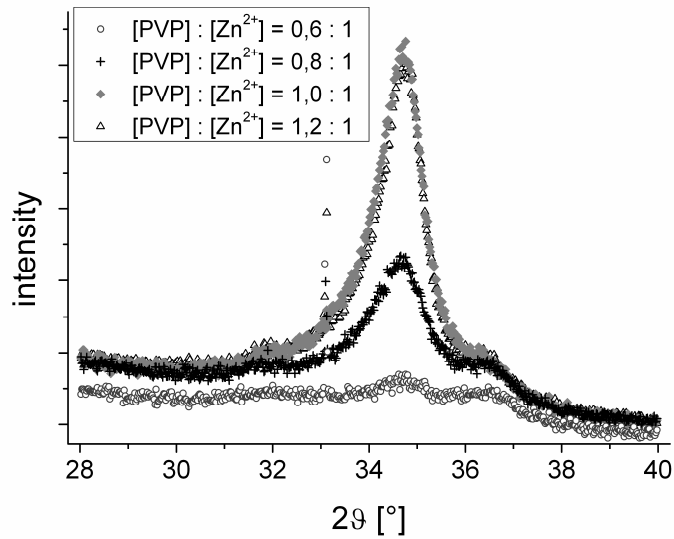


Figure 4.5: X-ray diffractograms of samples with the same deposition time ( $10 \times 1.5$  hours at  $60^\circ\text{C}$ ) and different  $[\text{PVP}] : [\text{Zn}^{2+}]$  ratios. The sharp peaks at  $33.1^\circ$  result from the single-crystalline silicon support.

XPS reveals the elements zinc and oxygen, and a minor amount of carbon. The oxygen 1s peak in XPS (Figure 4.6b) can be resolved into two components, where the component at the lower binding energy side (530.0 eV) is attributed to oxygen in zinc oxide, and the higher binding energy component (531.5 eV) is attributed to the hydroxylated oxide surface. Zn is present in the film in a single chemical environment (Figure 4.6c). The carbon 1s signal can be resolved into two peaks (Figure 4.6d). The component on the lower binding energy side (284.9 eV) is attributed to adventitious hydrocarbons; the one on the higher binding energy side (289.4 eV) may be due to residual acetate. No nitrogen 1s signal could be detected in Figure 4.6a, indicating that the nitrogen content of the oxide film is below about 1 at.-%. This means that the deposited zinc oxide film is virtually free of PVP. This result supports the notion that PVP only influences the processes in solution, but does not play a role in the actual film formation.

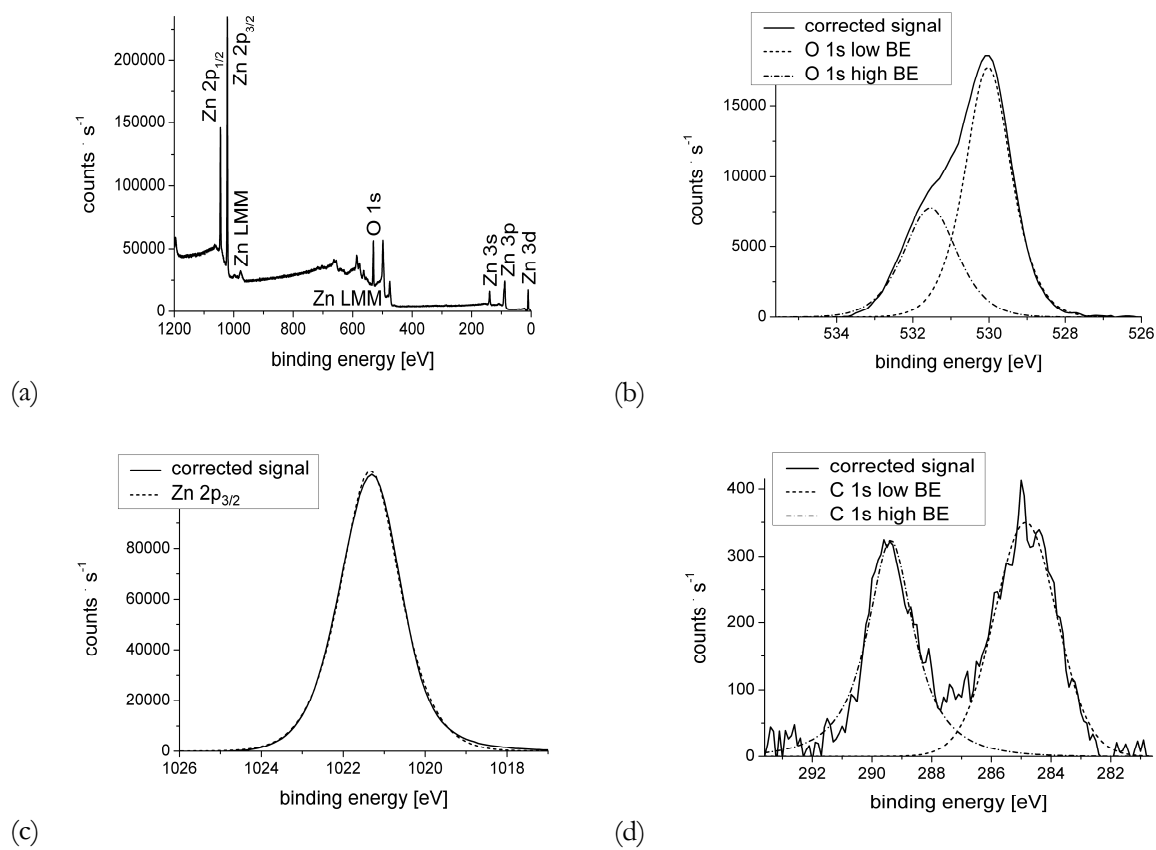


Figure 4.6: (a) X-ray photoelectron spectroscopy survey scan (raw data). Only Zn and O signals are present with appreciable intensity. (b) Oxygen 1s signal in XPS. (c) Zinc 2p<sub>3/2</sub> signal in XPS. (d) Carbon 1s signal in XPS. The solid lines in (b), (c), and (d) show the corrected data, i. e. the raw data after subtraction of a Shirley-type inelastic background; the broken lines are fits to the data. The sample was deposited from a solution with [PVP] : [Zn<sup>2+</sup>] = 1 : 1 at 60 °C, applying five deposition cycles.

#### 4.2.4 Microstructure and texture

XRD and transmission electron microscopy (TEM) substantiate that the films are nanocrystalline. In the X-ray diffraction diagrams (Figure 4.5), the three ZnO peaks are broadened strongly. Applying Scherrer analysis, an average grain diameter of 6 to 9 nm was calculated for typical samples with [PVP] : [Zn<sup>2+</sup>] ≈ 1 : 1. High-resolution transmission electron microscopy (HRTEM) images also show a nanocrystalline structure (Figure 4.7a) and grain sizes in accordance with the results from XRD investigations. These observations show that the broadening of the XRD peaks due to stresses in the crystallites is faint. This means it was justified that for

Scherrer analysis the whole peak broadening was attributed to crystal size effects, neglecting the effect of stresses in the crystallites.

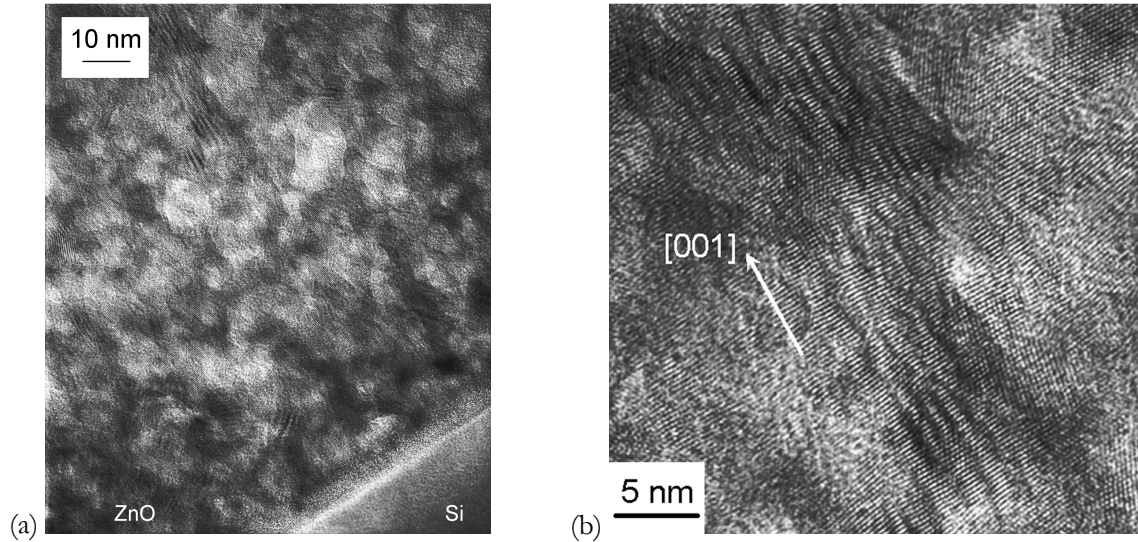


Figure 4.7: (a) Cross-sectional high-resolution transmission electron microscopy image of the bottom area of a ZnO film. (b) Enlarged section of the sample shown in (a). The  $\langle 001 \rangle$  direction of the crystallites is labelled. By comparison with (a), one can see that it is nearly perpendicular to the substrate. The moiré patterns along the diagonal of the image are indication of small-angle grain boundaries. The sample was deposited from a solution with  $[\text{PVP}] : [\text{Zn}^{2+}] = 1 : 1$  at  $60\text{ }^{\circ}\text{C}$ , applying ten deposition cycles.

Zinc oxide crystallites are polar because of the specific crystal structure of zincite. This polarity induces, on the one hand, a preferred orientation of the crystallites on the heavily charged surface of the SAM, on the other hand it enables the crystallites to perform oriented attachment to each other. Due to these effects, a texture emerges, which can be observed using X-ray diffraction methods. Accordingly, the (002) ZnO peak in the  $2\theta$  scan has a much higher intensity in the XRD diffractograms than the (100) and (101) peaks (Figure 4.6). In XRD diffractograms of very thick films, the (100) and (101) peaks are not even noticeable. For a sample with randomly oriented crystallites, the (002) peak would have been expected to be the weakest of the three. Hence its predominance indicates that the ZnO films are textured. The intensity ratios between the (002) peak and the other two peaks are highest for films deposited from solutions with molar ratios of about  $[\text{PVP}] : [\text{Zn}^{2+}] \approx 1$ ; in these films the crystallites are aligned best. The proof of a texture is provided by pole figures (Figure 4.8). An uncorrected 002 pole figure was measured for all rotational angles  $\Phi$ ; it indicated that the sample is fibre-textured. Taking this observation into

account, background-corrected pole figures were measured only for a single arbitrary angle  $\Phi$ . They show that the  $\langle 001 \rangle$  axis of the ZnO crystallites is preferentially oriented perpendicular to the substrate, the  $\langle 100 \rangle$  axis parallel to the substrate, and the  $\langle 101 \rangle$  axis with an angle of  $66^\circ$  to the perpendicular on the substrate.

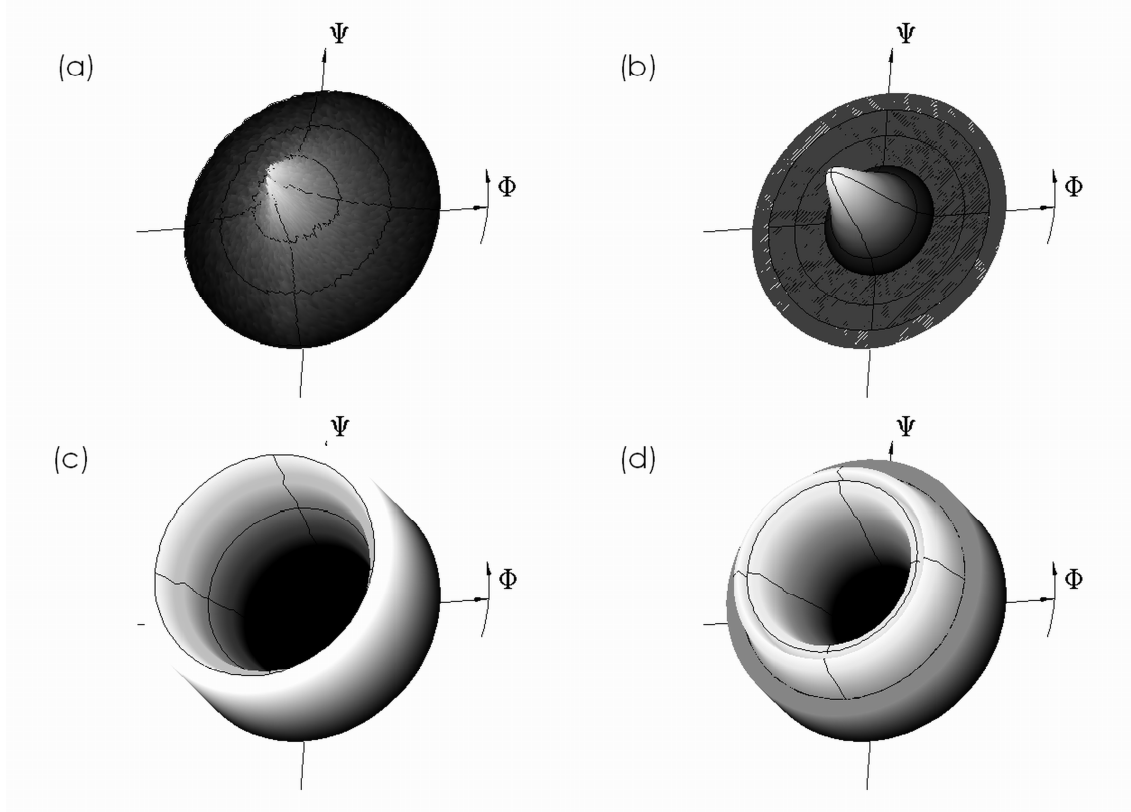


Figure 4.8: Pole figures of a ZnO film on a sulfonate-modified SAM on a glass support, deposited from a solution with  $[\text{PVP}] : [\text{Zn}^{2+}] = 1 : 1$  at  $60^\circ\text{C}$ , applying 20 deposition cycles. (a) Measured, uncorrected 002 pole figure, measured with tilting angles in the range  $\Psi = 0^\circ \dots 90^\circ$ . (b – d) Background-corrected pole figures derived from the integrated intensities of the measured diffraction lines for one arbitrary rotational angle  $\Phi$  and tilting angles in the range  $\Psi = 0^\circ \dots 80^\circ$ ; the range  $\Psi = 80^\circ \dots 90^\circ$  is shown in the same shade of grey as the value measured for  $\Psi = 80^\circ$  since no data was obtained for high tilting angles. (b) 002 pole figure. (c) 100 pole figure. (d) 101 pole figure.

The actual substrate for deposition is truly the sulfonate-modified surface of the organic SAM, not the silicon or glass support carrying the SAM. No interaction between ZnO and the supporting material is possible through the SAM; lattice-matching between the zinc oxide film and a crystalline support carrying the SAM is ruled out. Consequently, the same deposition



mechanism and films with the same kind of texture are expected for all kinds of support materials if they are covered with identical sulfonate-SAMs. Indeed congruent pole figures were obtained from ZnO films deposited on sulfonate-SAMs supported by silicon and on sulfonate-SAMs supported by quartz glass.

In high-resolution transmission electron microscopy (HRTEM) images (Figure 4.7b) the lattice spacings were determined to be 0.28 nm along the perpendicular to the substrate. This means that the  $\langle 001 \rangle$  axis is perpendicular to the substrate. The images reveal small-angle grain boundaries between adjacent crystal grains. This observation accounts for the broadening of the maxima in the pole figures. High-angle deviations from the preferred orientation are hardly found.

Heat treatment at temperatures below 800 °C does not change the appearance of the films as observed with the various microscopic methods. At temperatures above 800 °C, a chemical reaction between zinc oxide and the silicon substrate occurs. The topology of the film becomes smoother and more undulating, and cracks open up. A corresponding reaction between a zinc oxide film and its silicon substrate, albeit applying a sol-gel process for deposition, has been reported by Ji et al. [95] During heat treatment at 650 °C for 4 h, the grain size increases to 10 to 12 nm according to Scherrer analysis of XRD data. Simultaneously, the peak in the (002) pole figure becomes slightly sharper than before.

#### 4.2.5 Optical properties

When excited with near-UV light, the zinc oxide films are fluorescent. To the human eye, the photoluminescence is glaringly visible even at rather low excitation intensities and even in a laboratory lit by daylight; its apparent colour is a bright yellow. When excited at a photon energy of 3.8 or 4.1 eV, the emission spectrum can be resolved into three components (Figure 4.9a): a UV peak at about 3.4 eV, a green-yellow peak at about 2.3 eV, and a weak orange-red peak at about 1.8 eV. The presence of both a distinct visible peak and a sharp UV peak of similar intensity is unique: The intensity of the UV emission from the ZnO films presented in this paper is far higher than the intensity of the UV emission from smooth and uniform ZnO films deposited using different processes, which is hardly distinguishable from the background noise in the photoluminescence spectra. [96] Comparable UV emission intensities have only been reported from deposits consisting of much larger, rod-like crystals; [97] however these deposits lack smoothness and uniformity compared to the films presented here, and in most cases they show

hardly any photoluminescence in the visible range. The strong UV emission is evidence of a remarkable crystal quality in spite of the very fine-grained microstructure of the films.

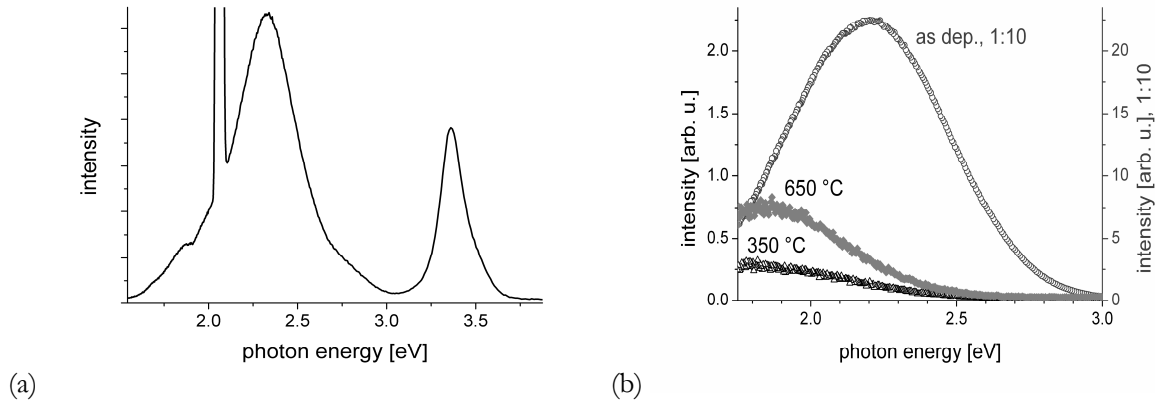


Figure 4.9: (a) Photoluminescence of a ZnO thin film as deposited. Emission spectrum for excitation at a photon energy of 4.1 eV. The truncated peak at 2.05 eV is the second harmonic of the excitation beam. The sample was deposited from a solution with  $[\text{PVP}] : [\text{Zn}^{2+}] = 1 : 1$  at 60 °C, applying 20 deposition cycles. (b) Photoluminescence of ZnO thin films, as deposited, and after four hours of heat treatment at 350 °C and 650 °C respectively. Emission spectra for excitation at a photon energy of 3.8 eV; here the second harmonic of the excitation beam was suppressed by a long-pass filter. The intensity values for the as-deposited sample are scaled down by a factor of ten for better comparability with the spectra of the heat-treated samples. The samples were deposited from a solution with  $[\text{PVP}] : [\text{Zn}^{2+}] = 1 : 1$  at 60 °C, applying five deposition cycles.

ZnO is a semiconductor with a wide band gap of 3.37 eV at room temperature; therefore the observed UV peak clearly results from band-edge emission. There is a controversy about the origin of the green-yellow and the orange-red peak in the literature. [96] The prevalent and most plausible explanation is that the green-yellow fluorescence originates from singly ionized oxygen vacancies at the surface of zinc oxide, [98,99] whereas the orange-red fluorescence is caused by oxygen-rich states. [100] Indeed, the high inner surface area induced by the nanocrystallinity of the film promotes green-yellow fluorescence, which disappears rapidly when the sample is heated in air so that oxygen vacancies can be filled (Figure 4.9b). Accordingly, a slow decline of the green-yellow fluorescence within several months is observed when the sample is stored in air at room temperature. In contrast, the intensity of the orange-red peak increases when the sample is heated to 650 °C in air. After heat treatment at temperatures of 800 °C or more, no photoluminescence is recorded; this observation is attributed to the reaction of the ZnO with the

Si support. [95] Patterned ZnO films exhibit the same photoluminescent properties as continuous films.

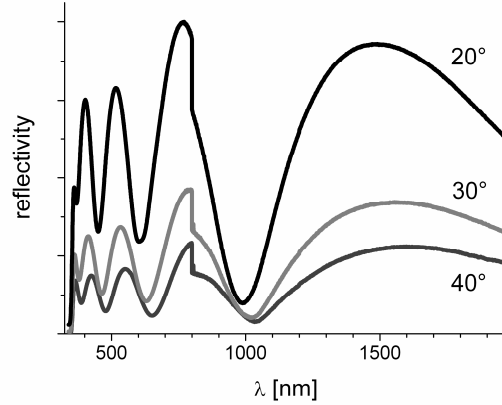


Figure 4.10: Reflectance spectra of a ZnO film with a thickness of about 580 nm at three different angles of incidence. The step at 800 nm is due to changeover of the light source and the grating in the instrument. The sample was deposited from a solution with  $[PVP] : [Zn^{2+}] = 1 : 1$  at 60 °C, applying 20 deposition cycles.

For visible light, the transmittance of the ZnO films is more than 85 %. In the near-UV, there is a sharp absorption edge at about 345 nm, below which the transmittance is much lower. The actual transmittance for UV light depends on the film thickness. To visible and near-IR light, silicon is a perfect mirror whereas the zinc oxide thin films are transparent. So when the reflection of light at the samples is studied, one observes interference of light which is reflected at the ZnO-air interface with light which is reflected at the Si-ZnO interface (Figure 4.10). If spectra are recorded for several different angles of incidence  $\theta$ , in principle both the refractive index  $n$  and the thickness  $d$  of the thin film can be determined by fitting of the formula

$$2d \cdot \sqrt{n^2 - \sin^2 \theta} = \frac{1}{m} \cdot \sum_{\nu=1}^m \left| \frac{1}{\lambda_{\nu}} - \frac{1}{\lambda_{\nu-1}} \right|^{-1} \quad \text{for } m \text{ interference fringes at the wavelengths } \lambda_{\nu}.$$

However this method is only feasible for the thickest films: only for them the number of interference fringes is high enough for evaluation in a wavelength interval where the refractive index of ZnO does not change too much. In this study the reflectance spectrum is evaluated between 340 to 800 nm. The film thickness as determined by SEM can be verified: in the SEM images, a local film thickness of 581 nm is observed, whereas the evaluation of the reflectance spectra yields a value of  $(556 \pm 22)$  nm. Using the RMS value of 14 nm as error bar for the determination of the film thickness from SEM images, the two values are in good agreement. The refractive index of

the film is about 1.6, which is lower than 2.0, which one would expect for bulk ZnO. The obvious reason for the difference is the porosity of the film.

#### **4.2.6 Deposition mechanism**

The described deposition process yields smooth and homogeneous ZnO films with a nanocrystalline, textured structure, whose favourable properties have been discussed in this article. For the formation of nanocrystalline ZnO films on sulfonate-modified SAMs in the presence of PVP, a deposition mechanism is proposed, which is in agreement both with the experimental results and with the prevailing theoretical conceptions.

At PVP concentrations applied in this study, interpenetration of the polymer chains is to be expected. [101] In other words, before the beginning of the deposition, a network of PVP molecules is present throughout the liquid. When the solution is heated, thermohydrolysis of the soluble precursor starts, and seed crystals of insoluble zinc oxide are formed. Interaction with the ubiquitous polymer prevents further growth of the ZnO seed crystals; they are preserved as roughly spherical nanocrystals. In the virtually anhydrous environment of this process, in which hydrolysis of soluble zinc salts is slower and therefore easier to control than in water-containing solutions, PVP is able to inhibit crystal growth more efficiently than in the previously used water-containing solutions. The ZnO nanocrystals are electrostatically attracted to the sulfonate-modified substrate which carries a negative surface charge under the present conditions, and they adsorb to it consequently. [84] A strongly negative surface charge is crucial – the weaker negative surface charge of the native oxide on the bare silicon wafer is not sufficient to make bare silicon a suitable substrate for deposition. At the same time, the ZnO nanocrystals form aggregates in solution. However, as described in detail above, film formation on the substrate is favoured, and aggregation becomes significant only after some incubation time, when a sufficient number of aggregation nuclei has been formed. When the critical point has been reached, aggregation takes over and film formation dies down.

### **4.3 Conclusions**

A new process for the deposition of zinc oxide from solutions at near-ambient conditions was developed and optimized. Mineralization takes place in methanol. This organic solvent does

not catalyse the hydrolysis of the soluble precursor; thus it was possible to use a network of PVP pervading the solution in order to direct the formation of nanocrystals in solution and prevent their growth towards micrometer-sized crystals. The nanocrystals adsorb to organic self-assembled monolayers with sulfonate functional groups. Smooth, homogeneous, uniform and porous films are formed, which consist of textured nanocrystalline zinc oxide. The thickness of the films can be tuned arbitrarily via the number of deposition cycles, whereas the roughness remains nearly constant throughout the deposition process. When the self-assembled monolayer on the substrate is photolysed in selected areas, zinc oxide is only deposited in the areas with intact SAM. Thus patterned films can be obtained.

The films exhibit photoluminescence in the orange-red, green-yellow and ultraviolet region; they are transparent for visible and infrared light, but opaque for ultraviolet light. Apart from its simplicity and frugality, and apart from the possibility to fine-tune structure and properties of the deposits, chemical bath deposition has two major advantages: As no direction is favoured above others in solution, arbitrarily shaped substrates can be coated. Furthermore deposition takes place at near-ambient temperature, so the deposition of metal oxides by this method is not detrimental to biomolecules; therefore in principle it is possible to build composite or hybrid nanostructures consisting of both metal oxides and biomolecules. The formation of ZnO films on curved substrates and the fabrication of biocomposites of ZnO are currently under investigation.

## **4.4 Experimental**

### **4.4.1 Substrate preparation and patterning**

Polished p-type boron-doped single-crystal Si (100) wafers are used as supports for self-assembled monolayers (SAMs). Prior to use, they are cleaned by wiping with chloroform, acetone, and ethanol. Subsequently, they are oxidized in Piranha solution for one hour at 90 °C and washed abundantly with distilled water afterwards. Piranha solution is mixed freshly prior to use out of 7 volume units concentrated H<sub>2</sub>SO<sub>4</sub> and 3 volume units H<sub>2</sub>O<sub>2</sub> (30 wt.-% in water). Alternatively, slides of quartz glass are used as substrates. They are also wiped with chloroform, acetone and ethanol prior to use, but they do not undergo Piranha treatment.

The actual substrate for ZnO deposition is a SAM of sulfonate-modified alkylsiloxanes chemically bound to a glass slide or to the native silicon oxide on top of a silicon wafer. SAM deposition takes place under argon atmosphere. 1-thioacetato-16-trichlorosilyl hexadecane is synthesized according to established procedures [102,65] and dissolved in toluene to a concentra-

tion of 2 vol.-%. The surface-oxidized silicon wafers or glass slides are immersed in the solution and kept there for 5 hours. During deposition, the solution is cooled to about 10 °C and sonicated in an ultrasonic bath. Afterwards, the substrates are washed with chloroform and methanol. The thioacetate functionality is oxidized to sulfonate by placing the substrates in a saturated aqueous solution of potassium hydrogen monopersulfate for at least 12 hours. Subsequently, the substrates are washed abundantly with distilled water and dried in a stream of argon. If the SAM-covered substrates cannot be used for ZnO deposition immediately, they are kept in the dark.

In order to deposit ZnO selectively in certain areas of the substrate only, after SAM deposition and oxidation the substrate is partially covered with a metal mask and illuminated with a deuterium lamp (Lot Oriel) for 48 hours. The spectrum of the lamp is continuous between 180 and 370 nm. Dulcey et al. have shown that the Si-C bond in self-assembled monolayers can be broken by deep UV irradiation at both 193 and 248 nm. [94] As photomasks, steel foils with a thickness of 25 µm and etched hole patterns are used.

#### 4.4.2 Deposition solution and deposition

Special care is taken to keep the deposition solution free of water, which would catalyse the decomposition of zinc acetate into zinc oxide and thus make the process more difficult to control. Therefore vessels are dried carefully, and reagents of high purity are used. For a precursor solution with  $[PVP] : [Zn^{2+}] = 1,0$ ,  $Zn(CH_3COO)_2 \cdot 2 H_2O$  (puriss. p. a., Fluka) is dissolved in methanol (VLSI selectipur, BASF) to a concentration of 40 mmol·l<sup>-1</sup>. With the aid of ultrasound, polyvinylpyrrolidone (PVP10, Sigma-Aldrich) with an average molecular weight of 10 000 g·mol<sup>-1</sup> is dissolved in methanol to a concentration of 20 mmol·l<sup>-1</sup>. 1 volume unit of the zinc acetate solution is mixed with 2 volume units of the PVP solution. Under gentle stirring, 1 volume unit of a solution of tetraethylammonium hydroxide (TEAOH, purum, Fluka) in methanol with a concentration of 100 mmol·l<sup>-1</sup> is added dropwise using a peristaltic pump at a flow rate of 1.5 ml·min<sup>-1</sup> for a volume unit of 45 ml, or 1.0 ml·min<sup>-1</sup> for a volume unit of 22.5 ml. For precursor solutions with different  $[PVP] : [Zn^{2+}]$  ratios, the zinc acetate and TEAOH concentrations are kept constant while the PVP concentration is adapted accordingly. To prevent evaporation of the solvent or premature ZnO formation, the precursor solution is stored in a closed jar at 4 °C and used within ten days after preparation. An analogue recipe has already been used for the deposition of ZnO in the presence of PEG. [84]

For deposition, a 10 × 10 mm<sup>2</sup> Si wafer or glass platelet coated with a sulfonate-modified

---

SAM is placed in a 1 ml aliquot of precursor solution in a closed jar, which is heated to 60 °C in an oil bath. Alternatively, up to twelve substrates are immersed in 22.5 ml of precursor solution in a specially designed reaction vessel at 60 °C. After 1.5 hours the solution is replaced by fresh deposition solution. Up to 20 such cycles are conducted before the substrate is removed and washed abundantly with distilled water.

### 4.4.3 Sample characterization

To determine particle sizes in solution, dynamic light scattering with subsequent photon correlation is done with a Malvern Zetasizer 3000HS. Particle size distributions were calculated from the correlograms using the non-negative least squares (NNLS) fitting method.

Scanning electron microscopy (SEM) is done using a JEOL JSM-6300 F with an accelerating voltage of 3 kV and a working distance of 15 mm and a Zeiss DSM 982 Gemini at accelerating voltages of 3 to 5 kV and working distances of 3 to 5 mm. Cross-sectional specimens for SEM are obtained by scarification of the substrate with wire-cutting pliers and subsequent manual cleaving.

Atomic force microscopy (AFM) images are recorded with a Digital Instruments Nanoscope III applying tapping mode with silicon cantilevers.

X-ray photoelectron spectroscopy (XPS) is performed with a Thermo VG Thetaprobe 300 system using monochromatic incident Al K $\alpha$  radiation ( $h\nu = 1486.68$  eV; spot size 400  $\mu\text{m}$ ). Energy calibration, removal of contaminations and charge compensation during the measurements are done according to established procedures. [25] Detailed spectra of the Zn 2p, the O 1s, and the C 1s signals are measured with a pass-energy of 100 eV and a step size of 0.1 eV. Spectral decomposition of the spectra is done for each spectral region by subtraction of a Shirley-type inelastic background and subsequent fitting with one or more mixed Gaussian-Lorentzian peak components. The binding energy (BE) scales are aligned by referencing the resolved C 1s main peak to the corresponding value for adventitious carbon of 284.8 eV. [26]

X-ray diffraction (XRD) diagrams are taken with a Philips X'Pert instrument in Bragg-Brentano geometry using only Cu-K $\alpha_1$  radiation by means of a primary monochromator. Scherrer analysis of the diffraction diagrams is done in the following way: Three Lorentz maxima with interdependent full widths at half maximum (FWHM)  $\gamma$  are fitted to the (100), (002), and (101) peaks of the ZnO diffraction diagram. The average crystallite diameter  $d$  is then calculated using

the Scherrer formula:  $d = \frac{0.94 \cdot \lambda}{\gamma \cdot \cos \theta}$ , where  $\lambda$  is the source wavelength, and  $2\theta$  the peak position.

For X-ray texture analysis, pole figures are recorded with a Philips MRD with an Eulerian cradle employing Cu-K $\alpha$  radiation. Background-corrected pole figure sections for ZnO 100, 002 and 101 reflections are derived from integrated intensities of the diffraction lines measured at tilting angles  $\Psi$  from 0° to 90° and an arbitrary rotational angle  $\Phi$ .

For transmission electron microscopy (TEM), a JEOL JEM-4000 FX with an accelerating voltage of 400 kV is used. Cross-sectional specimens for TEM are prepared according to the method established by Strecker et al. [103] Lattice spacings are determined using two-dimensional Fast Fourier Transformation (FFT) of selected areas of high-resolution TEM images.

Photoluminescence measurements are done with a spectrofluorometer (Spex FluoroLog 3, Horiba Jobin Yvon).

Optical transmittance and reflectance spectra are recorded with a Cary 5000 UV-Vis-NIR spectrometer (Varian Inc.). For transmittance spectra, thin films on glass substrates are measured, for reflectance spectra films on silicon substrates. The final data are obtained by comparing the measured data with baseline measurements of bare glass or silicon substrates respectively.

Unless otherwise indicated, all measurements presented in this paper were done with zinc oxide films deposited on SAMs on silicon supports. However, as far as possible all measurements were repeated with films deposited on SAMs on glass supports, and no noticeable differences were found. This congruence was expected, since ZnO deposition does not happen directly on the inorganic support, but on the sulfonate-modified surface of the organic SAM, which is identical in both cases.

## 4.5 Acknowledgements

The authors wish to thank Dr. Lars P. H. Jeurgens and Michaela Wieland for doing the XPS measurements, Maritta Dudek and Gerd Maier for recording the XRD diffractograms and pole figures, Sabine Kühnemann and Hartmut Labitzke for taking the SEM images, Peter Gerstel for the synthesis of the alkylsiloxanes and for general support in the Chemistry laboratory, and Prof. Lennart Bergström and Dr. Niklas Hedin for valuable discussions.







**5. Time evolution of zinc oxide particle formation and assembly of oriented nanocrystalline films in methanol**

## Abstract

Zinc oxide thin films are mineralized from solutions at near-ambient temperature applying the principles of bio-inspired materials synthesis. Zinc oxide is formed in methanol by thermal hydrolysis of soluble zinc acetate. The polymer polyvinylpyrrolidone (PVP) is dissolved in the precursor solution in order to induce the formation of textured polycrystalline zinc oxide films. Film deposition is possible on substrates with high surface charges, whether positive or negative. Film deposition happens via particle formation in solution and adsorption to the substrate. However classical descriptions via nucleation, growth, and steric repulsion fail to explain the observations. When the precursor solution is heated slightly, amorphous spicular particles are formed within the first minutes. After some delay time, these “needles” dissolve again and give way to the formation of aggregates of polycrystalline ZnO, which continue to grow with a linear increase in diameter with time. Film deposition on the substrate also starts immediately after heating-up, with its rate continuously decreasing due to increasing competition with aggregation in solution. Two mechanisms dominate the process: firstly depletion interaction between the polymer molecules and the particles in solution, and secondly oriented attachment both among the particles and between the particles and the substrate.

## 5.1 Introduction

Soft solution processing (SSP) has become known as a simple and economical method of synthesizing ceramics. [9] To connect SSP with the principles of bio-inspired materials synthesis means using organic templates and organic structure-directing agents in solution. Thin films of a vast number of materials have been produced applying this method. [45] However, only a few experiments and simulations have been conducted trying to investigate the mechanisms of mineralization in such solutions. Model concepts were proposed, [104] but they were often speculative.

Traditionally, the crystallization process is described in terms of nucleation events and growth processes. Two different mechanisms of nucleation have become textbook knowledge: In the case of homogeneous nucleation, [105] molecules or ions accumulate statistically to form a nucleus in the interior of a uniform substance. In the case of heterogeneous nucleation, [106] however, crystallization commences on a nucleus that has a different composition, or on a substrate. Mersmann et al. have given a comprehensive account of the established theories of crystallization. [107] Organic additives can prevent nucleation, disperse small particles, or inhibit crystal growth. [108] These manifold effects can be exploited for the preferential fabrication of certain crystal structures. Often unexpected crystal morphologies have been explained by molecules specifically adsorbing to certain faces of the growing crystals and thus directing the growth. [27] In this context, the interaction of polymers with the surface of  $\text{CaCO}_3$  has been explored using molecular dynamic simulations. [109] For the special case of zinc oxide, Sounart et al. have given an overview over recent research on the sequential nucleation and growth of complex structures. [110]

In solution processes for film deposition, particle formation in solution and subsequent adsorption to the substrate are often crucial. Accounting for this observation, Shin et al. have presented a theoretical model based on the DLVO theory, [111] and Niesen et al. have sought experimental evidence for this model. [112] Concentrating more on the processes in solution than on the substrate, Cölfen et al. have recognized, and investigated, the intimate relationship between the deposition of zirconia thin films on organic self-assembled monolayers (SAM) and particle formation in the precursor solution during chemical bath deposition (CBD). [113] Okudera and Yokogawa were among the first to realize that concurrent aggregation in solution and film growth on a substrate may occur via identical mechanisms and therefore compete with each other. [92]

Materials mineralized in solutions, whether in biological or artificial environment, frequently exhibit a hierarchical internal structure, which cannot be explained by the traditional concepts

of ion-by-ion growth and non-directional aggregation. [114] Analysing the early stages of such processes, it was found that when colloidal particles are formed in solution, they can attach to each other, adopt congruent crystallographic orientation, and fuse together. [115] For these phenomena, the term “oriented attachment” has been coined. [67,116] The adaptation of crystallographic orientation may happen by contact epitaxy, i. e. by internal rearrangement of the molecules or ions in the attaching crystallite. [117] Oriented attachment is responsible for the formation of highly oriented superstructures composed of nanocrystalline building blocks, so-called mesocrystals, [118] and it has been suggested as the cause of the formation of oriented domains in zinc oxide thin films deposited from solutions. [84]

Amorphous structures have been identified as an intermediate stage of crystallization in biomineralization, [2,119] for example during the formation of spines of larval [120] and adult [121] sea urchins, mollusc larval shells, [122,123] the carapace of crabs, [124] and the teeth of chitons. [125,126] It has also been proposed that hybrid nanoparticles, containing amorphous inorganic matter in an organic matrix, are precursors for the crystalline matter. [114]

In a previous publication, a method for the synthesis of nanostructured zinc oxide thin films on organic templates via a bio-inspired approach has been introduced. [127] An in-depth discussion of the morphology and properties of the ZnO films deposited by that method has been presented and will not be iterated here. In fine, the films deposited were smooth, polycrystalline, textured and fluorescent. Their thickness could be adapted arbitrarily by applying various numbers of deposition cycles. Two properties of the films must be emphasized because of their major relevance for the interpretation of the deposition mechanism: The polymer content of the films is evanescently low, and the films exhibit a pronounced fibre-texture with the [001] axis perpendicular to the substrate.

Considering the polycrystallinity of the films, an attempt to explain the deposition mechanism in terms of polymer-mediated oriented attachment was made in the mentioned paper. However, as the processes in solution had not been studied, no experimental data was available supporting the propositions. In particular, the role of the polymer remained unclear, and in what way and by what mechanisms it determines the structure and the properties of the films at various concentrations.

Now, a comprehensive study of the processes in the deposition solution has shed more light on the processes both in solution and on the substrate, so that a detailed account of the mechanism can be given. It has been found that the mineralization process of ZnO is rather complex, including amorphous interstages and manifold effects of the participating organic substances. Furthermore, evidence will be presented that the polymer molecules do not control film for-

mation simply by adsorbing to the seed crystals, but that they control the process by tuning the kinetics, and possibly the equilibria, of several reaction steps.

Inspired by the observations made on the deposition solutions, the need was recognized for further experiments elucidating the kinetics of film formation on a substrate, and the influence of the substrate and the polymer concentration on the film morphology.

## 5.2 Experimental

### 5.2.1 Substrate preparation, deposition solution and deposition

Self-assembled monolayers (SAM) are used as substrates for the deposition of ZnO films. Substrates and deposition solutions are prepared analogously to methods described elsewhere. [127] Polished p-type boron-doped single-crystal Si (100) wafers are used as supports for the SAMs. The wafers are cleaned by sequentially applying chloroform, acetone, and ethanol. Subsequently, their surfaces are oxidized in a Piranha solution for one hour at 90 °C and washed abundantly with distilled water afterwards. The Piranha solution is mixed freshly prior to usage out of seven volume units concentrated H<sub>2</sub>SO<sub>4</sub> and three volume units H<sub>2</sub>O<sub>2</sub> (30 wt.-% in water).

For the formation of a SAM of sulfonic acid modified alkylsiloxanes, 1-thioacetato-16-trichlorosilyl hexadecane is synthesized, [65,102] dissolved in toluene (2 vol.-%), and chemically bound to a surface-oxidized silicon wafer. The surface-oxidized silicon wafers, or glass slides, are immersed in cooled toluene based solution (4 °C for 5 h, argon atmosphere) and thereafter rinsed with chloroform and methanol. The thioacetate functionality is oxidized to a sulfonic acid moiety by placing the substrates in a saturated aqueous solution of potassium hydrogen monopersulfate for at least 12 hours. Subsequently, the substrates are washed abundantly with distilled water and dried in a stream of argon and stored in the dark. Alternatively, a SAM of amino-modified alkylsiloxanes is used. It is produced from 1-cyano-16-trichlorosilyl hexadecane [102] reacted with the surface oxidized wafers as described above. The cyano functionalities are reduced to amino groups by placing the substrates in a saturated solution of LiAlH<sub>4</sub> in absolute diethyl ether for at least 12 hours. Subsequently, the substrates are washed abundantly with pure ether and immersed in an aqueous 10 vol.-% HCl solution for protonation of the functional groups. Finally the substrates are dried in a stream of argon at room temperature.

Methanolic solutions of zinc acetate, polyvinylpyrrolidone (PVP), and tetraethylammonium hydroxide (TEAOH) are used to form and deposit ZnO-nanoparticles. Zn(CH<sub>3</sub>COO)<sub>2</sub> · 2 H<sub>2</sub>O (puriss. p. a., Fluka) is dissolved in methanol (VLSI selectipur, BASF) to a concentration of

40 mmol·l<sup>-1</sup>. PVP (Sigma-Aldrich,  $M_w \sim 10\,000$  g·mol<sup>-1</sup> or 40 000 g·mol<sup>-1</sup>) is dissolved in methanol. The zinc acetate solution is mixed with the PVP solution. Under gentle stirring, tetraethylammonium hydroxide (TEAOH, purum, Fluka, 100 mmol·l<sup>-1</sup> in methanol) is added drop by drop within about 25 minutes using a peristaltic pump. A typical composition is  $[Zn^{2+}] = 10$  mmol·l<sup>-1</sup>,  $[TEAOH] \approx 25$  mmol·l<sup>-1</sup>, and  $[PVP] \approx 10$  mmol·l<sup>-1</sup> (a volume fraction of  $\phi \approx 0.10$ ). The concentration and molecular weight of PVP are varied keeping the zinc acetate and TEAOH concentrations constant.

For deposition, a  $10 \times 10$  mm<sup>2</sup> Si wafer coated with a SAM is placed in a 1 ml aliquot of precursor solution in a closed jar heated to 60 °C in an oil bath. After 1.5 hours the solution is replaced by fresh deposition solution. Up to 20 such cycles are conducted before the substrate is removed and washed abundantly with distilled water. For investigation of the processes active in solution, the solutions are heated to 60 °C in closed jars in an oil bath or an oven, and quenched to room temperature in a water bath after the desired reaction time.

### 5.2.2 Sample characterization

In order to determine the particle sizes in solution, dynamic light scattering (DLS) experiments are performed using a Malvern Zetasizer Nano ZS device. From the time evolution of the scattering intensity, an autocorrelation function is calculated. The monomodal exponential decay

function  $g = A + c \cdot \exp\left(-\frac{2 \cdot t}{\tau}\right)$ , or, if no sufficient accordance could be reached, the bimodal exponential decay function

$g = A + \left(c_1 \cdot \exp\left(-\frac{t}{\tau_1}\right) + c_2 \cdot \exp\left(-\frac{t}{\tau_2}\right)\right)^2$  is fitted to the correlation function, using  $A$ ,  $c_i$ , and  $\tau_i$  as fit parameters. The diffusion constant is then  $D = \frac{1}{q^2 \cdot \tau}$ . Here

$q = \frac{4\pi \cdot n}{\lambda} \cdot \sin \mathcal{G}$  is the wave vector of the scattered beam.  $\mathcal{G}$  is the angle between the incident beam and the scattered beam in the DLS set-up,  $\lambda$  is the wavelength, and  $n$  is the refractive index of the medium. From the diffusion constant, the diameters of the diffusing particles are calculated using  $d = \frac{k_B T}{3\pi \cdot \eta \cdot D}$ .  $k_B$  is the Boltzmann constant,  $T$  is the absolute temperature, and  $\eta$  is the viscosity. In order to monitor the reaction and aggregation processes in the solution over a certain period of time, a sample cell containing the solution is heated to 60 °C inside the Zeta-



sizer, and photon correlation measurements with integration times of e. g. one minute are done repeatedly. The zeta potential of the particles in solution and the conductivity of the solutions are determined using the Malvern Zetasizer Nano ZS and applying the automated evaluation routines of the provided software.

Using a Thermo Haake RheoStress<sup>1</sup> rheometer, a viscosity of 2 cP is measured at 60 °C for a solution with 10 mmol·l<sup>-1</sup> PVP. For solutions without polymer, the literature value for pure methanol at standard temperature (0.55 cP) is used. For other PVP concentrations the viscosity is linearly interpolated.

For monitoring film growth on a substrate, a quartz crystal microbalance (RQCM, Maxtek Inc.) is used. As substrates, sulfonate-SAMs are deposited on quartz crystals with gold electrodes and a silica layer on the outer surface according to the procedures outlined previously. The measurements are performed in a closed reaction chamber with a heating coil connected to a thermostat.

For scanning electron microscopy (SEM), a JEOL JSM-6300 F with an accelerating voltage of 3 kV and a working distance of 15 mm is used. Cross-sectional specimens of the deposited films were obtained by cracking the brittle Si or glass substrate bearing the film. Using wire-cutting pliers, a small notch was made on the substrate edge to control the position of the crack.

For transmission electron microscopy (TEM), a JEOL JEM-4000 FX with an accelerating voltage of 400 kV, and a JEOL JEM-3010 operating at 300 kV are used. Images from the JEM-4000 FX are captured on electron image film (Kodak) and from the JEM-3010 on a CCD camera (Keen View, SIS Images). Samples of particles from the deposition solution are obtained by repeated dripping of a few drops of the solution on a copper TEM grid with a lacy carbon film (Plano or Okenshoji) and subsequent evaporation of the solvent at ambient conditions.

Atomic force microscopy (AFM) images are recorded with a Digital Instruments Nanoscope III operating in the tapping mode with silicon cantilevers.

X-ray diffraction (XRD) diagrams are taken with a Philips X'Pert diffractometer in Bragg-Brentano geometry using only Cu-K $\alpha_1$  radiation by means of a primary monochromator. Scherrer analysis is performed: Three Lorentz maxima with interdependent full widths at half maximum (FWHM)  $\gamma$  are fitted to the (100), (002), and (101) peaks of the ZnO diffraction diagram. The volume-weighted domain size  $d$  in the direction parallel to the diffraction vector is then calculated using the Scherrer formula:  $d \approx \frac{\lambda}{\gamma \cdot \cos \theta}$ , where  $\lambda$  is the wavelength, and  $2\theta$  the peak position.  $d$  is as a measure of the average particle size. Instrumental peak broadening is neglected since it is insignificant compared to the peak broadening because of grain size effects. Representen-

tative samples from PVP-free dispersions are prepared for XRD analysis by centrifugation at 1000·g for 45 minutes. The supernatant is replaced by pure methanol, the sediment is redispersed, the dispersion is centrifuged again and the supernatant decanted. Finally the sediment is dried. Samples from PVP-containing solutions are prepared for XRD by repeatedly dripping some drops of solution on a silicon wafer and subsequently evaporating the solvent at room temperature.

<sup>13</sup>C NMR spectra are measured using a Bruker Avance 250 spectrometer in a mixture of methanol and deuterated methanol operating at 62.895 MHz applying a broadband proton decoupling technique.

Elemental analysis is performed using various apparatuses (ELEMENTAR Vario EL C/H/N-Determinator; LECO TC-436-DR N/O Determinator) and by atom emission spectrometry (ISA JOBIN YVON JY70 Plus). Thermal properties are studied by differential scanning calorimetry and thermogravimetric analysis. These are carried out simultaneously in air between 25 and 1000 °C at a heating rate of 10 K·min<sup>-1</sup> in alumina crucibles using a Netzsch STA Jupiter 449C connected to a quadrupole mass spectrometer (GAM 200, In Process Instruments) for the detection of gaseous species. For the elemental analysis of the particles, the dispersions are centrifuged at 1880·g for 90 minutes, the supernatant is replaced by pure methanol, the sediment is redispersed, the dispersion is centrifuged again and the supernatant decanted. The sediment is dried and ground in a mortar.

## 5.3 Results and discussion

### 5.3.1 Three stages of particle formation

In order to understand the mechanism of film deposition on a substrate, thorough knowledge of the reactions in the precursor solution during the procedure is indispensable.

The processes in the solution occur in three distinct stages. The initial stage appears after mixing the solution, but before heating, the intermediate stage immediately after heating up the solution, and the final stage represents the long-time behaviour. Qualitatively, the behaviour is strongly dependent on the PVP concentration. Five regimes with distinct levels of the volumetric polymer content  $\phi$  are analysed: zero polymer content, low polymer content ( $\phi \approx 0.05$ ), medium or intermediate polymer content ( $\phi \approx 0.10$ ), high polymer content ( $\phi \approx 0.15$ ), and very high polymer content ( $\phi \approx 0.20$  and more). [128] Even at PVP concentrations denominated “low”, the

polymer chains are interpenetrating. [101] The polymer solutions are not fully diluted, but in the semi-dilute regime and contain a network of PVP molecules. During the three process stages, and at the various PVP concentrations, different chemical and physical processes take place in solution.

The time evolution of the particle size in the precursor solutions is measured in situ with dynamic light scattering (DLS) at 60 °C (Figure 5.1). The behaviours during the intermediate and final stages are significantly different. During the intermediate stage the particle size remains approximately constant. In the final stage, a linear increase of the particle diameter is observed. Between the two stages, there is a very short transition period with a substantial decrease of the measured particle size (except at high PVP concentrations, where the particle size stays small over the whole intermediate stage). This intermittent stage lasts for 1 to 3 h, and its duration is lower at higher polymer concentrations.

The observations with DLS suggest a hypothesis that different types of particles may form. After the solution is heated up, particles of one kind are present; they dissolve while a different type of particles forms. The characteristic size of the first kind of particles is between 20 and 50 nm. In the end of the intermediate stage of the process, these particles dissolve rapidly, within about half an hour. The growth of the second kind of particles, during the final stage, is linear and faster at higher PVP concentrations. At low PVP concentrations, the growth is barely noticeable; at the highest PVP concentration tested, the growth rate is almost 10 nm·h<sup>-1</sup>.

At very high PVP concentrations, with light scattering no particle formation is detected. This finding is evidence that no mineralization takes place at very high PVP content.

Besides the described phenomena, in DLS one can always find a strong signal which seemingly arises from smaller particles with sizes below 10 nm, with a time-dependent behaviour similar to the time evolution of the size of the larger particles. This signal is typical of scattering at the polymer molecules, with some systematic error originating from the evolution of the size of the larger particles, together with the impossibility to completely separate the contributions of objects of two different sizes to the DLS signal. However, these complications aside, it is clearly visible from Figure 5.1 that the particle size evolution is strongly dependent on the PVP concentration.

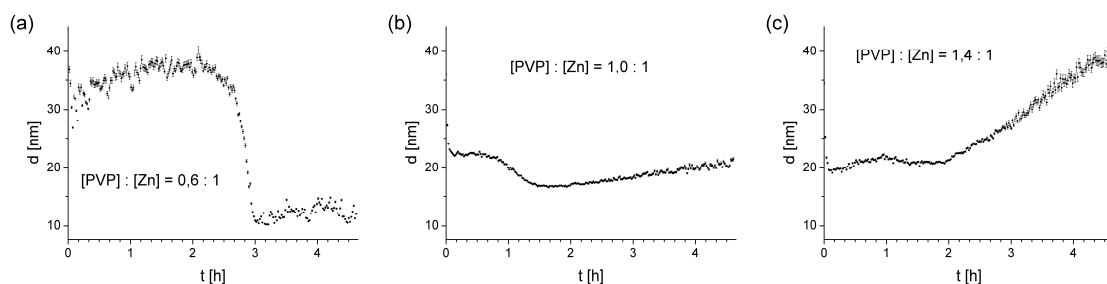


Figure 5.1: Time evolution of the particle size in deposition solutions with various polymer contents at 60 °C as measured by dynamic light scattering. Note how after a certain period of time the initial particles either shrink or stay constant in size, until the behaviours are reversed and the particles start to grow linearly. It will be shown that different particles dominate those stages.

### 5.3.2 Initial stage at room temperature

Evidence for the hypothesis of the different kinds of particles is found using transmission electron microscopy (TEM). As a control experiment, samples from unheated reaction solutions are investigated. Such solutions do not contain any particles if  $[PVP] : [Zn^{2+}]$  is 0.8 or higher (Figure 5.2). At ambient conditions, PVP prevents particle formation in the solutions; particles are formed only at low or zero polymer content.

If the solution is free of polymer, the particles formed at ambient conditions are crystalline and exhibit a rod-like morphology (Figure 5.3). XRD diffractograms of these particles show the characteristic diffraction pattern (Figure 5.4) of ZnO (zincite) plus a weak signal of  $Zn(OH)_2$  (wülfigite), which is due to surface hydroxylation of the particles. The morphology of the nanocrystals depends on the tetraethylammonium cation. If NaOH was used instead, approximately spherical nanocrystals of ZnO were found in solution. When the polymer-free solutions are heated to 60 °C, the nanocrystals dissolve within several hours. Otherwise no significant change of their composition and morphology was detected, except that a proportion of the “rods” disintegrated into shorter particles.

At low PVP content, amorphous particles are detected identical to the ones found during the intermediate stage and described in the following chapter.

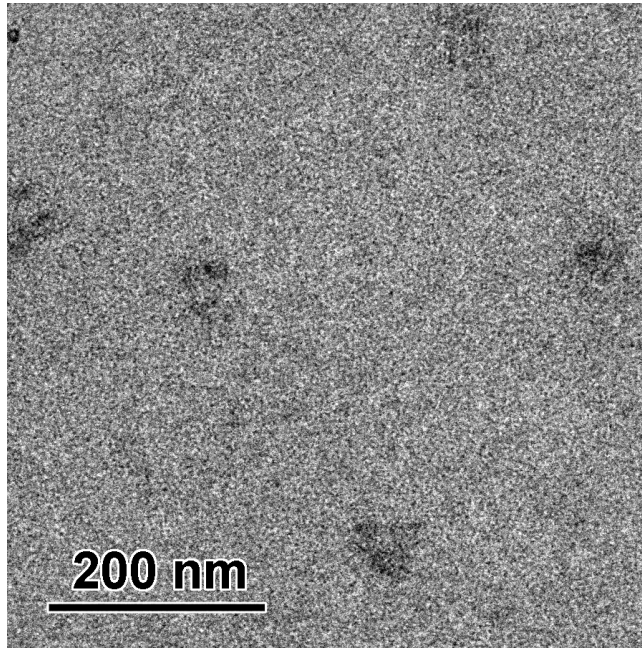


Figure 5.2: TEM micrograph: Sample from a solution with  $[PVP] : [Zn^{2+}] = 1 : 1$  before heating. As the dark blots show only a weak contrast and no indication of solidity or crystallinity, it is concluded that they are agglutinated polymers. There is no evidence of formation of amorphous or crystalline zinc containing particles.

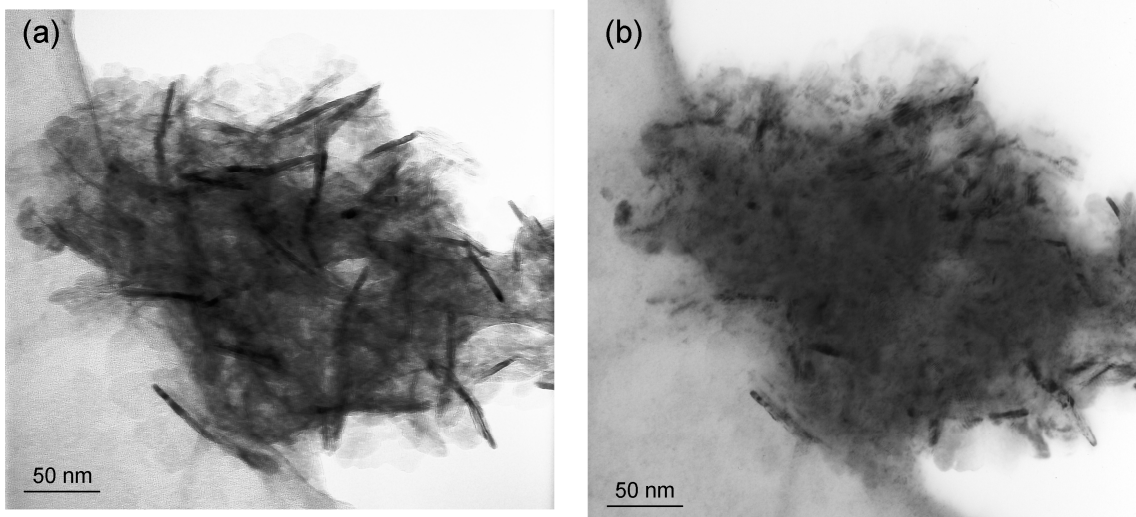


Figure 5.3: TEM images of crystalline ZnO particles prepared from a methanolic  $Zn^{2+}/TEAOH$  solution, without PVP and without heating. (a) bright field TEM image, (b) inverted dark field TEM image (i. e. negative). Note that in the dark field image domains are visible. This strongly indicates polycrystalline spicular particles.

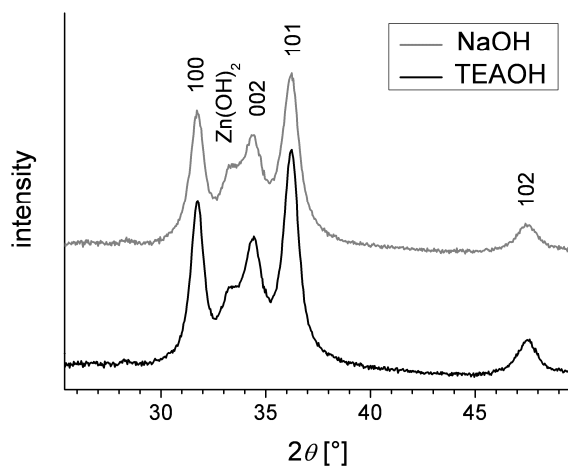


Figure 5.4: X-ray diffractogram of the particles prepared from methanolic  $\text{Zn}^{2+}$  solutions (no PVP or heating), with the addition of NaOH and TEAOH respectively. The individual graphs are shifted along the y-axis. The data was corrected by subtraction of the background intensity caused by the substrate. Typical zincite peaks are indexed.

### 5.3.3 Intermediate stage after heating-up to 60 °C

After the solution is heated up to 60 °C, i. e. at the beginning of the intermediate stage, ca. 30 nm long spicular (i. e. needle-like) [129] particles are observed (Figure 5.5) in all solutions except those without or with a very high polymer content. At intermediate and high PVP concentrations, spicular particles are formed at 60 °C; at low PVP concentrations they appear already at room temperature. In contrast to the PVP-free case, these spicular particles are observed under solution conditions with both TEAOH and NaOH.

Crystallinity was detected neither by X-ray diffraction (Figure 5.6) nor by TEM. Hence the spicular particles in PVP-containing solutions are amorphous.

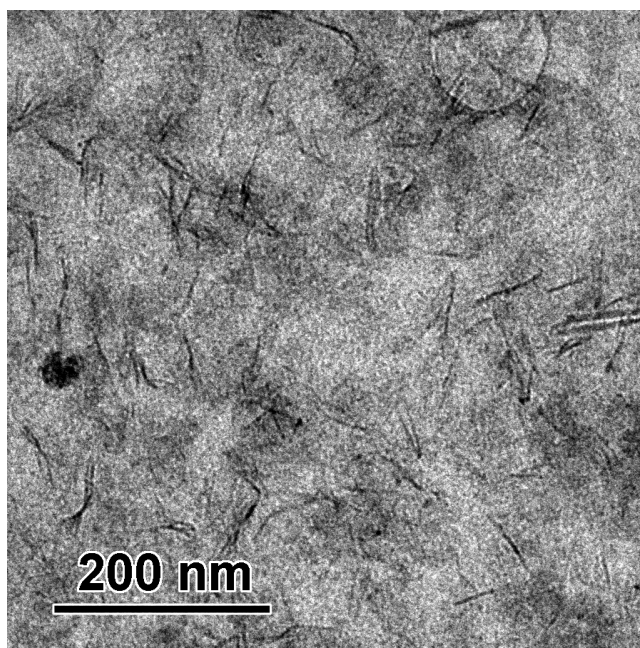


Figure 5.5: TEM micrograph: Spicular particles in a solution with  $[\text{PVP}] : [\text{Zn}^{2+}] = 1 : 1$  are present after 5 min reaction at  $60\text{ }^{\circ}\text{C}$ .

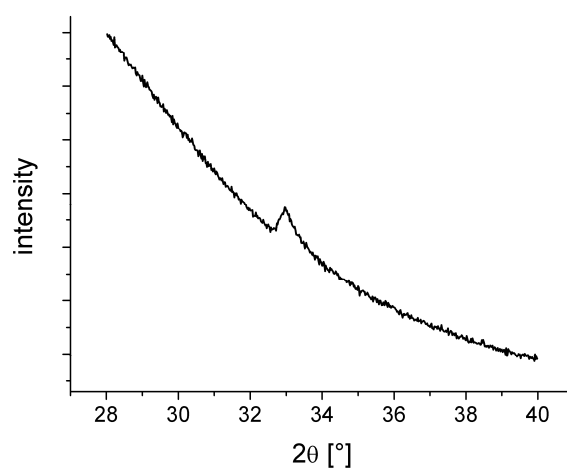


Figure 5.6: X-ray diffractogram of the spicular intermediate particles prepared from a solution with  $[\text{PVP}] : [\text{Zn}^{2+}] = 1 : 1$  after 5 min reaction at  $60\text{ }^{\circ}\text{C}$ . The peak at about  $33.1^{\circ}$  is due to the Si substrate on which the sample was prepared. The diffractogram does not indicate any crystallinity (compare with Figure 5.4).

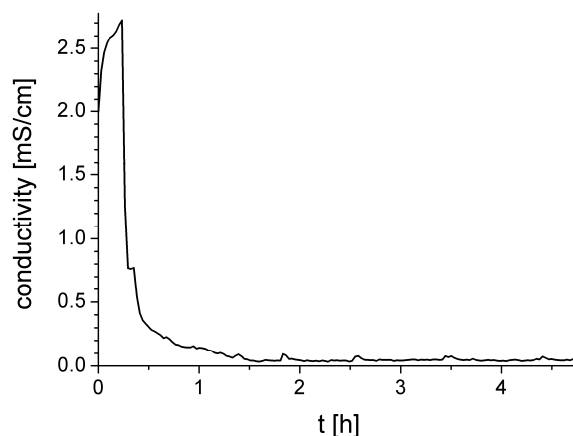


Figure 5.7: Time evolution of the electric conductivity of a deposition solution with a [PVP] : [Zn<sup>2+</sup>] ratio of 1,0 : 1 treated at 60 °C. Note the rapid decline of the conductivity indicating particle formation.

The formation of the amorphous spicular particles is rapid. The conductivity of the solution stays high for only a few minutes and decreases rapidly thereafter (Figure 5.7). This indicates consumption of the ions by fast particle formation.

#### 5.3.4 Final stage

Both at low and high PVP concentrations, the initial spicular particles gradually transform into polycrystalline aggregates, which consist of approximately spherical ZnO crystallites with diameters of only few nanometers according to TEM micrographs (Figure 5.8a). At low PVP concentrations, the aggregates have a fractal shape (Figure 5.8b), whereas at intermediate and high PVP concentrations, they are more compact and approximately spherical (Figures 5.8c and 5.8d).

The polycrystalline aggregates grow gradually. The growth rate increases with increasing PVP concentration (Figure 5.1). In some samples, mostly at low PVP content, ZnO nanoparticles can be observed in solution before the aggregates are formed. At higher PVP concentrations, the aggregation starts immediately after heating up. In most of these samples single nanocrystals could not be detected.



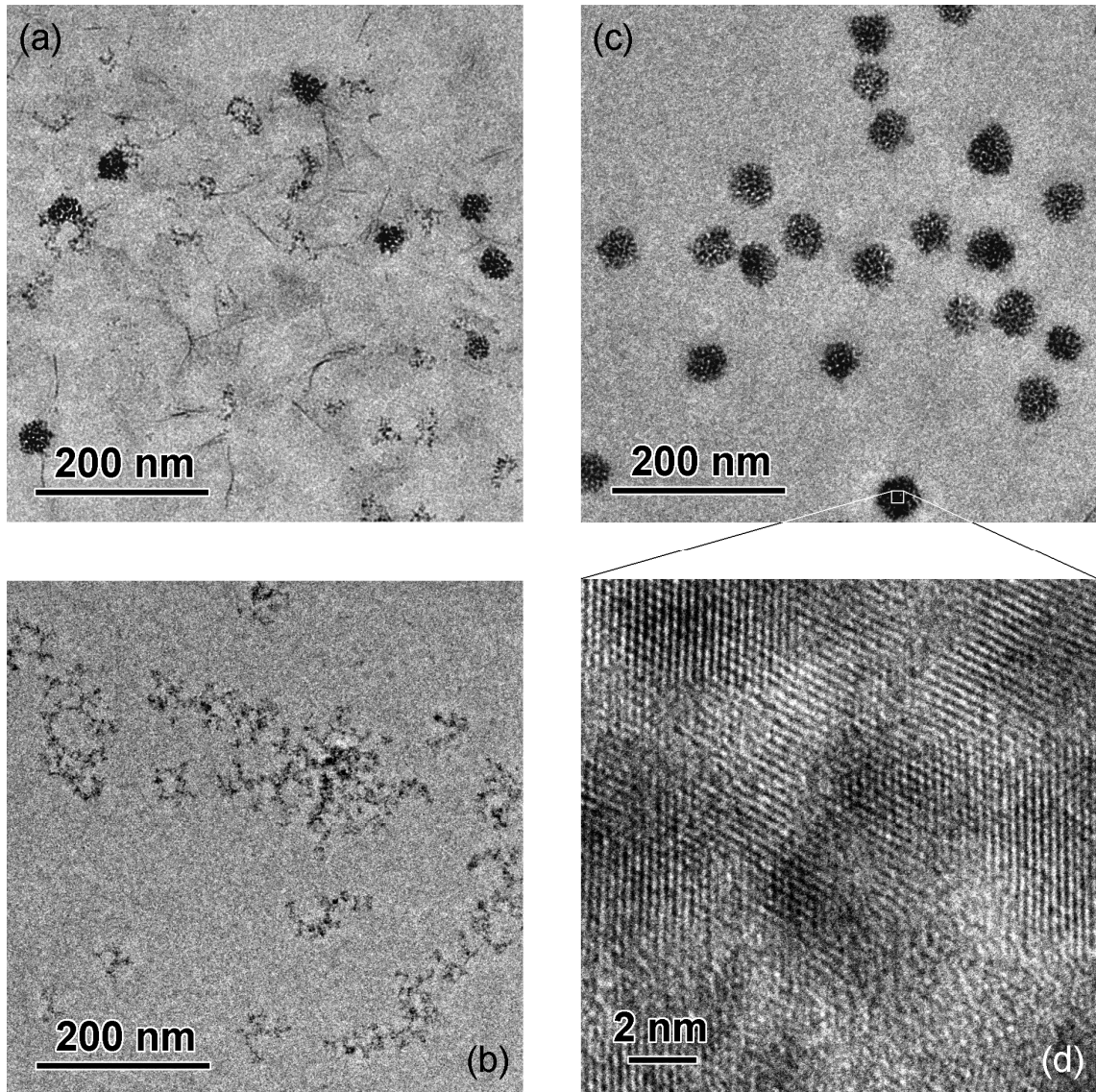


Figure 5.8: TEM micrographs:

(a) Spicular particles and compact aggregates of ZnO coexist in a methanolic solution with  $\text{Zn}^{2+}$ , TEAOH, and an intermediate PVP concentration after 1.5 h at 60 °C.

(b) Fractal aggregates of nanosized ZnO are evident in a methanolic solution with  $\text{Zn}^{2+}$ , TEAOH, and a low PVP concentration after 3.5 h at 60 °C.

(c) Compact aggregates of nanosized ZnO particles are evident in a methanolic solution with  $\text{Zn}^{2+}$ , TEAOH, and a high PVP concentration after 3.5 h at 60 °C. Images from solutions with intermediate PVP concentrations look very similar, except for the somewhat lower diameter of the aggregates.

(d) High resolution TEM image of an aggregated particle from the same sample from which the image above was taken. The angular distribution of the lattice fringes demonstrates the polycrystallinity of the particles.

### 5.3.5 Composition of the particles in solution

The composition of three samples, each containing one of the three typical species of particles, are investigated by thermal and elemental analysis.

*Initial stage:* Rod-like particles prepared without PVP at room temperature are analysed. Around 150 to 200 °C, alleviatedly continuing to about 400 °C, about 25 % mass is lost. Mass spectrometry indicates expulsion of H<sub>2</sub>O, CO, CO<sub>2</sub>, and hydrocarbon fragments with  $M_r = 17$ . This indicates decomposition of methanol or residual acetate or carbonate moieties. At about 700 to 800 °C, a weakly endothermic process occurs concurrently with a slight increase in mass, apparently because of an oxidation.

*Intermediate stage:* The spicular particles prepared at low PVP concentrations in a reaction of 20 min at 60 °C experience a slight mass loss between 150 and 200 °C (about 5 %); H<sub>2</sub>O and hydrocarbon fragments with  $M_r = 17$  are released. A more significant mass loss occurs around 400 to 500 °C (about 30 %), concurrently with an endothermic reaction because of the decomposition and expulsion of fragmented PVP molecules. In particular, signals of CO, H<sub>2</sub>O, hydrocarbon fragments with  $M_r = 17$  and  $M_r = 30$ , and a very strong signal of CO<sub>2</sub> were detected.

*Final stage:* The compact aggregates prepared at high PVP concentrations in a reaction of 24 h at 60 °C loose about 40 % of their original mass at around 300 to 500 °C. This mass loss is accompanied by endothermic reactions. Mass spectroscopy indicates PVP fragmentation. H<sub>2</sub>O, hydrocarbon fragments with  $M_r = 17$  and  $M_r = 30$ , and plenty of CO<sub>2</sub> are released.

Pure PVP decomposes in strongly endothermic reactions in the same temperature range. In mass spectroscopy, CO, H<sub>2</sub>O, hydrocarbon fragments with  $M_r = 30$ , and CO<sub>2</sub> were detected.

The rod-like and spicular particles (initial and intermediate stage, respectively) contain residual acetate or methanol. The particles formed in PVP containing solutions (intermediate and final stage) contain a large amount of PVP. It is not clear whether all the PVP is incorporated in the particles, or whether it is a remnant from the solution sticking to the particles or aggregates because of imperfect purification of the particles.

The results of the elemental analysis of the three types of samples are outlined in Table 5.1. For comparison, the elemental compositions of hypothetical particles consisting of arbitrary amounts of ZnO, Zn(OH)<sub>2</sub>, PVP, methanol, and water were calculated. Congruently with the results from the thermal analyses, the comparison of the experimental and the calculated values suggests that about two thirds of the mass of the particles taken from solutions containing PVP are zinc oxide and zinc hydroxide, about one third is PVP, and additionally there is some remnant solvent. The main constituent of the amorphous spicular particles may be Zn(OH)<sub>2</sub> and/or

ZnO. About three fourths of the mass of the particles taken from the polymer-free solution are ZnO, and about one fourth is solvent.

	rod-like particles, zero PVP, no heating	spicular particles, [PVP] : [Zn <sup>2+</sup> ] = 0,4 : 1, 20 min at 60 °C	compact aggregates, [PVP] : [Zn <sup>2+</sup> ] = 1,4 : 1, 24 h at 60 °C
Zn	51 %	44 %	41 %
O	34 %	31 %	30 %
N	1 %	3 %	4 %
C	9 %	18 %	20 %
H	3 %	4 %	4 %

Table 5.1: Results of the elemental analysis of three uncalcined samples (percent by weight) determined by C/H/N composition analysis and atom emission spectrometry. Note the significant content of carbon in these samples.

### 5.3.6 Interactions of PVP with ions, particles and aggregates

The interactions between PVP and zinc ions as well as the amorphous interstage are investigated in order to find clues to the effect of PVP during the initial stage of the deposition process. In electrophoresis, no interaction between PVP and zinc ions could be observed. <sup>13</sup>C NMR spectroscopy suggests that there is a weak interaction between PVP and zinc ions as indicated by chemical shift changes for the carbonyl carbon in both PVP and monomeric vinylpyrrolidone upon addition of Zn<sup>2+</sup>. However, no significant line broadening of the signals or any change in the chemical shift from the PVP polymer are detected in the presence of the amorphous spicular particles (Figure 5.9). [130] Furthermore, the influence of PVP on the ZnO grain size is negligible (Figure 5.10).

During the final stage of the process, PVP controls the growth of the polycrystalline ZnO aggregates. In order to elucidate the effect of PVP during that stage, the evolution of the particle size is followed for more than one day (Figure 5.11). A linear increase of the particle diameter is found. The growth rate is higher at higher PVP concentrations. A linear increase in diameter implies that the particle growth is much faster than growth by Ostwald ripening, which, in the diffusion limited case, would mean a linear increase in volume. The unexpected, compact morphology of the aggregates is another indication that PVP essentially determines the aggregation process.

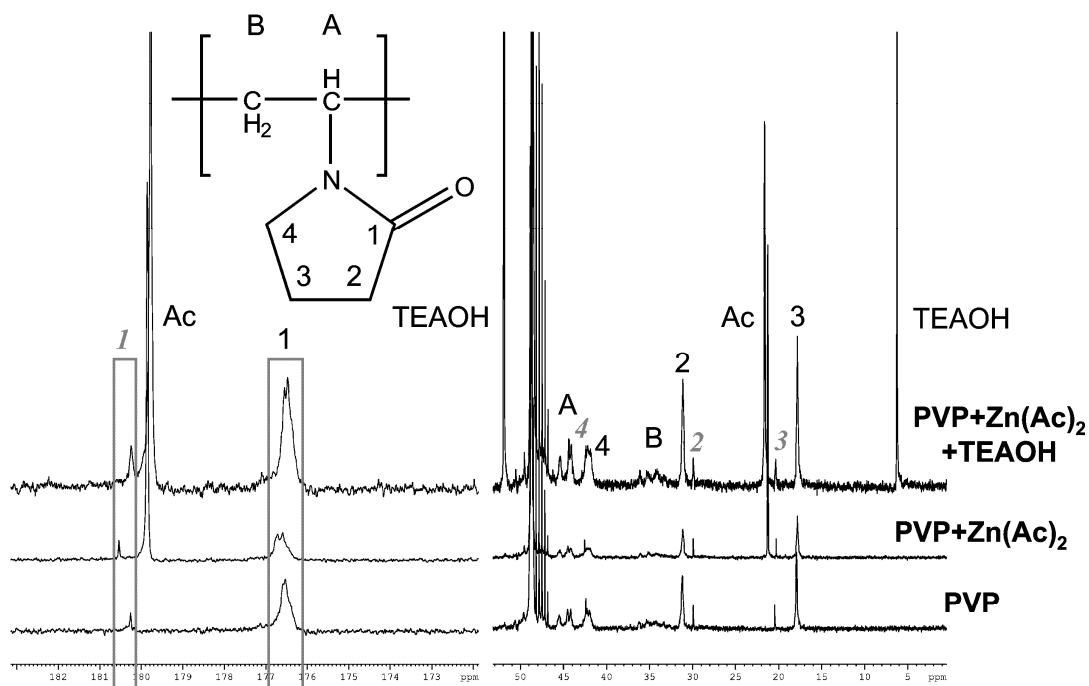


Figure 5.9:  $^{13}\text{C}$  NMR spectra recorded of three solutions containing only PVP, PVP plus zinc acetate, and PVP plus zinc acetate plus TEAOH. The carbon atoms in the PVP monomer were assigned numbers or letters, and the corresponding numbers or letters in the spectra indicate which peak can be attributed to which carbon atom. Grey italic numbers indicate signals from free monomeric vinylpyrrolidone. Note the small but significant changes in the chemical shift for the carbonyl carbon on addition of  $\text{Zn}^{2+}$  (in the middle spectrum).

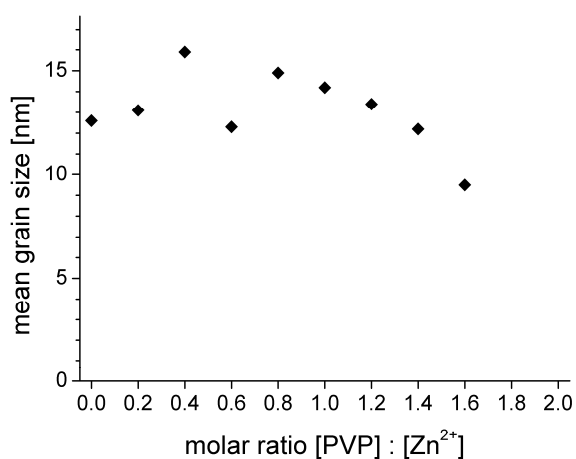


Figure 5.10: Average grain size in the ZnO thin films depends only weakly on the polymer concentration. The grain sizes were determined from XRD data using Scherrer analysis.

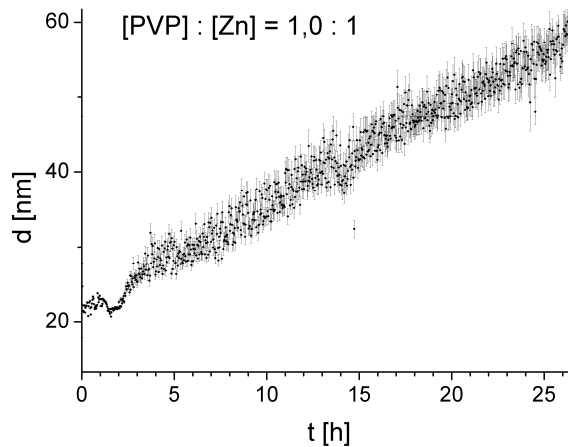


Figure 5.11: Time evolution of the size of zinc oxide particles/aggregates in a basic methanol deposition solution with  $[PVP] : [Zn^{2+}] = 1,0 : 1$  at 60 °C shows a linear increase.

The fractal aggregates observed at low PVP concentrations are well in accordance with the structures observed in colloidal model systems. [131] In contrast, the fast particle growth at high PVP concentrations and the high density of the compact aggregates cannot be explained merely by one of the prevalent models of crystal growth or aggregation such as reaction-limited aggregation [132,133] or diffusion-limited aggregation [134] without consideration of the effects of the dissolved polymers. Non-adsorbing polymers cause attractive depletion forces between particles because of entropic effects. [135] Thus the formation of aggregates of comparable compactness in dispersions containing relatively high polymer concentrations has been asserted by theoretical studies, [136,137] by simulations, [138] and by experimental investigations of model systems. [139,140]

The zeta potential of the particles in solution might give further clues whether electrostatic interaction is involved in aggregation and film formation. In solutions containing zinc acetate, PVP, and TEAOH in methanol, the electrophoretic mobility of the particles, which is directly proportional to their zeta potential, was measured as a function of time at 60 °C (Figure 5.12). The measured values are all close to zero and scatter strongly. It seems improbable that the particles have an appreciable surface charge which is screened by a coating of PVP. As apparently strong forces like electrostatic interaction can be ruled out for the present system (see below), aggregation is governed by weak interactions which imply the reversibility of attachment and permit rearrangement of the clusters towards a compact spherical shape. [138,141]

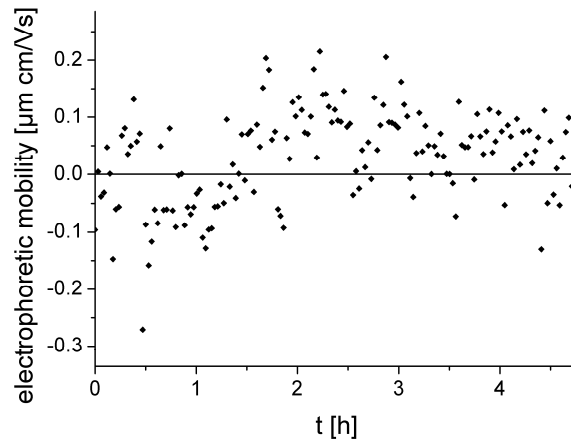


Figure 5.12: Time evolution of the electrophoretic mobility in a basic methanol deposition solution with  $[PVP] : [Zn^{2+}] = 1,0 : 1$  at  $60\text{ }^{\circ}\text{C}$ . The mobility is close to zero and scatters strongly, and a weak trend indicates an initial negative value that turns positive, on the average, after a few hours.

The hypothesis that the polymer adsorbs to ZnO crystallites and thus prevents their growth [9] is not realistic in the case of PVP. However, the PVP does influence the particle formation. The PVP concentration determines whether the spicular particles form at room or elevated temperatures, whether they are crystalline, and how soon they dissolve. When finally spherical ZnO nanocrystals are formed, PVP guides their aggregation on the substrate and in solution, probably via depletion forces (as discussed above). High polymer concentrations prevent the formation of any particles. This indicates that the polymer does not only tune the particle aggregation kinetics, but also the molecular chemical reaction kinetics or, maybe even, equilibrium.

### 5.3.7 Influence of the substrate on the film deposition

ZnO film deposition is possible both on strongly positively charged substrates such as SAMs with a protonated amino group, and on strongly negatively charged substrates. [127,142,143] The films deposited on SAMs with sulfonic acid groups are somewhat smoother than the ones deposited on SAMs with amino groups, and their texture is slightly more pronounced, but altogether the differences are small. The deposition of rough films was even achieved on lead zirconate titanate (PZT), a material with a high dielectricity. Deposition is not possible on weakly charged or neutral surfaces such as bare silicon, [127] glass, or untreated plastics. It is concluded that not the sign of the charge is crucial, but its magnitude. This indicates that the polarity of the ZnO

crystallites plays a significant role in attachment and structure formation.

The low surface charge of the ZnO particles (see the discussion of the electrophoretic mobility above), the high ion strength, and the possibility of film formation both on negatively and on positively charged surfaces rule out simple electrostatic attraction as the dominant mechanism for attachment to the substrate. Instead, the observed results suggest a mechanism of oriented aggregation: [144] Zinc oxide crystallites are polar because of the specific crystal structure of zincite. [145] This polarity induces a preferred orientation of the crystallites, towards the electrical double layer close to the SAM surface and permits oriented attachment of the crystallites. A texture emerges.

### 5.3.8 Influence of the polymer on the film deposition

The film thickness depends strongly on the ratio  $[\text{PVP}] : [\text{Zn}^{2+}]$  in the solution (Figure 4.3b); new measurements show that the same is true for the roughness. The maximum thickness and minimum roughness occur at a ratio of around  $[\text{PVP}] : [\text{Zn}^{2+}] \approx 1$ .

At zero and at very low PVP concentration, large disordered clusters precipitate from solution onto the substrates and can widely be removed by ultrasonification. At low and intermediate PVP concentrations, a smooth and contiguous ZnO film is deposited, whose thickness increases with increasing PVP concentration. At high PVP concentrations, the thickness reaches a plateau, and smoothness and texture are gradually lost again when the PVP content is increased further. At very high PVP concentrations hardly any particles are formed and no film is deposited.

X-ray diffraction data reveal similar trends. In all samples, which exhibit appreciable deposition, the three typical ZnO peaks at scattering angles  $2\theta$  of about  $31.9^\circ$ ,  $34.6^\circ$ , and  $36.4^\circ$  are present (Figure 5.13). At low and at high PVP concentrations the relative intensities of the peaks correspond to the pattern obtained from a powder. At intermediate PVP contents, however, the predominance of the (002) peak is evidence of a pronounced texture.

The competition between aggregation in solution and film formation on the substrate accounts for this behaviour. Non-interacting polymers in solution destabilize dispersions and induce aggregation. [146] Accordingly, the film grows faster at higher polymer concentrations. Simultaneously, the growth of the aggregates in solution is enhanced. The film and aggregate growth compete, and the aggregation is ultimately favoured, because of the larger surface area of the aggregates, as soon as a sufficient number of aggregates has formed. This occurs more rapidly

at higher PVP concentrations, so at high polymer concentrations the favourable timeframe for film formation becomes too short for a further increase in film thickness and smoothness. The fast aggregation at higher PVP concentrations also leaves no time for internal rearrangement of the growing structures which would permit the development of a texture. At low PVP concentrations, on the other hand, the roughness of the deposits is also high, and their internal alignment low, because of the described precipitation of clusters. So there is a “sweet spot” of an intermediate concentration of PVP being optimal for the formation of thick, smooth and well-ordered ZnO nanocrystalline films.

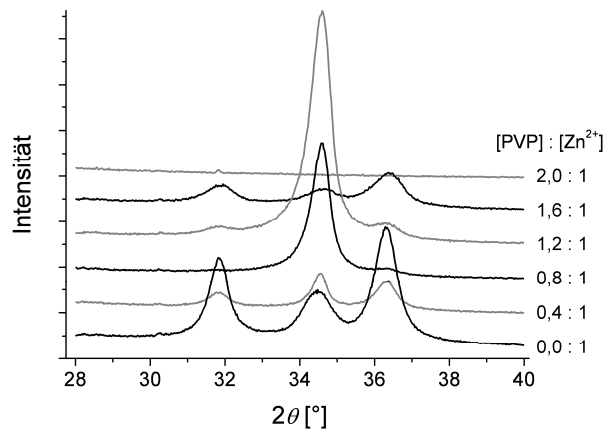


Figure 5.13: X-ray diffractograms of ZnO films deposited from basic methanol solutions with varied  $[PVP] : [Zn^{2+}]$  ratios. The single graphs are shifted along the y-axis.

One might suggest that the polymer network in solution controls the deposition by slowing down the diffusion of the nanoparticles. Evidence for such diffusion control has manifested itself neither in the present experiments nor in current theoretical models. [147,148]

### 5.3.9 Deposition kinetics

Quartz Crystal Microbalance (QCM) experiments show an almost instant start of the deposition after the deposition solutions was heated up to 60 °C (Figure 5.14a). The rate of mass increase is high in the beginning and decreases gradually to zero. On the bare SAM the deposition continues for about 30 minutes with only small amounts deposited. During subsequent deposition cycles the rate of mass increase is much higher, and the films continue to grow for almost 3 h (Figure 5.14b). The film formation is more significant on an already existing



ZnO film than on the bare substrate, which is another indication that film formation happens by oriented attachment. This is in line with the observation that during the first two or three deposition cycles islands are formed rather than continuous films. The mass of the film decreases slightly after a few hours; however, this may be caused by solvent evaporation since the sample chamber could not be closed hermetically.

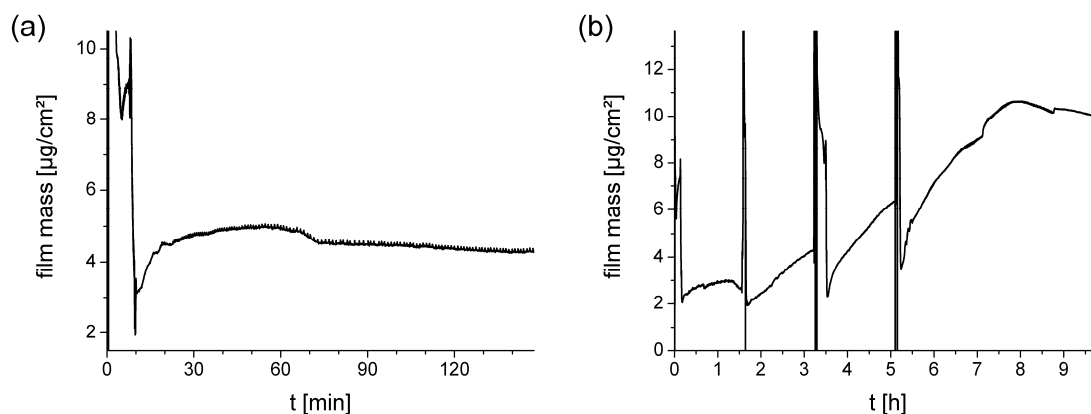


Figure 5.14: Graphs of mass uptake experiments with a QCM show ZnO film growth on a sulfonate-SAM during (a) a single deposition cycle and (b) four deposition cycles respectively. The vigorous amplitudes, before and between the actual deposition cycles, are due to temperature differences and agitation while the reaction chamber is assembled and filled.

The QCM results suggest that the deposition solution could be used more efficiently, albeit with a slightly slower average deposition rate, if an initial deposition cycle of 0.5 h and subsequent deposition cycles of 3 h are applied instead of deposition cycles of 1.5 h. Testing the suggested schedule experimentally, a 46 % thicker film could be deposited from the same amount of deposition solution, admittedly with the drawback of an 83 % longer total deposition time.

### 5.3.10 Influence of the molecular weight of the polymer

TEM investigations demonstrate that in solutions containing PVP with a molecular weight of 40 000 g/mol (K25) the process passes through the same stages as in solutions containing PVP with 10 000 g/mol (K15 or PVP10) if the volume fraction of polymer is similar. This observation suggests that for proper control of the aggregation and deposition dynamics of zinc oxide nanoparticles, the presence of a polymer network of a certain density is crucial.

When films are deposited using the higher molecular weight PVP polymer, a slower deposition rate is found. Films with the best properties (thickness and roughness) are obtained at a slightly higher volume fraction of PVP in the deposition solution than with K15 ( $\phi \approx 0.15$  instead of  $\phi \approx 0.1$ ). The decrease of film thickness with rising polymer concentration is less abrupt with the K25 polymer, and at  $\phi \approx 0.2$  film deposition is still possible. One could speculate whether the discrepancy relates to the decreased entropy of mixing associated with K25. Unaffected by this small difference, one may conclude that the decisive factor is not the number of polymer molecules per volume or the length of the polymer chains, but the concentration of monomer units or, equivalently, the volume fraction of polymer.

## 5.4 Conclusion

The precursor solutions contain zinc acetate which is partly dissociated into zinc and acetate ions. The zinc ions interact with the polymers, so a certain proportion among them may be considered as solvated by the PVP. While solvated by the PVP, the zinc ions are not available for further reactions any more; this is the reason why no particle formation is observed if the PVP concentration is too high.

When a polymer-free precursor solution is heated, zinc oxide nanocrystals are formed. When PVP is present, however, this route is barred and the zinc ions participate in the formation of amorphous spicular particles. The formation of these particles is mediated by the PVP and happens with a very high rate constant. On the other hand, PVP also enhances the dissolution of the spicular particles; so higher PVP concentrations destabilize the particles. The dissolution of the spicular particles happens, however, with a much slower rate constant than their formation. Therefore the particles are stable for some time depending upon the PVP concentration. When the spicular particles dissolve again, free zinc ions are available for crystallization. Consuming these zinc ions, zinc oxide nanocrystals form gradually. PVP tunes the interaction between the nanocrystals, via depletion forces, and promotes film formation on the substrate and aggregation in solution.

Aggregation in solution and film deposition happen simultaneously and compete with each other. Initially, film formation is favoured because of a lower energy barrier, but at a certain critical number of aggregates, aggregation in solution will be favoured because of the larger total surface of the aggregates, and film formation on the substrate will come to a halt.

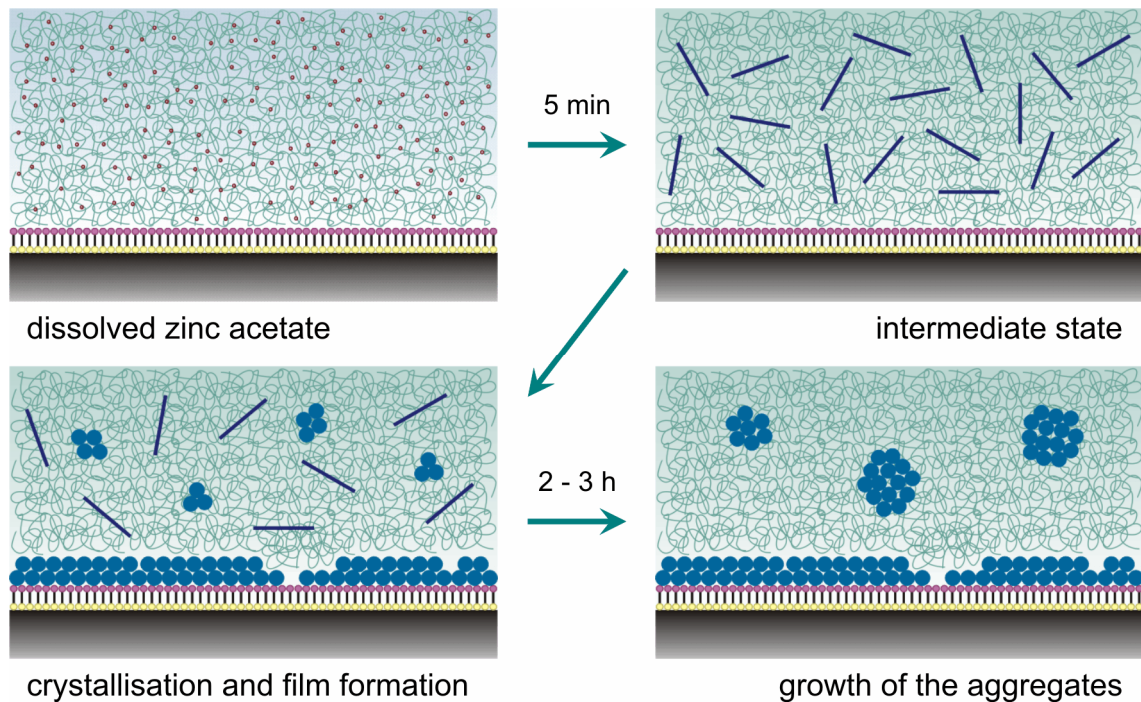


Figure 5.15: Schematic pictorial view of the processes active during the deposition of a smooth thick film of nanosized ZnO particles on a charged SAM. This picture represents the “sweet spot” with an intermediate concentration ratio  $[PVP] : [Zn^{2+}]$  in the basic methanol solution. The grey block is the silicon carrier, the palisades symbolize the SAM, the green clews are the polymers, the red dots are  $Zn^{2+}$  ions, the dark purple lines are the amorphous spicular particles, and the blue circles are ZnO crystallites.

Apart from preventing immediate crystallization, PVP has distinct effects on three steps of the process: Firstly, it is involved in the formation of the amorphous spicular particles, and it is also included into them. Secondly, it dissolves those particles, so the onset of the dissolution of the spicular particles occurs sooner at higher polymer concentrations. Thirdly, the polymers trigger and boost the growth of the polycrystalline aggregates since they promote aggregation via depletion forces. Their influence explains the surprisingly fast particle growth and the unexpectedly high density of the aggregates at high polymer concentrations.

PVP Concentration				
zero ( $\phi = 0$ )	low ( $\phi \approx 0.05$ )	medium ( $\phi \approx 0.10$ )	high ( $\phi \approx 0.15$ )	very high ( $\phi \approx 0.20$ )
Initial Deposition Solution (before heating)				
turbid, crystalline rod-like ZnO particles	slightly turbid, amorphous spicular particles	clear, no particles		
↓	↓	↓	↓	↓
Intermediate State in Solution (when heated to 60 °C)				
ZnO nanoparticles	amorphous spicular particles			no particles
↓	↓	↓	↓	↓
Final State in Solution (after several hours)				
ZnO nanoparticles	fractal ZnO aggregates	slowly growing compact ZnO aggregates	fast growing compact ZnO aggregates	no particles
Deposition on the Substrate				
disordered clusters of ZnO crystallites	rough thin ZnO film, slight texture	smooth thick ZnO film, strong texture	rough thick ZnO film, slight/no texture	no film

Table 2: Overview over the observed processes in solutions with various polymer contents and at different times. Note that there is a “sweet spot” in the PVP concentration for which compact aggregates are formed in the solution and smooth thick films are deposited.

The amorphous spicular particles represent an intermediate stage of mineralization, which has not been reported for chemical bath deposition previously. The existence of amorphous intermediate stages is, however, not unusual for directional growth processes. Instances are found in biomineralization. [144] On the way towards crystallization, the detour via the amorphous interstage is crucial for the formation of ordered structures such as textured films on the substrates. By taking this detour it is, on the one hand, possible to avoid rapid crystallization leading to unstructured clusters such as in polymer-free solutions. On the other hand, a slower rate of crystallization can be set via the PVP concentration, and the system can be designed so that the deposition process can be triggered by a small increase in temperature. The amorphous particles represent, so to speak, a reservoir, from which zinc ions can be released at an adjustable rate.

## 5.5 Acknowledgements

The authors wish to thank Dr. Udo Welzel, Maritta Dudek and Gerd Maier for recording the XRD diffractograms, Sabine Kühnemann for taking the SEM images, Peter Gerstel for the synthesis of the silanes, for doing the NMR measurements and for general support in the Chemistry laboratory, Gerhard Kaiser for chemical analysis, Peter Kopold for supervision during some of the TEM investigations, and Dr. Paul Bellina and Dr. Peter van Aken for discussions about TEM.



**6. Zinc oxide microcapsules obtained via a bio-inspired approach**

**Abstract**

Hollow zinc oxide microcapsules have been synthesized by a sacrificial template route involving the chemical bath deposition of nanostructured zinc oxide thin films on sulfonate-modified polystyrene microspheres and subsequent removal of the polymer core by dissolution in a solvent or by thermolysis. Scanning electron micrographs show that uniform coating of the templates is achieved when ZnO is deposited from a solution containing zinc acetate, the polymer polyvinylpyrrolidone, and a base in methanol, and that the ZnO shells remain intact after removal of the cores. A focused ion beam is used to cut slices from the spheres and demonstrate their inner morphology and hollowness. X-ray diffraction yields evidence that the shells consist of nanocrystalline ZnO with the zincite structure.



## 6.1 Introduction

Zinc oxide is a substance with advantageous properties promising manifold applications. [82] Hollow spheres with diameters in the micrometer or nanometer range are of particular interest due to their low overall density, high surface area, material properties distinct from bulk materials, [149] and their possible use for encapsulation. [150] Further applications of high surface area ZnO are gas sensors [151] and catalysts. [152]

Hollow ZnO structures have been fabricated by oxidation of vapour-deposited zinc, [153,154] laser-assisted growth on the surface of ethanol droplets as templates, [155] chemical vapour deposition on carbon nanotubes [156] and an autoclave and pyrolysis process. [157] All these processes, by which shape, size and quality of the produced shells remain more or less accidental, require high energies or complex set-ups.

Self-assembly of ZnO nanoparticles on interfaces in a Pickering emulsion has been achieved. [158] Although this process is easy to control, it requires the previous synthesis of ZnO nanoparticles by a separate process. As minimization of the interfacial energy is the driving force for assembly in this case, the forces between the nanoparticles in the shells are only weak, and therefore the resulting hollow spheres have a low quality and low stability. Considering the mentioned methods, there remains a need to find a process which combines the possibility to control the geometry of the hollow spheres with on-site mineralization of ZnO for better quality and stability of the wall.

Recently, a sacrificial template route for the fabrication of ZnO hollow spheres has been employed using  $Zn_5(CO_3)_2(OH)_6$  beads [159,160] or microspheres of  $Zn^{2+}$  exchanged polystyrene (PS) resin [161] as templates. This method consists of two steps: First a coating of the desired shell material is formed on a template of the desired shape, and subsequently the template is dissolved in a solvent or decomposed by heat. The difficulty of synthesizing monodisperse microspheres of the respective template materials with arbitrary diameters limits, however, the universal applicability of these approaches.

The thermohydrolysis of metal salts, known as chemical bath deposition (CBD), is a rather new method for the deposition of oxidic thin films. [12] Compared to other methods of film deposition, it is simple and inexpensive. [84] Another main advantage is the possibility to coat substrates of irregular shape, [162] which cannot be achieved with most “classical” film deposition methods like molecular beam epitaxy or physical and chemical vapour deposition. Therefore CBD is the method of choice for coating purchasable latex beads, which are used as sacrificial templates in the present study.

Recently, we presented a method to obtain uniform films of nanocrystalline zinc oxide on flat substrates by CBD applying a bio-inspired approach. [127] The term bio-inspired materials synthesis refers to the attempt to adopt the principles of biomineralization for the fabrication of synthetic materials since biominerals generally have amazingly favourable properties although organisms produce them with little expenditure at near-ambient temperature. As the secret of biomineralization is control by organic templates, using a bio-inspired approach includes either the deposition on an organic substrate or the control of the process by organic additives in solution or both.

In the present paper, this method is adopted for the deposition of a zinc oxide coating on polymer microspheres with a sulfonate-modified surface. By subsequent disintegration of the polymer core, micrometer-sized hollow spheres (microcapsules) of zinc oxide are fabricated. It will be shown that the process is cheap and simple, that there is no need for prior preparation of nanoparticles or templates of unusual materials, and that the resulting spheres are well-shaped and stable.

## **6.2 Experimental**

### **6.2.1 Templates**

An aqueous dispersion of monodisperse polystyrene beads (micromer<sup>®</sup>, micromod) with a nominal diameter of 2  $\mu\text{m}$  and a sulfonate-functionalized surface was purchased ready for use. Before use, the beads were washed in methanol (VLSI selectipur, BASF) at least twice: After centrifuging the dispersion for 20 minutes at 535g, the supernatant was removed and replaced by the same amount of fresh methanol. The microspheres were dispersed again by vigorous shaking on a vortexing machine. The centrifugation and redispersion were repeated once more. In order to illustrate the difference between coated and uncoated microspheres, a drop of the dispersion containing the uncoated beads was dried on a silicon wafer and imaged in the scanning electron microscope (Figure 6.1).

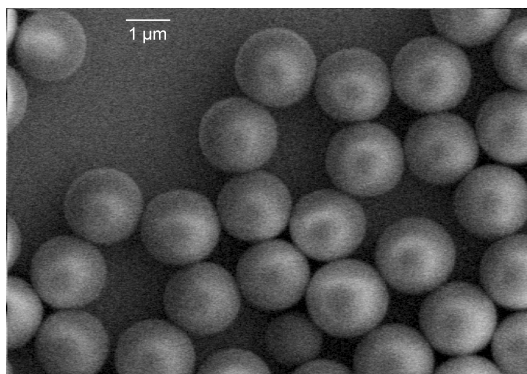


Figure 6.1: SEM image of uncoated, sulfonate-modified PS microspheres.

### 6.2.2 Precursor solution

$\text{Zn}(\text{CH}_3\text{COO})_2 \cdot 2 \text{H}_2\text{O}$  (puriss. p. a., Fluka) was dissolved in methanol to a concentration of  $40 \text{ mmol}\cdot\text{l}^{-1}$ . With the aid of ultrasound, polyvinylpyrrolidone (PVP) with an average molecular weight of  $M = 10\,000 \text{ g}\cdot\text{mol}^{-1}$  (PVP10, Aldrich) was dissolved in methanol to a concentration of  $20 \text{ mmol}\cdot\text{l}^{-1}$ . 45 ml of the zinc acetate solution were mixed with 90 ml of the PVP solution. Under gentle stirring, 45 ml solution of tetraethylammonium hydroxide (TEAOH, purum, Fluka) in methanol with a concentration of  $100 \text{ mmol}\cdot\text{l}^{-1}$  were added dropwise using a peristaltic pump at a flow rate of  $1.5 \text{ ml}\cdot\text{min}^{-1}$ . To prevent evaporation and aging, the precursor solution was stored in a closed jar at  $4 \text{ }^\circ\text{C}$  and used within a week after preparation.

### 6.2.3 ZnO coating

A sample from the original dispersion of the polymer microspheres in methanol was centrifuged, the supernatant is disposed off, and the microspheres were redispersed in 10 ml precursor solution, so that the bead concentration becomes  $50 \text{ }\mu\text{g}/\text{ml}$ . This dispersion was heated to  $60 \text{ }^\circ\text{C}$  in a closed jar. After 1.5 h under continuous stirring, the dispersion was centrifuged for 20 min at  $535\text{g}$ , whereupon the supernatant was removed and replaced by the same amount of fresh precursor solution. The microspheres were dispersed again by vigorous shaking on a vortexing machine, and the dispersion was heated again. After 10 such cycles, each including immersion of the templates in the heated deposition solution for 1.5 h and subsequent centrifugation, the beads were washed in methanol and stored as a dispersion in methanol in a closed jar at  $4 \text{ }^\circ\text{C}$ . When required, the beads were dried by evaporation of the methanol at ambient conditions.

#### 6.2.4 Removal of the polymer templates

In order to remove the polystyrene cores from the zinc oxide microcapsules, pyrolysis or dissolution in a nonpolar solvent was used. For pyrolysis, 50  $\mu\text{l}$  of the dispersion of the beads in methanol were spread on a silicon wafer. After the methanol had evaporated at room temperature, the wafer was heated to 450  $^{\circ}\text{C}$  for one hour in air. For dissolution, the dispersion with the beads was centrifuged for 20 min at 535 $\cdot$ g. The supernatant methanol was replaced by chloroform, and the dispersion in chloroform was stirred vigorously for one hour. After that, it was centrifuged for 20 min at 535 $\cdot$ g again, redispersed in fresh chloroform, and stored in a closed jar at 4  $^{\circ}\text{C}$ . When required, the capsules were dried by evaporation of the chloroform at ambient conditions.

#### 6.2.5 Sample characterization

The ZnO films achieved were characterized by scanning electron microscopy (SEM), focused ion beam (FIB), and X-ray diffraction (XRD).

Scanning electron microscopy (SEM) was done using a JEOL JSM-6300 F with an accelerating voltage of 3 kV and a working distance of 15 mm and a Zeiss DSM 982 Gemini at accelerating voltages of 3 to 5 kV and working distances of 3 to 5 mm.

Additionally, cross-sections and slices of the microspheres or the resulting microcapsules were prepared by a dual-beam instrument (FEI Nova NanoLab 600) including both a focused ion beam (FIB) and a SEM. The specimen was placed at the coincidence point of the electron and the ion beam, which is positioned 5 mm below the objective lens of the SEM. Then the specimen was tilted by 52 $^{\circ}$  resulting in a perpendicular incidence of the ion beam. This position allows simultaneous viewing with the SEM during FIB cutting. In the present investigation, an acceleration voltage of 2 kV was used for the SEM, and the Ga ions of the FIB were accelerated with 30 kV. The spheres were spread on a silicon wafer by 50  $\mu\text{l}$  dispersion, and afterwards the solvent was evaporated at room temperature. Prior to the cutting with the FIB, the spheres were coated with a protective Pt layer using a metal-organic precursor gas which is decomposed in the ion beam. Finally, a cross-section was dissected or a slice excised with FIB, while the cutting was simultaneously monitored using the SEM. SEM images from cross-sections of coated spheres were also used to determine the thickness of the coatings.

X-ray diffraction (XRD) diagrams were taken with a Philips X'Pert instrument in Bragg-Brentano geometry using only Cu  $K\alpha_1$  radiation with  $\lambda = 0.15406$  nm by means of a primary monochromator. Scherrer analysis of the diffraction diagrams was done in the following way: A superposition of Lorentz maxima with interdependent full widths at half maximum (FWHM)  $\gamma$  was fitted to the (100), (002), and (101) peaks of the ZnO diffraction diagram. The average crystallite diameter  $d$  was then calculated using the Scherrer formula  $d = \frac{0.94 \cdot \lambda}{\gamma \cdot \cos \theta}$ , where  $\lambda$  is the source wavelength, and  $2\theta$  the peak position. Instrumental broadening can be neglected since its contribution to the FWHM is only about  $0.04^\circ$  in the measured range of scattering angles.

### 6.3 Results

XRD diffractograms (Figure 6.2) of the dried coated spheres exhibit the typical peaks of zincite: (100) at  $31.8^\circ$ , (002) at  $34.6^\circ$ , and (101) at  $36.3^\circ$ . This means that the coatings consist of polycrystalline zinc oxide. According to the Scherrer analysis of the XRD data, the grain size in the coatings is about 8 nm. Because of the curvature of the templates, XRD cannot answer the question whether the films are textured with respect to the substrate surface.

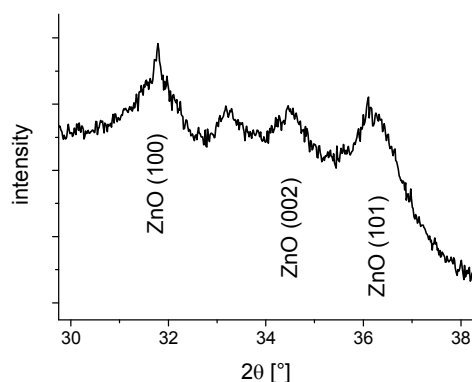


Figure 6.2: XRD diffractogram of PS microspheres with a ZnO coating.

SEM images show that a full coverage of the PS microspheres can be achieved (Figure 6.3). The films seem not quite as smooth as the ones deposited on flat sulfonate-SAMs which exhibit route mean squared deviations in height of less than 5 nm, [127] but still the beads are coated with a film of extraordinarily uniform thickness compared to the products of other processes. Cross-

sectional images of coated spheres (Figure 6.4) affirm that the templates are coated uniformly, and that the films are homogeneous, yet not with a particularly smooth surface. The thickness of the ZnO coating is about 160 nm, which is at the lower end of the range of typical thicknesses of ZnO films deposited on a sulfonate-modified SAM by the same process and after the same number of deposition cycles.

In a previous study [127] the influence of the number of deposition cycles on the film thickness was investigated thoroughly. A nearly linear increase of the film thickness with the number of deposition cycles applied was observed. Though in that investigation flat substrates were used, they were also furnished with a sulfonate-modified surface, so the results are valid for the spherical templates in the present study. It is, however, important to consider that initially film formation occurs by island growth. So if significantly fewer than ten deposition cycles are applied, or if a multiple of the suggested concentration of PS microspheres is dispersed in the deposition solution, no continuous ZnO film is formed on the templates. This indicates that a certain minimum number of deposition cycles must be applied in order to obtain cohesive shells, and shells with a thickness of less than 50 to 100 nm will not be stable after removal of the PS core. In contrast, the wall thickness of the capsules can easily be adjusted to higher values by increasing the number of deposition cycles.

Polystyrene with a sulfonate-modified surface has been chosen as the template material since previous experiments with flat substrates [127] indicated that the sulfonate moieties are particularly compatible with ZnO. This compatibility is attributed to the relatively high surface charge of sulfonate-modified surfaces which favours the mechanism of oriented attachment which has been observed for the formation of ZnO films from solutions containing PVP as an additive. [84] Though experiments have shown that on flat PS substrates with an unmodified surface some scattered islands of ZnO can be deposited, sulfonate-modified PS was preferred for the microcapsule fabrication since it was expected to provide for a denser and faster growing coating.

As suggested in previous publications, [84,127] the deposition of the ZnO film happens via the formation of ZnO nanocrystals in solution and the subsequent assembly on the template via oriented attachment. [12,66] By variation of the concentration of the additive PVP, crystallization and aggregation at the surface of the template can be controlled.

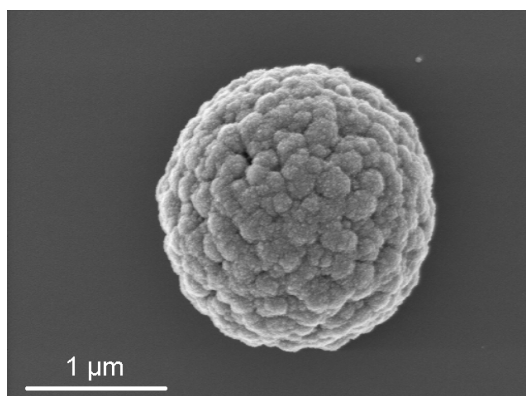


Figure 6.3: SEM image of a PS microsphere coated with ZnO.

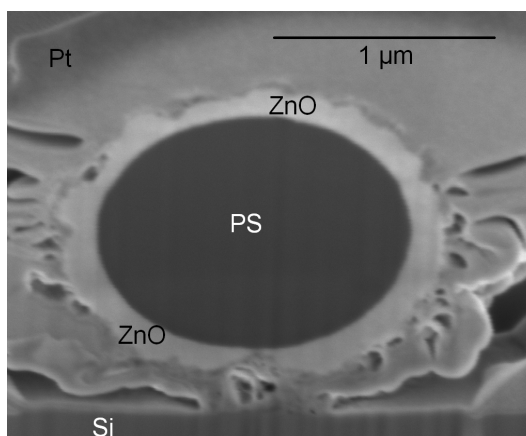


Figure 6.4: SEM image of a tilted cross-section of a PS microsphere coated with ZnO. Note that the scale bar is only valid for the horizontal since the vertical is distorted because of the tilting by  $52^\circ$ . This is also the reason why the cross-section seems oval instead of circular.

Neither after exposing the coated spheres to chloroform (Figure 6.5a) nor after heating them to  $450^\circ\text{C}$  (Figure 6.5b) was any change visible from the outside of the spheres. The spheres did not break, and the ZnO films did not crack or peel off. Slices cut from the spheres treated with one of these two methods have spherical openings through which the background behind the slice can be seen. So it is evident that the PS has disappeared from the spheres both after dissolution (Figure 6.6a) and after pyrolysis (Figure 6.6b) of the core. The results of treatment with heat or with chloroform are absolutely identical, so for possible applications the more suitable process can be chosen arbitrarily every time. In some of the investigated samples, which have been treated with chloroform or heat only for one hour, a small amount of PS is left over inside the ZnO shell. The remaining PS could easily be disposed off by prolonging the times of treatment in chloroform or in the oven, respectively.

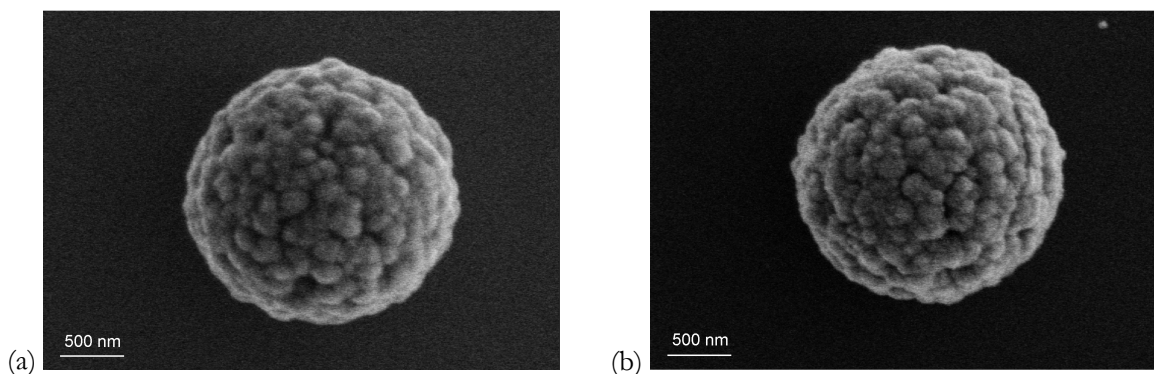


Figure 6.5: SEM images of a ZnO hollow sphere (a) after dissolution of the PS core in chloroform, (b) after thermal decomposition of the PS core at 450 °C.

It is important to note that the ZnO shells endure the removal of the PS cores without any damage, and that even the centrifugation steps after dissolution of the core in chloroform did not harm them. This means that the mechanical stability of the ZnO films deposited from solutions of zinc acetate, PVP, and TEAOH in methanol is astonishingly good. Since the ZnO shells did not crack during removal of the cores, it is concluded that they contain pores through which the organic matter could vanish.

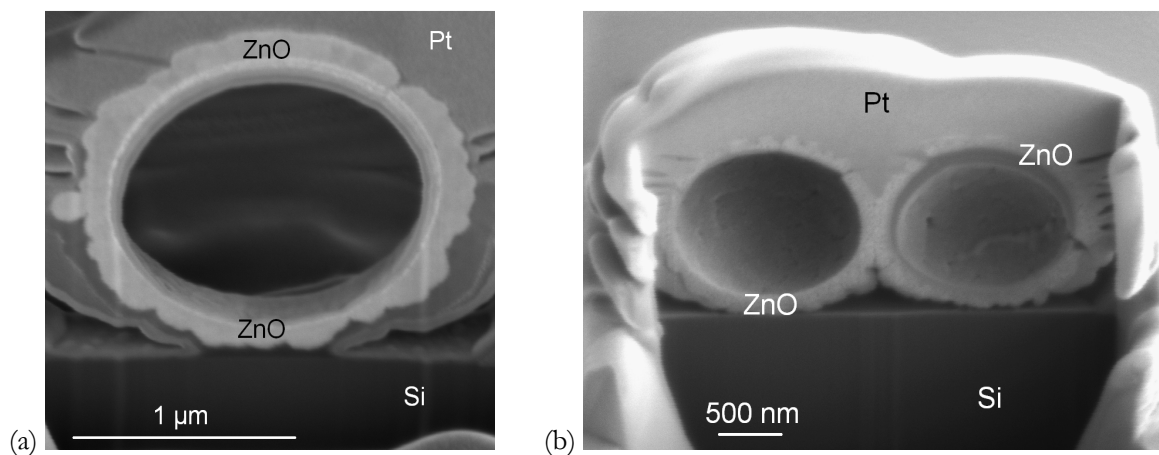


Figure 6.6: SEM images of tilted cross-sections of ZnO hollow spheres (a) after dissolution of the PS core in chloroform, (b) after thermal decomposition of the PS core at 450 °C. In (a) a thin slice was cut, while in (b) only parts of the spheres were removed. Therefore the internal surface of the shells is visible in both images, whereas in (a) additionally the background is visible through the void in the shell. In the right microcapsule in (b) the PS has not been thermolysed completely, and some remnant is left close to the upper wall.



## 6.4 Discussion and outlook

The viability of the present approach is the first experimental evidence of the applicability of the CBD of ZnO to curved surfaces. Furthermore it expands the potential of the present process to other sulfonate-modified surfaces apart from the previously used self-assembled monolayers (SAM) of alkylsiloxanes. Last but not least it demonstrates the high mechanical stability of the thus obtained ZnO films. In fact, hollow ZnO microcapsules made by the sacrificial template route would be a convenient model system for testing the mechanical properties of ZnO thin films by atomic force spectroscopy [163] since there is no substrate to influence or distort the measured values.

The inner void of the ZnO hollow spheres is, of course, nearly perfectly spherical. As island growth is involved in film formation, a completely uniform wall thickness cannot be achieved. After a sufficient number of deposition cycles, however, the islands merge, so that full coverage of the template is permitted, and a homogeneous minimum film thickness of a few dozen nanometers is provided for. Further away from the template, however, dents and canyons still occur. Together with the granular surface which is due to the nanocrystalline microstructure, these impressions give the shells their characteristic rough appearance. Spheres which were misshapen because of irregular growth or because of adhering large agglomerates were not observed. To our knowledge, there have not been any reports of ZnO microcapsules with a more uniform wall thickness. Furthermore, compared to ZnO hollow spheres produced without the use of monodisperse templates, even the diameter of the present spheres hardly varies.

Only very few of the ZnO shells crack or come apart during removal of the PS core or during preparation for further investigation, which implies that the proportion of cull is very low, unlike with many of the other methods of ZnO microcapsule production presented in the introduction of this chapter. The process is simple and robust and can be realized with a set-up and cheap raw materials that are commercially available. Due to the use of a sacrificial template, it is not possible to both synthesize and fill the capsules in one step, so other methods for posterior filling must be developed. The deposited ZnO films show a certain degree of porosity which permits the removal of the PS core without destruction of the shell; this porosity might also be exploited for filling.

## **6.5 Acknowledgements**

The authors wish to thank Dr. Udo Welzel, Maritta Dudek and Gerd Maier for recording the XRD diffractogram, Sabine Kühnemann and Hartmut Labitzke for taking the SEM images, and Ulrike Eigenthaler for operating the dual beam instrument.





- 7. Laminates of zinc oxide and poly(amino acid) layers with enhanced mechanical performance**

**Abstract**

Nanostructured composite systems of alternating organic and inorganic layers were prepared by a bio-inspired process. The mineral component was zinc oxide. As the organic component, polyelectrolyte multilayers were prepared using polystyrene sulfonate and poly(amino acids). These laminates have typical properties in common with nacre: they consist of nanocrystals in a matrix of biomolecules, they exhibit a texture, and they proved to be harder than the monolithic mineral.

## 7.1 Introduction

Nacre consists of 95 vol.-% calcium carbonate, but it is about 3000 times as tough [164,165] and about twice as hard as bulk  $\text{CaCO}_3$ . [166,167] It is built up of aragonite platelets embedded in a protein-based matrix. [168] Experiments were performed [169] and theoretical models have been developed [170] with the aim to explain this astonishing performance. Particular attention has been turned to the effects of the combination of soft organic and brittle inorganic materials, [171,172] and to the stratified structure of nacre. [173] Synthetic composite organic-inorganic layer structures were fabricated hoping that they would exhibit similarly favourable properties. Apart from numerous attempts to produce  $\text{CaCO}_3$ -based “synthetic nacre”, [174] silica, [175] alumina, [176] titania, [177] and indium tin oxide (ITO) [178] have been used as the inorganic component. The organic layers consisted mostly of synthetic polymers. Indeed a stacked composite system consisting of particulate amorphous titania on the one hand and polyelectrolyte multilayers on the other hand exhibited mechanical properties better than the corresponding bulk titania. [179] However even when both constituents were inorganic, a multilayer structure proved advantageous. [180]

In this study, nacre is mimicked by a laminate of nanocrystalline zinc oxide alternating with polyelectrolyte multilayers. The main component of the polyelectrolyte multilayers are poly-(amino acids), i. e. biomolecules. The crystallinity of the inorganic component and the use of biomolecules place the synthetic composite close to the natural material and raise the expectation that the ZnO-based laminate exhibits favourable mechanical properties. Comparable layer structures based on ZnO have not been reported before.

## 7.2 Experimental section

Polished p-type boron-doped single-crystal Si (100) wafers were used as supports for the multilayer systems. Prior to use, they were cleaned by wiping with chloroform, acetone, and ethanol. Subsequently, they were oxidized in Piranha solution for one hour at 90 °C and washed abundantly with distilled water afterwards. Piranha solution was mixed freshly prior to use out of 7 volume units concentrated  $\text{H}_2\text{SO}_4$  and 3 volume units  $\text{H}_2\text{O}_2$  (30 wt.-% in water).

Each organic layer consists of a multilayer of alternately positively and negatively charged polyelectrolytes (PE) prepared as a layer-by-layer assembly (LBL) via dip-coating. [23] Poly(sty-

rene sulfonate) (PSS,  $M \approx 70\,000\text{ g}\cdot\text{mol}^{-1}$ , Aldrich, USA) and the poly(amino acids) poly-L-glutamic acid (PLGA,  $M = 15\,000 - 50\,000\text{ mol}\cdot\text{ml}^{-1}$ , Fluka, Switzerland) and poly-L-lysine hydrobromide (PLL,  $M = 15\,000 - 30\,000\text{ mol}\cdot\text{ml}^{-1}$ , Sigma, USA) were each dissolved in water to a concentration of  $1\text{ mg}\cdot\text{ml}^{-1}$ . The pH of the poly-L-lysine solution was adjusted to 9 by dropwise addition of  $3\text{ mol}\cdot\text{l}^{-1}$  KOH lye. Every single polyelectrolyte layer was deposited by incubation of the substrate in the respective polyelectrolyte solution for 20 minutes and subsequent washing by repeated dipping in deionized water for 5 minutes. For thoroughness, the washing routine was split up into four stages, using a different vessel of water every time. By repeating this routine alternatingly with cationic and anionic polymers, a multilayer with the sequence (PLL – PLGA)<sub>5</sub> – PLL – PSS was deposited on the silicon. On top of the PSS, an inorganic layer of ZnO was deposited by the method which is described below. Before the second (or third etc.) ZnO layer was deposited, the previous one was coated with another organic layer, this time with the sequence PSS – (PLL – PLGS)<sub>2</sub> – PLL – PSS. Repeating the dip-coating with the polyelectrolytes and the ZnO deposition alternatingly, a composite layer stack was created. The dip-coating was done either manually or with the help of the dipping robot DR 3 (Riegler & Kirstein, Germany).

For comparison, in some cases a self-assembled monolayer (SAM) of sulfonate-modified alkylsiloxanes was used as the first organic layer instead of a polyelectrolyte multilayer. The SAM was chemically bound to the native silicon oxide on top of the silicon wafer. SAM deposition took place under argon atmosphere. 1-thioacetato-16-trichlorosilyl hexadecane was synthesized according to established procedures [65,102] and dissolved in toluene to a concentration of 2 vol.-%. The surface-oxidized silicon wafers or glass slides were immersed in the solution and kept there for 5 hours. During deposition, the solution was cooled to about 4 °C. Afterwards, the substrates were washed with chloroform and methanol. The thioacetate functionality was oxidized to sulfonate by placing the substrates in a saturated aqueous solution of potassium hydrogen monopersulfate for at least 12 hours. Subsequently, the substrates were washed abundantly with distilled water and dried in a stream of argon. On the SAM-coated substrates, the next, inorganic, layer was deposited immediately.

ZnO deposition solutions were prepared according to a previously published procedure. [127] For a precursor solution with  $[\text{PVP}] : [\text{Zn}^{2+}] = 1,0$ ,  $\text{Zn}(\text{CH}_3\text{COO})_2 \cdot 2\text{ H}_2\text{O}$  (puriss. p. a., Fluka) was dissolved in methanol (VLSI selectipur, BASF) to a concentration of  $40\text{ mmol}\cdot\text{l}^{-1}$ . With the aid of ultrasound, polyvinylpyrrolidone (PVP10, Sigma-Aldrich) with an average molecular weight of  $10\,000\text{ g}\cdot\text{mol}^{-1}$  was dissolved in methanol to a concentration of  $20\text{ mmol}\cdot\text{l}^{-1}$ . 60 ml of the zinc acetate solution were mixed with 120 ml of the PVP solution. Under gentle stirring, 60 ml of a solution of tetraethylammonium hydroxide (TEAOH, purum, Fluka) in methanol



with a concentration of  $100 \text{ mmol}\cdot\text{l}^{-1}$  was added dropwise using a peristaltic pump at a flow rate of  $2 \text{ ml}\cdot\text{min}^{-1}$ . To prevent evaporation of the solvent or premature ZnO formation, the precursor solution was stored in a closed jar at  $4 \text{ }^\circ\text{C}$  and used within ten days after preparation.

For ZnO deposition, a  $10 \times 10 \text{ mm}^2$  Si wafer or glass platelet coated with a sulfonate-modified SAM or a polyelectrolyte multilayer was placed in a 1 ml aliquot of precursor solution in a closed jar, which was heated to  $60 \text{ }^\circ\text{C}$  in an oil bath. Alternatively, up to twelve substrates were immersed in 22.5 ml of precursor solution in a specially designed reaction vessel at  $60 \text{ }^\circ\text{C}$ . After 1.5 hours the solution was replaced by fresh deposition solution. For each ZnO layer, five such cycles were conducted before the substrate was removed and washed abundantly with distilled water. In order to obtain the monolithic ZnO films, which were used for the purpose of comparison, the same total number of ZnO deposition cycles was applied as for the composite films, i. e. a  $(\text{PE} - \text{ZnO})_4$  composite film was compared to a ZnO film deposited in 20 cycles. The monolithic films were deposited on sulfonate-SAMs.

Scanning electron microscopy (SEM) was done using a JEOL JSM-6300 F with an accelerating voltage of 3 kV and a working distance of 15 mm. Cross-sectional specimens of the deposited films were obtained by cracking the brittle silicon substrate bearing the film. Using wire-cutting pliers, a small notch was made on the substrate edge to control the position of the crack.

X-ray diffraction (XRD) diagrams were recorded with a Philips X'Pert instrument in Bragg-Brentano geometry using only  $\text{Cu-K}\alpha_1$  radiation by means of a primary monochromator. Scherrer analysis of the diffraction diagrams was done in the following way: Three Lorentz maxima with interdependent full widths at half maximum (FWHM)  $\gamma$  were fitted to the (100), (002), and (101) peaks of the ZnO diffraction diagram. The average crystallite diameter  $d$  was then calculated using the Scherrer formula:  $d = \frac{0.94 \cdot \lambda}{\gamma \cdot \cos \theta}$ , where  $\lambda = 0.154056 \text{ nm}$  is the source wavelength, and  $2\theta$  the peak position. Instrumental peak broadening was neglected since it is insignificant compared to peak broadening because of grain size effects.

Atomic force microscopy (AFM) images are recorded with a Digital Instruments Nanoscope III Multimode applying tapping mode with silicon cantilevers.

For transmission electron microscopy (TEM), a JEOL JEM-4000 EX with an accelerating voltage of 400 kV was used. A cross-sectional specimen for TEM was prepared according to the method established by Strecker et al., [103] i. e. a slice with a width of approximately 2.5 mm was cleaved from the wafer carrying the ZnO/PE composite film. The coated side of the sample slice was glued to a complementary piece of silicon with epoxy resin. Subsequently two more pieces of silicon were glued to both sides of the sample sandwich, so that the cross-section of the whole

sandwich reached about 3 mm in diameter, and the sandwich was embedded in a copper ring. Finally a thin slice with a thickness of 0.8 mm was cut with a wire saw. Both sides of the sample were ground and polished until the sample thickness was 80 – 100  $\mu\text{m}$  and smooth planes were obtained. One side was further ground and polished on a Gatan 656 Dimple Grinder until the thickness reached about 10 – 20  $\mu\text{m}$ . The sample was sputtered with  $\text{Ar}^+$  ions at 4 keV in a Gatan Duo 691 ion-milling machine on both sides till perforation.

The depth distributions of Zn, C, S, N, and Si in the oxide layer and the parent substrate were determined by sputter-depth profiling using Auger Electron Spectroscopy (AES). To this end, spectra of the Zn LMM, O KLL, S LVV, C KLL, N KLL and Si KLL lines were recorded with a JEOL Jamp 7830F using a primary electron beam of 10 keV and 16 nA (scanning an area of  $10 \times 10 \mu\text{m}^2$ ) and employing alternating ion sputtering intervals of 60 s (with a focused 500 keV  $\text{Ar}^+$  beam rastering an area of  $300 \times 300 \mu\text{m}^2$ ). The intensity-depth profiles of the various spectral contributions were resolved from the peak-to-peak heights in the corresponding differential AES spectra using the linear least-squares fitting procedure as implemented in the Phi-MultiPak software (version 5.0A).

X-ray Photoelectron Spectroscopic (XPS) analysis was performed with a Thermo VG Thetaprobe system employing monochromatic Al  $K\alpha$  radiation ( $h\nu = 1486.68 \text{ eV}$ ; spot size 400  $\mu\text{m}$ ). Detailed spectra of the Zn 2p, O 1s, C 1s and Si 2p regions were measured with a step size of 0.1 eV at a pass-energy of 100 eV.

Nanoindentation testing was performed with a scanning nanoindenter consisting of a depth-sensing force transducer (Hysitron Triboscope) combined with the scanning probe microscope Digital Instruments Nanoscope III Multimode in a way analogous to the work by Burghard et al. [181] A cube corner diamond indenter with a nominal tip radius of approximately 40 nm was used, which permits making small indentations while still creating plastic deformation. Working with very shallow indentation depths was facilitated by the high load and displacement resolution (100 nN and 0.2 nm, respectively) of the force transducer. All indentations were made applying the maximum force of 150  $\mu\text{N}$ , which was chosen in order to reach a maximum penetration depth of about 150 nm. The indentation force was varied during subsequent load/partial unload cycles over 25 steps, with automatic recording of the indentation depth after each step. Tip calibration within the penetration depth range of up to 150 nm was performed utilizing a fused silica standard sample.

### 7.3 Results and discussion

Nanoscale organic/inorganic laminates can be produced with little expenditure when in-situ mineralization of the inorganic layers is combined with layer-by-layer deposition of polyelectrolytes for the organic layers. In the case of ZnO, however, this procedure implied a particular challenge since ZnO dissolves rapidly in solutions of common polycations, like polyethyleneimine (PEI) and poly(allylamine hydrochloride) (PAH). [179] It was found that the poly(amino acid) poly(glutamic acid) (PLGA) is more compatible with ZnO, and therefore it was the cation of choice in the present work. For the best interplay with the PLGA, another poly(amino acid) was used as the polyanion: polylysine (PLL). On the other hand, the electrical charge of the surface is crucial for the deposition of ZnO, [127] and the relatively weakly charged PLGA is not ideal in that respect. Therefore each polyelectrolyte multilayer was terminated with layers of poly(styrene sulfonate) towards the ZnO. For the same reason, ZnO cannot be deposited on bare silicon, [127] so its surface must be modified, or the bottom layer of the laminate must be an organic one.

In cross-sectional images from scanning electron microscopy (SEM) the multilayer structure of the stacked composite systems is clearly visible (Figure 7.1). The ZnO layers appear granular, and they have a thickness of about 120 nm each. The polyelectrolyte interlayers are much thinner, about 9 nm in average (see discussion below), and not quite homogeneous in thickness. Because of their high carbon content they appear black in the SEM. PE/ZnO composite films are thinner than monolithic ZnO films, which were deposited applying the same number of ZnO deposition cycles, by nearly 20 %. This observation indicates that 1 mg·ml<sup>-1</sup> PLL solutions set to a pH of 9 still dissolve ZnO to a small extent.

X-ray diffraction (XRD) was performed in order to test composition and crystallinity of the samples. In fact, neither between monolithic ZnO films [182] and ZnO/polyelectrolyte composite films, nor between composite films with a SAM and with a polyelectrolyte as first layer, was any mentionable difference observed (Figure 7.2). The three typical ZnO peaks (100) at 31.9°, (002) at 34.7°, and (101) at 36.7° are present. Scherrer analysis of the diffractograms reveals an average grain size of 7 nm. The predominance of the (002) peak over the (100) and (101) peaks is evidence that even with the polyelectrolyte interlayers the ZnO is textured. Orientation of the  $\langle 001 \rangle$  axis perpendicular to the substrate is preferred. As it has been published previously, oriented attachment during the film formation is supposed to be the reason for the formation of a texture. [127]

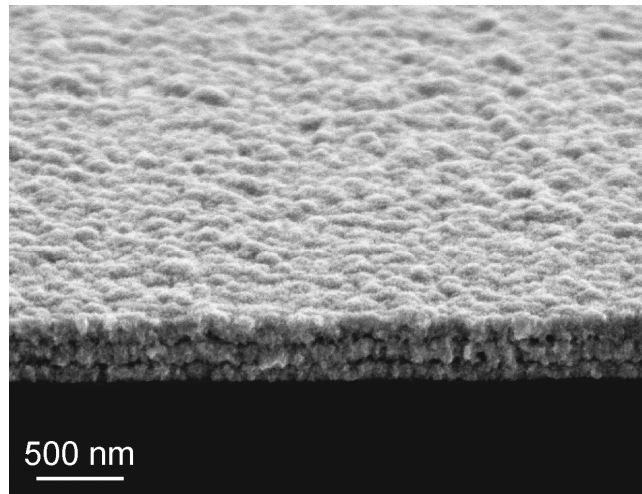


Figure 7.1: Scanning electron micrograph of a composite film with the layer structure SAM – ZnO – (PE – ZnO)<sub>2</sub>. The sample is tilted by 20°, so that both the cross-section and the surface of the film are visible. The thin organic layers between the thicker ZnO layers are visible as discontinuous black lines.

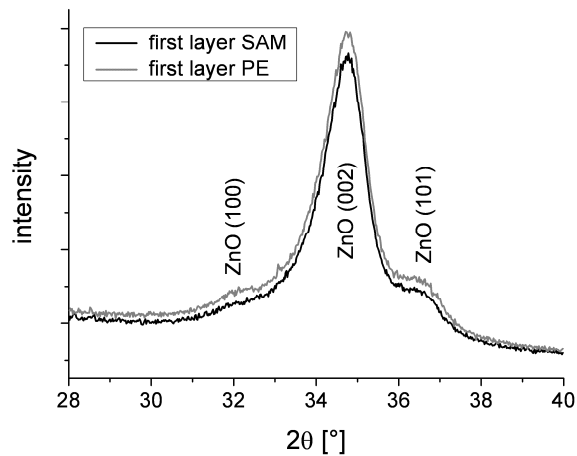


Figure 7.2: X-ray diffractograms of two composite films with the layer structures SAM – ZnO – (PE – ZnO)<sub>3</sub> (in black) and (PE – ZnO)<sub>4</sub> (in grey).

The atomic force microscopy (AFM) images in Figure 7.3 permit a comparison of the surface morphologies of monolithic ZnO and ZnO/polyelectrolyte multilayer films. The AFM data were analysed in order to obtain the root mean square (RMS) of the deviation in height, which is a measure of the roughness. For pure ZnO films with a thickness of about 0.5  $\mu\text{m}$  it was found to be 14 nm, whereas a roughness of 16 nm was obtained for composite films deposited applying the same number of ZnO deposition cycles. Consequently the integration of organic material into the films has practically no effect on the roughness. For pure ZnO film it has been shown

that the roughness depends hardly on the film thickness. [127] Both these results indicate that the deposition process is very robust.

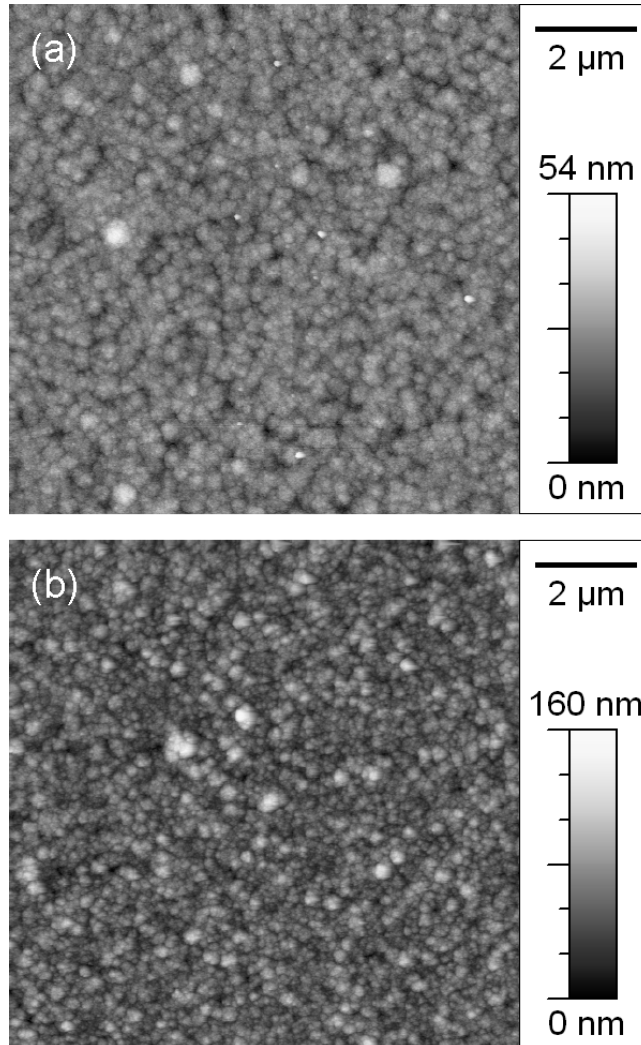


Figure 7.3: Atomic force microscopy images of (a) a monolithic ZnO film, and (b) a composite film with the layer structure SAM – ZnO – (PE – ZnO)<sub>3</sub>. Both films were fabricated applying the same total number of ZnO deposition cycles, and both have an approximate thickness of 0.5 μm.

AFM micrographs also permit the determination of the thickness of the polyelectrolyte films. For that purpose a film of six double layers of polyelectrolytes, i. e. (PLL – PLGS)<sub>6</sub>, was deposited on a silicon wafer and scratched with a plastic tweezer. The height difference between the PE coated and the blank surface was found to be 15 nm. It is concluded that the thickness of a single polyelectrolyte layer is about 1.3 nm. So in the ZnO/polyelectrolyte multilayers the average thickness of the PE interlayers is about 9 nm, and the bottom layer directly on the silicon support is about 15 nm thick.

A cross-sectional transmission electron microscopy (TEM) image of a quadruple composite film is shown in Figure 7.4. The inorganic layers are visible as grey regions with a thickness of approximately 120 nm, while the organic layers are visible as slightly brighter zones between the ZnO layers. They appear somewhat wavy and blurred, which indicates interpenetration between ZnO and the organic PE components. Interpenetration is not unexpected since the average thickness of the PE film is of the same order of magnitude, probably even somewhat lower, than the average roughness of the ZnO layers. The strong interaction between ZnO and PSS, and the observed slight solubility of ZnO in PLL solutions might also induce the formation of hybrid structures on a molecular level.

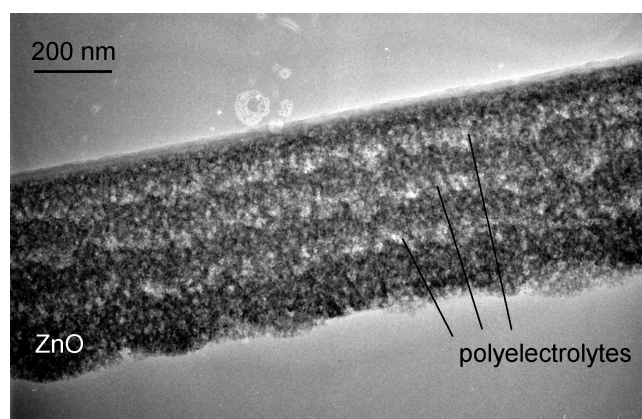


Figure 7.4: Cross sectional transmission electron micrograph of a composite film with the layer structure SAM – ZnO – (PE – ZnO)<sub>3</sub>. The topside of the film was facing the substrate. The Si wafer itself is not visible in the image since the film delaminated from the substrate during sample preparation for TEM.

The existence of a multilayered structure consisting of alternating ZnO layers separated by much thinner regions of PE organics is evident from the depth distribution of Zn, O, S, C and Si in the composite layer as measured by AES sputter-depth profiling (Figure 7.5a). Recognizing the extremely high sensitivity of AES for sulphur, the occurrence of a layered sequence of the organic-rich regions is most clearly reflected by the strong undulation of the S LVV signal with depth (Figure 7.5b; note that polyelectrolyte PSS and the SAM are the only sulphur-containing components in the system). The relatively much weaker undulation of the Zn, O and C signals can be explained on the basis of the relatively much lower sensitivity of AES for these elements and a much faster sputter rate within the organic region in combination with the interpenetration between the oxide and the organic PE components (as evidenced by TEM; see above). In addition some Si was detected by the AES analysis in the region of the composite layer adjacent to

the parent Si/SiO<sub>2</sub> substrate, which suggests that some Si from the parent substrate gets incorporated into the bottom part of the composite layer during the initial stages of the layer deposition process.

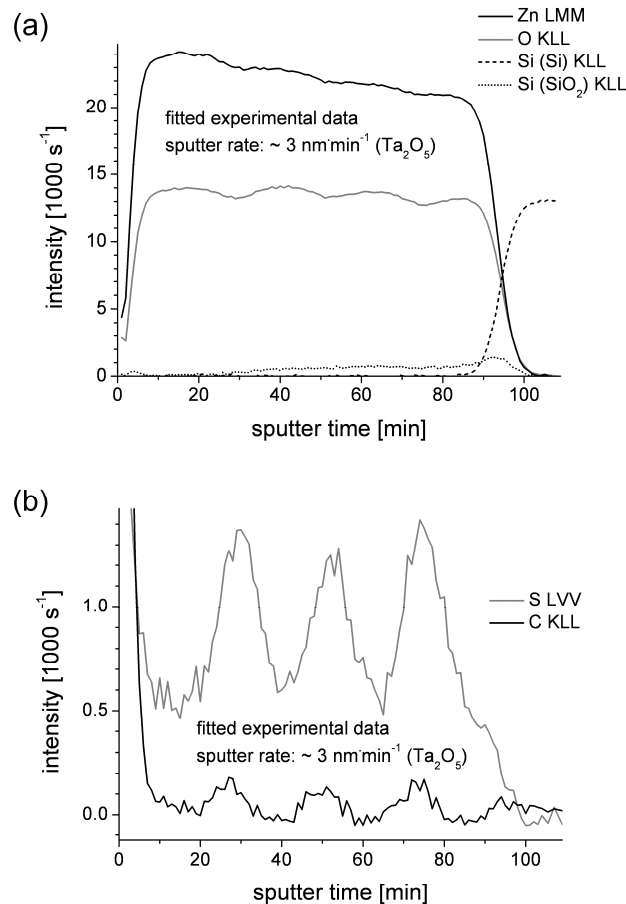


Figure 7.5: (a) Intensity-depth profile of the resolved elemental species in the SAM – ZnO – (PE – ZnO)<sub>3</sub> laminate and the parent substrate as obtained by AES sputter-depth profiling. The profiles demonstrate the existence of a structure of alternating ZnO layers separated by much thinner S-rich organic regions. In (b) the sulphur and carbon intensity-depth profiles pertaining to the measurement of (a) are enlarged. The two Si signals were attributed to elemental Si and SiO<sub>2</sub> according to the result of an XPS measurement.

The mechanical properties of the monolithic ZnO and ZnO/PE multilayer samples are tested by nanoindentation experiments. These tests are performed on films with a total thickness of about 0.5  $\mu\text{m}$ . Hardness and Young's modulus are derived from the measured load-contact depth curves following the procedure of Oliver and Pharr. [183] The hardness of the indented material is given by the indentation load divided by the projected area of contact at the applied load during the indentation. The Young's modulus of the sample is determined from the elastic

contact stiffness and the contact area. The contact stiffness is defined as the slope of the upper portion of the unloading curve during the initial stage of unloading. From Figure 7.6, in which the extracted hardness and Young's modulus are plotted as a function of contact depth, it is apparent that the presence of the organic-inorganic multilayered structure greatly enhances the mechanical stability of the films compared to the monolithic ones. The stronger dependence of the Young's modulus on the contact depth, as compared to the hardness, can be understood from the fact that for the same indentation depth, the elastic deformation field under the indenter extends further into the films than the plastic deformation field. [184] Therefore the values of the Young's modulus were considered typical when they were measured at lower penetration depths than the corresponding values of the hardness.

If in nanoindentation the penetration depth is smaller or similar to the value of the RMS roughness, i. e. about 15 nm for the present samples, the data obtained are generally adulterated by the surface roughness of the sample. Moreover, a marked influence from the substrate is recorded for indentation depths larger than 20 % [185] of the total film thickness. These limitations were taken into account, and only data obtained from the intermediate penetration depth range, i. e. between 40 and 100 nm, was evaluated.

A hardness of about 1.7 GPa was measured for the monolithic ZnO film, and around 2.1 GPa for the multilayer sample (Figure 7.6a). The difference corresponds to an increase by 24 % owed to the organic-inorganic multilayer structure. The enhanced hardness of the nanocomposites in comparison to the monolithic coatings is attributed to the following mechanism: The combination of a soft (PE multilayers) and a hard (ZnO) material of different shear modulus results in increased external stresses required to drive the deformation field from one material to another, as it has been asserted by theory. [186] For polyelectrolyte multilayers similar to the ones in the present samples, shear moduli between 3 and 150 MPa have been reported, [187] while a value of about 15 GPa is calculated for the ZnO layer from the measured Young's modulus by using the well known relation between Young's modulus and shear modulus  $G = \frac{E}{2(1 + \mu)}$  and

assuming a Poisson's ratio of  $\mu = 0.356$ . [188] Hardening by differences in shear modulus has previously been reported for polycrystalline multilayer coatings, in which the movement of dislocations across the interface is blocked. [189] Interpenetration of the ZnO- and polyelectrolyte layers might even enhance this effect. Young's modulus is nearly the same for the composite and the monolithic films. Approximately 35 GPa in the pure ZnO and about 40 GPa in the multilayer film (Figure 7.6b) were measured, but the difference is insignificant since the error bars are overlapping. This result is astonishing since in the case of isostress usually layered composites of a



stiff mineral and a soft organic substance exhibit a lower Young's modulus than the pure mineral, [190] in contrast to the observations made on the present system. The question why no decrease of Young's modulus was observed, remains unanswered by the established theories and may be due to the particular interaction between the ZnO and the polyelectrolytes.

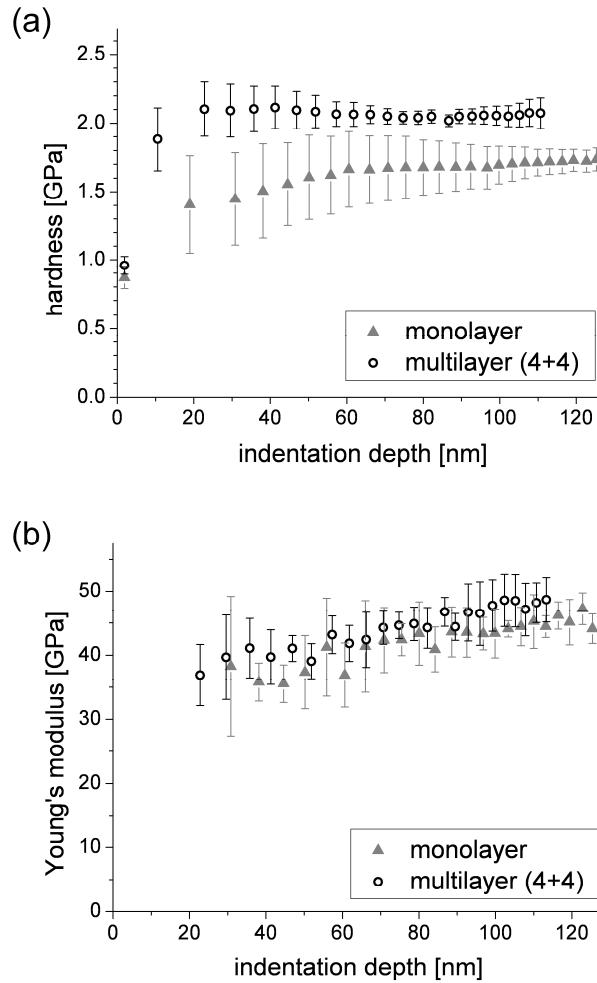


Figure 7.6: (a) Hardness and (b) Young's modulus as a function of penetration depth as measured by nanoindentation. The data shown in black was obtained from a monolithic ZnO film, the data shown in green from a composite film with the layer structure  $(PE - ZnO)_4$ . Both films were fabricated applying the same total number of ZnO deposition cycles, and both have an approximate thickness of  $0.5 \mu\text{m}$ .

Admittedly, both hardness and Young's modulus of the monolayer samples are inferior to bulk single-crystalline zinc oxide, [191] which can be explained by the porous and polycrystalline structure of the films. Indeed calculations have shown that in ZnO a porosity of 25 % results in a decrease in hardness of more than 50 % and a decrease in Young's modulus of nearly 70 %. [188]

Nevertheless the mechanical performance is comparable to that reported for nanocrystalline ZnO derived from gas phase condensation and annealed at 300 °C, [192] in spite of the lower temperature and expenditure of the CBD process.

## 7.4 Conclusion

In this paper, the example of ZnO/biopolymer composites demonstrates that the combination of the CBD method with LBL assembly offers valuable access to multilayered films with nacre-like architecture. This bio-inspired approach allows tuning of the composition of nanostructured thin films on the nanometer length scale, and hence constitutes a powerful tool for constructing materials with unique mechanical properties. The combination of nanocrystalline ZnO with poly(amino acids) permits a great enhancement of the mechanical performance, i. e. a significant increase in hardness without any negative impact on the stiffness. Possibly the mechanical properties of the composite films might be improved even further by optimizing their structure, including the thickness ratio of the organic and inorganic layers, the structural integrity and the coupling strength of the oxide grains. However the sensitivity of ZnO to acids, lyes, and ionic solutes might limit the viability of these attempts. Another interesting future goal is to determine the fracture toughness of the ZnO/biopolymer composites and compare it to the fracture toughness of monolithic films. One possible approach to tackle this question might be tensile tests on freestanding films obtained after deposition on sulfonate-modified polystyrene and subsequent removal of the template. [142]

## 7.5 Acknowledgements

The authors wish to thank Bernhard Siegle for the AES measurements, Michaela Wieland for the XPS measurements, Sabine Kühnemann for the SEM images, Dr. Udo Welzel and Maritta Dudek for the XRD diffractograms, Marion Kelsch for the preparation of the TEM sample, Dr. Paul Bellina and Dr. Peter van Aken for valuable discussions about TEM, and Peter Gerstel for the synthesis of the silane.





## 8. Kurzfassung der Dissertation

### 8.1 Einleitung und Überblick

Traditionelle Methoden zur Synthese keramischer Werkstoffe erfordern hohen Energieaufwand, oder sie erfolgen bei extremen Drücken und Temperaturen, was sie sehr kostspielig macht. [1] Insbesondere die Herstellung von Bauteilen mit komplexer Geometrie ist sehr aufwendig. Die belebte Natur zeigt, wie sich sehr komplexe Formen praktisch unter Umgebungsbedingungen bezüglich Temperatur, Druck und Atmosphäre erzeugen lassen. Beispiele sind Biomineralien wie Knochen, Zahnschmelz oder den Schalen von Weichtieren. [2] Besonderes Interesse der Forschung weckt das Perlmutter durch seinen irisierenden Glanz und seine mechanische Stabilität. Grund für seine Eigenschaften ist sein Gefüge: Aragonitplättchen in der Größenordnung von einigen hundert Nanometern sind in eine proteinhaltige Matrix eingebettet. [4]

Bei der bioinspirierten Materialsynthese werden die Prinzipien der Biomineralisation auf die Herstellung künstlicher Werkstoffe angewandt. [5] Dabei interessieren vor allem solche Stoffe, die in der Natur nicht vorkommen, aber für technische Anwendungen gefragt sind. Ziel ist es, bei niedrigen Temperaturen Werkstoffe mit herausragenden Eigenschaften herzustellen. Dazu findet wie bei der Biomineralisation die Abscheidung aus einer Lösung auf organischen Oberflächen oder in organischen Matrizen statt, und organische Hilfsstoffe in der Abscheidungslösung steuern den Prozess. [8]

In der vorliegenden Arbeit wird ein Verfahren angewandt, das als Abscheidung aus dem chemischen Bad bezeichnet wird und speziell für die Abscheidung von Metallchalkogeniden aus Salzlösungen entwickelt wurde. Dabei werden lösliche Metallsalze durch eine Erhöhung des pH-Werts und geringfügiges Aufheizen der Lösung hydrolysiert, um mit geringem technischen Aufwand Schichten auf Substraten abzuscheiden, ohne dass Redoxreaktionen erforderlich wären. [12]

Um Zinkoxid-Dünnschichten herzustellen, wird die Abscheidung aus dem chemischen Bad mit den Prinzipien der bioinspirierten Materialsynthese kombiniert. Zinkoxid wurde ausgewählt, da es als transparenter Halbleiter für zahlreiche Anwendungen in der Optik, Elektronik und Chemie von Bedeutung ist [82] und die Herstellung von hochqualitativem Zinkoxid bisher besonders aufwendig und teuer war.

Zunächst wird anhand des Beispiels von Aminosäuren und Dipeptiden gezeigt, welche Vielfalt an Morphologien und chemischen Zusammensetzungen von Zinkverbindungen durch den Einsatz organischer Hilfsstoffe bei der Abscheidung aus wässrigen Lösungen erzeugt werden kann. Andere Additive wie synthetische Polymere und Zucker werden im Hinblick darauf unter-

sucht, ob sie die Abscheidung homogener Zinkoxidschichten ermöglichen. Da mit Polyvinylpyrrolidon (PVP) die besten Ergebnisse erzielt wurden, wurde die Abscheidung in dessen Gegenwart weiter erforscht. Die Zusammensetzung und die wichtigsten Eigenschaften der abgeschiedenen Schichten werden vorgestellt, und es wird gezeigt, dass sich durch eine entsprechende Vorbehandlung der Substratoberfläche strukturierte Schichten erzeugen lassen. Um den Abscheidungsmechanismus und Kristallisationsprozesse in Lösungen generell besser zu verstehen, wurden die Vorgänge in den Abscheidungslösungen genau untersucht. Es wurde ein mehrstufiger Prozess vorgefunden, der über amorphe Zwischenstufen läuft und vom PVP auf komplexe Weise gesteuert wird. Um die vielfältigen Einsatzmöglichkeiten der Synthesemethode zu zeigen, wurden Zinkoxid-Mikrokapseln mittels „verlorener Kerne“ hergestellt sowie Komposite, die aus abwechselnden Schichten von Zinkoxid und organischem Material bestehen und verbesserte mechanische Eigenschaften aufweisen.

## **8.2 Von Aminosäuren und Dipeptiden gesteuerte Mineralisation in wässrigen Zinksalzlösungen**

Bei der Abscheidung aus dem chemischen Bad kann die Wechselwirkung organischer Moleküle mit anorganischen Phasen zur Bildung komplexer Strukturen führen. [20] Bekannt ist der Zinkfinger, eine Konfiguration eines DNS-bindenden Proteins. [21] Daher wurden bereits viele Komplexe von Zink mit Aminosäuren auf ihre Eignung untersucht, Ausgangsmaterial für die Bildung von festen Materialien zu sein. [22] In diesem Abschnitt wird gezeigt, dass sich Aminosäuren und Dipeptide eignen, um bei der Abscheidung von Zinkverbindungen deren Struktur zu steuern und dass so eine Vielzahl an hierarchisch strukturierten Morphologien erzeugt werden kann. Als Substrate wurden polierte Siliziumeinkristalle verwendet.

Werden der Reaktionslösung Glycyl-Glutamin (Gly-Gn), Citrullin (Cit) oder Prolin (Pro) zugegeben, so bilden sich mikrometergroße, längliche, hexagonale Kristalle. Ähnliche große Kristalle werden sowohl in Lösungen, die Additive mit Carboxylgruppen enthalten, als auch in Lösungen ohne Additive abgeschieden. Gly-Gln, Cit und Pro wechselwirken also nur schwach mit Zinkionen.

In der Gegenwart von ausreichend hohen Konzentrationen von Histidin (His) und Glycyl-Histidin (Gly-His) bilden sich sehr glatte und einheitliche amorphe Schichten. Dicke und Uniformität der Schicht nehmen mit der Konzentration der Hilfsstoffe zu. Messungen mit der Röntgenphotoelektronenspektroskopie (XPS) zeigen für den Fall von Histidin, dass die Schichten aus

ZnO und Zn(His)<sub>2</sub> bestehen, und dass der Anteil an Zn(His)<sub>2</sub> mit steigender His-Konzentration in der Abscheidungslösung zunimmt.

Tryptophyl-Glycin (Trp-Gly) in der Reaktionslösung induziert auf dem Substrat die Bildung komplexer Strukturen von schwammartigem Aussehen und hierarchischem Aufbau. Diese Strukturen ähneln verblüffend den Blattoberflächen von Taro- und Lotuspflanzen [30,31] und zeigen auch deren superhydrophobe Eigenschaften: Wassertropfen perlen ab.

In Gegenwart von Arginin (Arg) bilden sich Stapel von nanometerdicken Plättchen, die an die Schichtstruktur von Perlmutter erinnern. In Lösungen, die Glycyl-Glutaminsäure (Gly-Glu) enthalten, scheiden sich bandförmige Nanostrukturen ab, wenn die Siliziumoberfläche zuvor mit einer Multischicht aus Polyelektrolyten funktionalisiert wurde.

Die Abscheidungsprodukte aus Trp-Gly-, Arg- und Gly-Glu-haltigen Lösungen haben eine komplexe Zusammensetzung, die mittels Röntgenbeugung und Infrarotspektroskopie aufgeklärt wurde. Es handelt sich um sogenannte basische Zink-Schichtsalze mit der Zusammensetzung  $Zn_5(OH)_8A_2 \cdot n H_2O$  oder  $Zn_5(OH)_6(CO_3)_2$ . [32,33,34] Als Komponente A liegen in der Regel Chlorid- oder Nitrationen vor, im vorliegenden Fall nehmen diesen Platz jedoch die Anionen der Aminosäuren ein. Die Schichtsalze haben eine turbostratische Struktur, wobei die Zink- und Hydroxidionen Schichten in Brucitstruktur bilden, die entweder mit Wasser oder einem Teil der Anionen koordiniert sind und zwischen denen sich die übrigen Anionen frei anordnen.

Durch Auslagern bei 450 °C können die verschiedenen Abscheidungsprodukte in Zinkoxid umgewandelt werden; [38] sie behalten dabei ihre charakteristischen Morphologien. Die in Gegenwart von Gly-Glu gewachsenen Bandstrukturen wachsen gerichtet auf. Nach dem Auslagern bestehen sie aus einkristallinem Zinkoxid, dessen  $\langle 001 \rangle$ -Achse senkrecht zur Substratoberfläche orientiert ist. In allen anderen Fällen wurde eine statistische Orientierung des Zinkoxids beobachtet.

Die Schichtsalzstrukturen sind offenbar nach heterogener Keimbildung Ion für Ion aufgewachsen. [16,17] Im Fall von His und Gly-His scheint es jedoch wahrscheinlicher, dass sich durch homogene Keimbildung in der Lösung amorphe Teilchen bilden, die sich dann am Substrat anlagern. [16,25]

### 8.3 Schichtbildung durch orientierte Anlagerung von mit Polyvinylpyrrolidon überzogenen Zinkoxid-Nanokristallen

Bei der Hydrolyse von Zinksalzlösungen fallen normalerweise mikrometergroße, längliche hexagonale Kristalle aus. [49,50,51] Für die Form dieser Kristalle sind Unterschiede in der Oberflächenenergie der verschiedenen Kristallebenen verantwortlich, die zu unterschiedlichen Wachstumsraten entlang der verschiedenen kristallographischen Richtungen führen. [52] In den letzten Jahren konnte jedoch gezeigt werden, dass sich die Größe und das Seitenverhältnis beim Wachstum von Zinkoxidkristallen mittels organischer Hilfsstoffe in der Lösung steuern lassen. [27,54,55, 58,62]

Ziel der Arbeit war es, organische Hilfsstoffe auch bei der Schichtabscheidung einzusetzen, um möglichst glatte, dichte und einheitliche Schichten herstellen zu können. In früheren Arbeiten wurden bereits die Auswirkungen der Zugabe von Aminosäuren und Peptiden [64] sowie Kopolymeren [18] untersucht. In diesem Kapitel wird gezeigt, wie Polyethylenglykol (PEG),  $\beta$ -Cyclodextrin und Polyvinylpyrrolidon (PVP) die Schichtbildung beeinflussen. Als Substrat werden selbstassemblierte Monoschichten (SAM) mit Sulfonsäuregruppen als funktionellen Einheiten [65] verwendet.

In wässrigen Lösungen, denen  $\beta$ -Cyclodextrin zugegeben wurde, scheidet sich keine durchgehende Schicht ab, sondern man erhält nahezu sphärische Aggregate, die sowohl aus rundlichen als auch aus haarförmigen Zinkoxid-Nanokristallen zusammengesetzt sind. Bei höheren Zinksalzkonzentrationen werden in Gegenwart von  $\beta$ -Cyclodextrin Aggregate von mikrometergroßen Plättchen und nadelförmigen Kristallen aus ZnO abgeschieden. In PEG-haltigen methanolischen Lösungen hingegen bilden sich zusammenhängende, aber sehr rauhe nanokristalline Zinkoxidschichten. Die Molmasse des verwendeten PEGs beeinflusst dabei die Schichtmorphologie nur unwesentlich.

Die glattesten und einheitlichsten Schichten entstanden bei der Abscheidung aus einer Zinkacetatlösung in einem Isopropanol-Wasser-Gemisch, dem PVP beigegeben wurde. Die mittlere Schichtdicke beträgt etwa 130 nm nach 4,5 h Abscheidung. Mittels Röntgenbeugung konnte nachgewiesen werden, dass die Schichten aus nanokristallinem Zinkoxid bestehen und keine weiträumige Textur besitzen. Im Transmissionselektronenmikroskop zeigt sich jedoch, dass sich die Schichten aus Domänen zusammensetzen, in denen die Kristallite jeweils gerichtet angeordnet sind. Innerhalb einer Domäne weicht die Orientierung benachbarter Körner nur wenig voneinander ab.

Das Auftreten dieser Domänen wurde mittels des Mechanismus' der gerichteten Aggrega-



tion [66,67] erklärt. Die Trübung der Lösung während der Abscheidung ist ein Hinweis darauf, dass sich die Nanokristalle bereits in der Lösung bilden und dann am Substrat anlagern. Die ersten Kristallite, die am Substrat adsorbieren, nehmen eine beliebige Orientierung an. Später hinzukommende Kristallite orientieren sich parallel zu den an dieser Stelle bereits angelagerten Körnern, und so bilden sich geordnete Domänen aus. Die gerichtete Anlagerung ist durch die polare Kristallstruktur des Zinkits bedingt.

Zusammenfassend wurde festgestellt, dass alle drei überprüften Substanzen als Additive geeignet sind, das anisotrope Wachstum der Zinkoxidkristalle zu hemmen. Als Erklärung hierfür wurde angenommen, dass im Fall von PEG und PVP die dichte Durchdringung der Lösung mit den Polymerketten bzw. im Fall von  $\beta$ -Cyclodextrin [57] (und eventuell auch PVP [69]) die Bildung von Komplexen aus Zinkionen und organischen Molekülen das Kristallwachstum hemmen. Die Abscheidung einigermaßen homogener Schichten gelang jedoch nur in Gegenwart von PVP. Aus dem Nichtvorhandensein von PVP in den Schichten [19] wurde gefolgert, dass die Polymere nur die Kristallisation in Lösung, nicht jedoch die Anlagerung am Substrat steuern.

#### **8.4 Ortsselektive Abscheidung von nanostrukturierten Zinkoxid-Dünnschichten aus polyvinylpyrrolidonhaltigen Lösungen**

Im vorigen Abschnitt wurde die Abscheidung von Zinkoxidschichten in der Gegenwart von PVP in einem Propanol-Wasser-Gemisch vorgestellt. Die Rauigkeit der Schichten war jedoch hoch, ihre Dicke begrenzt, und es bildete sich keine Textur aus. Außerdem sind für optische und elektronische Anwendungen häufig lateral strukturierte Schichten erforderlich. Bei den bislang verbreiteten Ätzprozessen besteht jedoch das Risiko, die Schicht und das Substrat zu beschädigen. Bei früheren Versuchen einer Strukturierung durch ortsselektive Schichtabscheidung gelang es nicht, ZnO-Strukturen abzuscheiden, die gleichzeitig glatt und fluoreszent waren. [88,89,90] In diesem Teil der Arbeit wird eine Methode vorgestellt, wie aus PVP-haltigen Lösungen besonders homogene ZnO-Schichten mit hervorragenden Eigenschaften hergestellt und diese gleichzeitig lateral strukturiert werden können.

Die Schichten werden wiederum auf mit Sulfonsäuregruppen modifizierten SAMs hergestellt, und zwar aus methanolischen Lösungen, die Zinkacetat, PVP mit einer durchschnittlichen Molmasse von 10.000 und als Base Tetraethylammoniumhydroxid (TEAOH) enthalten. Wenn eine solche Lösung auf 60 °C erhitzt wird, bilden sich kolloidale Teilchen, die sich nach und nach am Substrat anlagern. Gleichzeitig beobachtet man die Aggregation der Teilchen in der Lösung,

die mit der Schichtbildung konkurriert. Die Substrate mit den SAMs werden jeweils 1,5 Stunden in der Lösung beschichtet, bevor die gealterte Lösung durch frische ersetzt wird und ein weiterer Abscheidungszyklus durchgeführt wird. Man erhält sehr homogene, nanokristalline und gut haftende Schichten, deren Dicke in etwa linear mit der Anzahl der Abscheidungszyklen um jeweils 10 bis 30 nm zunimmt, während die Rauigkeit (Varianz der Schichtdicke) unter 10 nm liegt und über den gesamten Abscheidungsprozess in etwa konstant bleibt.

Die Schichtdicke hängt außerdem von der PVP-Konzentration ab und erreicht für das Konzentrationsverhältnis  $[PVP] : [Zn^{2+}] \approx 1 : 1$  ein Maximum. In bezug auf die Konzentration der Base ist ein Verhältnis von  $[TEAOH] : [Zn^{2+}] \approx 2,5 : 1$  am günstigsten, und bezüglich der Temperatur ist die Abscheidung umso effektiver, je mehr man sich dem Siedepunkt von Methanol nähert, weshalb für alle weiteren Experimente 60 °C gewählt wurden.

Zinkoxid scheidet sich zwar auf den Sulfonat-SAMs ab, nicht jedoch auf dem blanken Silizium. Dies wird zur Strukturierung der Schichten ausgenutzt, indem man die SAM mittels UV-Licht und einer Fotomaske gezielt an bestimmten Stellen zerstört. [94] Es zeigt sich, dass bei der Schichtabscheidung die belichteten Bereiche tatsächlich ganz frei bleiben, während sich in den abgeschatteten Bereichen eine Schicht wie auf unbelichteten Substraten ausbildet. In einem nur wenige hundert Nanometer breiten Übergangsbereich ist eine erhöhte Rauigkeit der Schicht festzustellen; ansonsten ist die Kante scharf.

Röntgenbeugung und Röntgenphotoelektronenspektroskopie (XPS) beweisen, dass die Schichten aus Zinkoxid bestehen. XPS zeigt außerdem, dass die Oberflächen des Zinkoxids hydroxyliert sind und dass der PVP-Gehalt der Schichten unter der Nachweisgrenze liegt. Röntgenbeugung und hochauflösende Transmissionselektronenmikroskopie ergeben übereinstimmend, dass der mittlere Korndurchmesser um die 6 bis 9 nm liegt.

Wie schon in den Experimenten in Propanol/Wasser [84] wachsen auch im jetzigen Fall die Schichten gerichtet auf. Da Wasser die Hydrolyse beschleunigt, ist die Reaktion in reinem Methanol jedoch nochmals verlangsamt, und schon die ersten adsorbierenden Kristallite haben genug Zeit, sich gegenüber dem Substrat optimal zu orientieren. Daher werden nun nicht mehr nur geordnete Domänen, sondern sogar eine weiträumige Textur beobachtet, die durch Röntgenstrukturanalyse mittels Polfiguren nachgewiesen wurde. Auch für die Ausbildung der Textur erweist sich eine PVP-Konzentration entsprechend  $[PVP] : [Zn^{2+}] \approx 1 : 1$  als optimal.

Wärmebehandlung der Schichten bis 800 °C lässt die Schichten bis auf ein geringfügiges Wachstum der Körner und eine leichte Verstärkung der Textur unverändert, bei noch höheren Temperaturen reagiert das ZnO mit dem Trägermaterial zu Zinksilikaten. [95]

Die Schichten zeigen eine ausgeprägte Photolumineszenz, die sich in drei Komponenten

aufspalten lässt: eine UV-Komponente durch die Bandkantenemission, eine grüne Komponente aufgrund von Sauerstoff-Fehlstellen [98,99] und eine rote von sauerstoffreichen Bereichen. [100] Für sichtbares Licht sind die Schichten durchlässig, für UV-Licht jedoch opak. Der Brechungsindex im sichtbaren Wellenlängenbereich konnte zu 1,6 bestimmt werden, was deutlich niedriger liegt als die 2,0, die an Einkristallen gemessen werden, und auf Porosität hinweist.

Folgender Abscheidungsmechanismus wird vorgeschlagen: Nachdem sich durch die Hydrolyse des Zinkacetats Kristallisationskeime gebildet haben, hemmt das Polymernetzwerk, das die Lösung durchzieht, deren Wachstum. [101] Die Wechselwirkung der stark negativ geladenen SAM-Oberfläche mit den polaren Zinkitkristalliten führt zu orientierter Adsorption der kolloidalen Kristallite. Durch gerichtete Anlagerung wächst die Schicht weiter. Gleichzeitig setzt die Aggregation in der Lösung ein und bringt die Schichtbildung zum Erliegen, da die gesamte zur Anlagerung zur Verfügung stehende Oberfläche der Aggregate bald weit größer ist als die Substratoberfläche. Außerdem führt die Anlagerung einzelner gewachsener Aggregate zu einer Erhöhung der Schichtrauigkeit.

## **8.5 Zeitliche Entwicklung der Bildung von Zinkoxidteilchen und des Aufwachsens orientierter nanokristalliner Schichten in Methanol**

Der Mechanismus, nach dem sich dünne Schichten aus Lösungen abscheiden, war bisher nur wenig untersucht. Man unterscheidet homogene [105] und heterogene [106] Keimbildung, wobei für die Schichtabscheidung meist von homogener Keimbildung ausgegangen wurde. [111] Man stellte sich vor, dass organische Additive an den Keimen adsorbieren und so das Kristallwachstum steuern. [9] Wie sich aus den Teilchen dann eine Schicht auf dem Substrat aufbaut, konnte mit der DLVO-Theorie erklärt werden. [111,112] Tatsächlich kann aber auch Aggregation in der Lösung auftreten und mit der Schichtbildung in Konkurrenz treten. [92,113]

In den letzten Jahren wurde festgestellt, dass viele scheinbar einkristalline Mineralien tatsächlich eine hochgeordnete innere Struktur aufweisen. [114] Es konnte nachgewiesen werden, dass in bestimmten Fällen sich an ein Aggregat anlagernde Teilchen die gleiche kristallographische Orientierung annehmen wie die benachbarten Kristallite. [67,115,84] Dieser Prozess wird als orientierte Aggregation bezeichnet [116] und erklärt den gerichteten Aufbau geordneter Strukturen. Viele Biomineralisationsprozesse laufen außerdem über amorphe Vorstufen ab. [2,114,119]

In diesem Abschnitt wird der Mineralisationsprozeß bei der Abscheidung der im vorigen Abschnitt vorgestellten Zinkoxidschichten genauer untersucht, um eine Erklärung für den

Mechanismus dieses und anderer Abscheidungsverfahren zu finden.

Mittels dynamischer Lichtstreuung wurde die Entwicklung der Teilchengröße in der Lösung während der Reaktion verfolgt. Man kann zwei Phasen erkennen: Während der ersten Phase bleibt der Teilchendurchmesser in etwa konstant. An ihrem Ende sinkt er für kurze Zeit rapide ab, um in der zweiten Phase allmählich linear anzusteigen. Dabei sind die Teilchen in der ersten Phase umso kleiner, je höher die PVP-Konzentration ist. In der zweiten Phase wachsen sie bei höherer PVP-Konzentration schneller.

Wenn die PVP-Konzentration in der Lösung bei etwa 20 Vol.-% oder höher liegt, bilden sich gar keine Teilchen mehr. Ein anderes Verhalten zeigen PVP-freie Lösungen, in denen sich schon beim Anrühren der Lösung bei Raumtemperatur längliche Zinkitkristallite bilden. In Lösungen mit nicht extremen PVP-Konzentrationen entstehen nach dem Erhitzen auf die Abscheidungstemperatur von 60 °C nadelförmige amorphe Teilchen. Die Messung der Ionenleitfähigkeit der Lösung ergibt, dass dies sehr schnell passiert.

Nach einer gewissen Zeit – bei höherer PVP-Konzentration geschieht es umso schneller – lösen sich die amorphen nadelförmigen Teilchen wieder auf. Statt dessen bilden sich nun etwa sphärische Zinkoxid-Nanokristalle, die aggregieren. Bei niedrigen PVP-Konzentrationen haben die Aggregate eine fraktale Form, wie es klassische Modellvorstellungen der Aggregation [131] erwarten lassen. Bei höheren PVP-Konzentrationen sind die Aggregate hingegen kompakt und rundlich. Die Kompaktheit der Aggregate und die lineare Zunahme ihres Durchmessers sind ohne polymerinduzierte Effekte nicht erklärbar. Diese Beobachtungen sprechen dafür, dass die Polymere in der Lösung die Aggregation über entropische Verarmungskräfte fördern. [135,136, 138,139]

Auch wenn PVP mit einem höheren mittleren Molekulargewicht zugegeben wird, durchläuft die Reaktion die gleichen beiden Phasen.

Die thermische und Elementaranalyse ergeben, dass sowohl die amorphen nadelförmigen Teilchen als auch die Aggregate anders als die Schichten auf dem Substrat nicht aus reinem Zinkoxid bestehen, sondern einen PVP-Gehalt von etwa einem Drittel aufweisen.

Elektrophorese und Kernspinresonanzspektroskopie (NMR) zeigen, dass PVP mit den Zinkionen nur schwach und mit den amorphen „Nadeln“ nicht direkt wechselwirkt. Auch deswegen kann ausgeschlossen werden, dass die Polymere das Kristallwachstum steuern, indem sie an den Kristallisationskeimen adsorbieren. PVP beeinflusst den Prozess vielmehr auf andere Weise, indem es in der ersten Phase sowohl die Bildung als auch die Auflösung des Zwischenstands initiiert und in der zweiten Phase die Aggregation fördert.

Um die Beobachtungen in Lösung und auf dem Substrat abzugleichen, wurde auch die Ab-

---

scheidung auf dem Substrat noch weiter untersucht: Aus den PVP-haltigen methanolischen Lösungen scheidet sich Zinkoxid sowohl auf positiv geladenen Oberflächen wie SAMs mit Aminogruppen ab als auch auf negativ geladenen Oberflächen wie SAMs mit Sulfonsäuregruppen oder anionischen Polyelektrolyten. Der Betrag der Oberflächenladung ist entscheidend, nicht ihr Vorzeichen. Außerdem tragen die Teilchen in der Lösung keine nennenswerte Ladung. Diese Beobachtungen lassen darauf schließen, dass die Polarität der Zinkoxidteilchen eine wesentliche Rolle bei der Anlagerung am Substrat spielt.

Die Schichtdicke und die Rauigkeit der Schichten erreichen bei mittleren PVP-Konzentrationen ein Optimum, aber auch die Textur ist dann am ausgeprägtesten. Bei niedrigeren PVP-Konzentrationen lässt die unkontrollierte Ausfällung von Agglomeraten aus der Lösung keine geordnete Schichtbildung zu (bei Konzentrationen nahe null) bzw. der amorphe Zwischenzustand ist zu lang stabil, bei höheren PVP-Konzentrationen hingegen ist die von PVP beschleunigte Aggregation schon wieder zu schnell, für Ordnungsprozesse bleibt keine Zeit und die konkurrierende Aggregation in Lösung nimmt zu bald überhand, bzw. schließlich werden gar keine Teilchen mehr gebildet. Das gleiche Verhalten wird auch mit PVP höheren Molekulargewichts beobachtet, allerdings mit einem vermutlich aufgrund von Entropieeffekten geringfügig (also nicht proportional zur Molmasse) zu höheren Konzentrationen verschobenen Optimum.

Das Schichtwachstum wurde mit einer Quarz-Mikrowaage beobachtet. Während des ersten Abscheidungszyklus' wächst die Schicht nur langsam und nur etwa eine halbe Stunde lang. In den folgenden Abscheidungszyklen verläuft die Massenzunahme wesentlich rascher und dauert etwa drei Stunden lang an.

Zusammenfassend erscheint folgender Mechanismus plausibel: Zinkacetat dissoziiert in Methanol teilweise, und es ist anzunehmen, dass das PVP die Zinkionen solvatisiert. Nach dem Aufheizen der Lösung bewirkt das PVP die Bildung der amorphen nadelförmigen Teilchen. Gleichzeitig löst es sie auch wieder auf, jedoch mit einer deutlich niedrigeren Geschwindigkeitskonstante. Die nun freigesetzten Zinkionen bilden Zinkoxid-Nanokristalle, die unter dem Einfluss der vom PVP induzierten Verarmungskräfte sich am Substrat anlagern bzw. in Lösung aggregieren. Zunächst wird wegen der niedrigeren Energiebarriere vor allem Schichtbildung stattfinden, später wegen der größeren Oberfläche vor allem Aggregation in Lösung. Die Mineralisation über einen amorphen Übergangszustand ist in der Biomineralisation ein bekanntes Phänomen; [2] nun wurde sie erstmals bei der künstlichen Synthese mittels Abscheidung im chemischen Bad beobachtet.

## 8.6 Nach einer bioinspirierten Methode hergestellte Zinkoxid-Mikrokapseln

Zinkoxidhohlkugeln zeigen Materialeigenschaften, die sich von massivem Zinkoxid unterscheiden. [149] Ihre große Oberfläche macht eine Anwendung als Gassensoren [151] oder Katalysatoren [152] denkbar. Bisherige Methoden zur Herstellung von Zinkoxidhohlkugeln erforderten hohe Energien, und man hatte kaum Einfluss auf Form, Größe und Qualität des Produkts. [153,154,155,156,157]

Eine bessere Steuerung erlauben Methoden, die sich „verlorener Kerne“ bedienen. Das bedeutet, dass Zinkoxidschichten auf Kugeln aus einem Trägermaterial hergestellt werden und das Trägermaterial anschließend mit chemischen oder thermischen Mitteln zersetzt wird. Als Kerne wurden früher schon Kugeln aus  $\text{Zn}_5(\text{CO}_3)_2(\text{OH})_6$  [159] oder aus durch Ionenaustausch mit  $\text{Zn}^{2+}$ -Ionen versehenem Polystyrol (PS) [161] verwendet. Einfacher und kostengünstiger ist jedoch die Verwendung von kommerziell erhältlichen PS-Mikrokugeln mit sulfonatmodifizierten Oberflächen in Verbindung mit der in den vorausgegangenen Abschnitten entwickelten ZnO-Abscheidungsmethode. Damit ist sichergestellt, dass die Mikrokapseln gute und kontrollierbare Eigenschaften aufweisen. Günstig wirkt sich auch aus, dass die Abscheidung von Zinkoxid in der Gegenwart von PVP auf Sulfonatoberflächen bei niedrigen Temperaturen und ohne großen Energieaufwand möglich ist.

Die als wässrige Suspension gekauften PS-Mikrokugeln werden in Methanol gewaschen, in eine Abscheidungslösung transferiert, dort 1,5 Stunden lang beschichtet, abzentrifugiert und jeweils in frischer Abscheidungslösung wieder redispergiert, um in weiteren Abscheidungszyklen eine dichte und ausreichend dicke ZnO-Schale zu erzeugen. Um den PS-Kern zu entfernen, werden die beschichteten Kugeln in Chloroform dispergiert, in dem sich Polystyrol auflöst, oder er wird im Ofen bei 450 °C thermisch zersetzt.

Röntgenbeugungsexperimente zeigen, dass die Zinkoxidschalen wie die Schichten auf ebenen Substraten aus nanokristallinem Zinkoxid bestehen. In Aufnahmen aus dem Rasterelektronenmikroskop ist zu erkennen, dass die Oberfläche der Mikrokugeln durchgehend bedeckt ist, die Rauigkeit der ZnO-Schichten jedoch höher ist als auf ebenen Sulfonat-SAMs. Ein fokussierter Ionenstrahl wurde verwendet, um Querschnitte der beschichteten Kugeln zu präparieren. Dadurch bestätigt sich, dass ein kugelförmiger PS-Kern mit einer weitgehend homogenen Zinkoxidschicht überzogen ist. Auch die ZnO-Wanddicke kann bestimmt werden; sie beträgt nach zehn Abscheidungszyklen etwa 160 nm. Es ist zu erwarten, dass sie sich variieren lässt, indem eine andere Anzahl an Abscheidungszyklen gewählt wird. [127]

Nach der Behandlung mit Chloroform bzw. Hitze sehen die Zinkoxidschalen äußerlich unverändert aus. Wird allerdings mit dem Ionenstrahl ein Querschnitt präpariert, kann man ungehindert auf die innere Oberfläche der Zinkoxidschicht bzw. durch den freigelegten Hohlraum hindurchblicken. Nach einer Stunde in Chloroform bzw. im Ofen wurden in einigen Hohlkugeln noch PS-Reste vorgefunden, die durch eine längere Behandlung jedoch sicher hätten entfernt werden können. Wichtig ist die Beobachtung, dass nahezu alle Zinkoxidschalen die Zersetzung des PS-Kerns unversehrt überstanden, denn sie ist ein Nachweis für die außerordentliche mechanische Stabilität der Schichten. Außerdem weist das ungehinderte Entweichen des Polystyrols auf Porosität im Zinkoxid hin.

Mit der vorgestellten Methode konnten mit minimalen Kosten und relativ geringem technischem Aufwand Zinkoxidhohlkugeln von herausragender Qualität hergestellt werden. Kraftspektroskopie [163] an solchen Hohlkugeln könnte zur Messung der mechanischen Kenngrößen des synthetisierten Zinkoxids verwendet werden, da Substrateinflüsse ausgeschlossen wären.

## **8.7      Laminate aus Zinkoxid- und Polyaminosäurenschichten mit verbesserten mechanischen Eigenschaften**

Perlmutter besteht zwar zu 95 % aus Kalziumkarbonat, ist aber 3000 mal so zäh [164,165] und etwa doppelt so hart [166,167] wie das monolithische Mineral. Man führt das auf die Kombination aus weichem organischen und hartem anorganischen Material [171,172] und auf die Schichtstruktur [173] von Perlmutter zurück. Um die Vorteile dieser Struktur technisch nutzbar zu machen, wurden zahllose Versuche unternommen, synthetisches Perlmutter herzustellen, [174] aber auch organisch-anorganische Schichtstrukturen mit anderen anorganischen Komponenten wie Silikat, [175] Aluminiumoxid, [176] Titanoxid [177] und Indium-Zinn-Oxid [178] herzustellen, wurde versucht.

Jüngst wurde von Kompositstrukturen aus gestapelten Schichten von abwechselnd amorphem Titanoxid und Polyelektrolyten berichtet. [179] Tatsächlich wurde an diesen Verbundwerkstoffen eine höhere Härte und ein höherer Elastizitätsmodul gemessen als am entsprechenden reinen Titanoxid. Inzwischen konnte gezeigt werden, dass dabei auch die Bruchzähigkeit substantiell ansteigt. [193] Ein ähnlicher Ansatz wurde nun verfolgt, um Laminate aus Zinkoxid abwechselnd mit organischen Zwischenschichten herzustellen.

Da die zum Aufbau von Polyelektrolyt-Multischichten üblicherweise verwendeten synthetischen Polykationen Zinkoxid auflösen, wurde auf ein System aus Polyaminosäuren, nämlich

Polyglutaminsäure (PLGS) im Wechsel mit Polylysin (PLL), ausgewichen. Da jedoch für die Abscheidung von Zinkoxid eine hohe Oberflächenladung von Vorteil ist, wurde als gegen das Zinkoxid abschließende Lage jeweils noch eine Schicht Polystyrolsulfonat (PSS) aufgebracht. Als anorganisches Material wurde nach der in den vorangegangenen Abschnitten beschriebenen Methode aus PVP-haltigen methanolischen Lösungen Zinkoxid abgeschieden. [127]

Im Rasterelektronenmikroskop ist die Schichtstruktur der Komposite deutlich zu erkennen. Die Zinkoxidschichten sind etwa 120 nm dick, die Polyaminosäurenschichten wesentlich dünner. Die Gesamtdicke der Schichtstapel ist knapp 20 % geringer als die Dicke von monolithischen ZnO-Schichten, die mit gleich vielen Abscheidungszyklen hergestellt wurden. Das deutet auf eine geringfügige Löslichkeit des Zinkoxids in der PLL-Lösung hin.

In der Röntgenbeugung ist kein nennenswerter Unterschied erkennbar zwischen den Kompositen und monolithischem Zinkoxid, [182] und es spielt auch keine Rolle, ob sich zwischen dem Substrat und der untersten Lage ZnO eine SAM oder eine Polyaminosäurenschicht befindet. Die mittlere Korngröße beträgt wieder etwa 7 nm, und die charakteristische Textur bildet sich trotz der organischen Zwischenschichten aus.

Mittels Rasterkraftmikroskopie (AFM) konnte kein erkennbarer Einfluss der organischen Zwischenschichten auf die Rauigkeit der Schichtoberfläche festgestellt werden. Mit AFM wurde auch ein Höhenprofil einer teilweise abgeschabten Polyelektrolytschicht auf einem Siliziumkristall gemessen. Aus den Messwerten folgt, dass die Polyaminosäurenzwischenschichten nur etwa 9 nm dick sind. Die erste Schicht zwischen dem Silizium und der untersten Zinkoxidschicht wurde mit 15 nm etwas dicker gewählt.

Um die Zusammensetzung der Kompositschichten zu untersuchen, wurden mit der Augerelektronenspektroskopie Tiefenprofile aufgenommen. In zunehmender Tiefe finden sich abwechselnd Bereiche, in denen ein erhöhtes Sauerstoff- bzw. ein erhöhtes Kohlenstoff- und Schwefelsignal gemessen wird. Insbesondere die deutliche Variation des Schwefelsignals ist ein Nachweis für den Einbau von organischen Zwischenschichten ins Zinkoxid, da die Zinkoxid-Abscheidungslösung keine schwefelhaltigen Verbindungen enthält.

Die mechanischen Eigenschaften der Schichten wurden per Nanoindentation vermessen. Gegenüber dem entsprechenden monolithischen Zinkoxid ist die Härte (2,1 GPa statt 1,7 GPa) erhöht, der während Elastizitätsmodul (ca. 35 bis 40 GPa) in etwa gleichauf liegt. Die Werte von einkristallinem Zinkoxid [190] werden zwar nicht erreicht, was auf die Polykristallinität und Porosität der Schicht zurückzuführen ist, das mechanische Verhalten ist jedoch ähnlich gut wie bei wesentlich aufwendiger über die Gasphase hergestelltem nanokristallinem Zinkoxid. [191] Die Härtung der Kompositschichten gegenüber monolithischen Schichten kann erklärt werden durch



die Kombination der anorganischen Phase mit einem hohen und der organischen Phase mit einem sehr geringen Schubmodul. Dadurch werden Verformungsvorgänge über die Grenzflächen hinaus unterbunden.

Dank der kristallinen Struktur des Zinkoxids ist der Härtungseffekt sogar noch deutlich größer als bei dem zuvor untersuchten amorphen Titanoxid. [179] Für die Zukunft wäre die Bestimmung der Bruchzähigkeit der Schichten eine interessante Fragestellung, die beispielsweise mit Zugversuchen an vom Substrat gelösten Schichten [142] geklärt werden könnte.



## References

- [1] K. L. Chopra, S. Major, D. K. Pandya, *Thin Solid Films* **1983**, *102*, 1.
- [2] S. Mann, *Chem. uns. Zeit* **1986**, *20*, 69.
- [3] R. Kniep, *Chem. uns. Zeit* **1996**, *30*, 46.
- [4] S. W. Wise, *Science* **1970**, *167*, 1486.
- [5] A. H. Heuer, D. J. Fink, V. J. Laraia, J. L. Arias, P. D. Calvert, K. Kendall, G. L. Messing, J. Blackwell, P. C. Rieke, D. H. Thompson, A. P. Wheeler, A. Veis, E. I. Kaplan, *Science* **1992**, *255*, 1098.
- [6] S. Mann, *Nature* **1993**, *365*, 499.
- [7] X. Y. Liu, S. W. Lim, *J. Am. Chem. Soc.* **2003**, *125*, 888.
- [8] Y. Gao, K. Koumoto, *Crystal Growth & Design* **2005**, *5*, 1983.
- [9] R. C. Hoffmann, J. Bill, F. Aldinger, *Key Eng. Mater.* **2004**, *264-268*, 331.
- [10] S. Mokrushin, Y. D. Tkachev, *Kolloidnyi Zhurnal* **1961**, *23*, 438.
- [11] R. A. Boudreau, R. D. Rauh, *J. Electrochem. Soc.* **1986**, *130*, 513.
- [12] T. Saeed, P. O'Brien, *Thin Solid Films* **1995**, *271*, 35.
- [13] T. M. Fuchs, *Templatinduzierte Erzeugung und Charakterisierung dünner ZnO- und TiO<sub>2</sub>-Schichten*, Dissertation, Universität Stuttgart, Stuttgart **2003**.
- [14] S. J. Pearton, D. P. Norton, K. Ip, Y. W. Heo, T. Steiner, *Superlatt. Microstruct.* **2003**, *34*, 3.
- [15] Z. L. Wang, *J. Phys. Condens. Matter* **2004**, *16*, R829.
- [16] J. Bill, R. C. Hoffmann, T. M. Fuchs, F. Aldinger, *Z. Metallkd.* **2002**, *93*, 478.
- [17] R. C. Hoffmann, S. Jia, J. Bill, M. R. de Guire, F. Aldinger, *J. Ceram. Soc. Jap.* **2004**, *112-1*, S1089.
- [18] R. C. Hoffmann, S. Jia, J. C. Bartolomé, T. M. Fuchs, J. Bill, P. C. J. Graat, F. Aldinger, *J. Eur. Ceram. Soc.* **2003**, *23*, 2119.
- [19] R. C. Hoffmann, S. Jia, L. P. H. Jeurgens, J. Bill, F. Aldinger, *Mater. Sci. Eng. C* **2006**, *26*, 41.
- [20] see e. g. S. Mann, *Biomineralization*, Oxford University Press, Oxford **2001**.
- [21] see e. g. S. J. Lippard, J. M. Berg, *Principles of Bioinorganic Chemistry*, University Science Books, Mill Valley **1994**, pp. 178 – 183.
- [22] M. Rombach, M. Gelinsky, H. Vahrenkamp, *Inorg. Chim. Acta* **2002**, *334*, 25.
- [23] G. Decher, *Science* **1997**, *277*, 1232.

- 
- [24] G. Weitzel, F. Schneider, A. Frentzdorff, H. Z. Heyke, *Physiol. Chem.* **1957**, *307*, 14.
- [25] R. C. Hoffmann, L. P. H. Jeurgens, S. Wildhack, J. Bill, F. Aldinger, *Chem. Mater.* **2004**, *16*, 4199.
- [26] C. D. Wagner, W. M. Riggs, L. E. Davis, J. F. Moulder, G. E. Muilenberg, *Handbook of X-ray Photoelectron Spectroscopy*, Perkin-Elmer cooperation – Physical Electronics Division, Eden Prairy **1979**.
- [27] M. Öner, J. Norwig, W. H. Meyer, G. Wegner, *Chem. Mater.* **1998**, *10*, 460.
- [28] T. J. Kistenmacher, *Acta Crystallogr. B* **1972**, *28*, 1302.
- [29] L. G. Mar, P. Y. Timbrell, R. N. Lamb, *Thin Solid Films* **1993**, *223*, 341.
- [30] W. Barthlott, C. Neinhuis, *Planta* **1997**, *202*, 1.
- [31] N. A. Patankar, *Langmuir* **2004**, *20*, 8209.
- [32] R. Z. Allmann, *Kristallogr.* **1968**, *126*, 417.
- [33] W. Stählin, H. R. Oswald, *Acta Crystallogr.* **1970**, *B26*, 860.
- [34] S. Ghose, *Acta Crystallogr.* **1964**, *17*, 1051.
- [35] L. Poul, N. Jouini, F. Fiévet, *Chem. Mater.* **2000**, *12*, 3123.
- [36] J. Zhang, F. Zhang, L. Ren, D. G. Evans, X. Duan, *Mater. Chem. Phys.* **2004**, *85*, 207.
- [37] D. Yang, R. F. Frindt, *J. Mater. Res.* **1996**, *11*, 1733.
- [38] E. Hosono, S. Fujihara, T. Kimura, H. Imai, *J. Colloid Interface Sci.* **2004**, *272*, 391.
- [39] S. Aisawa, S. Takahashi, W. Ogasawara, Y. Umetsu, E. Narita, *J. Solid State Chem.* **2001**, *162*, 52.
- [40] T. Hibino, *Chem. Mater.* **2004**, *16*, 5482.
- [41] S. P. Newman, T. Di Cristina, P. V. Coveney, W. Jones, *Langmuir* **2002**, *18*, 2933.
- [42] H. Morioka, H. Tagaya, J. I. Kadokawa, K. Chiba, *J. Mater. Sci. Lett.* **1999**, *18*, 995.
- [43] Figure 2.12 and the corresponding paragraphs in the text are not part of the original paper, but they were taken from P. Gerstel, P. Lipowsky, O. Durupthy, R. C. Hoffmann, P. Bellina, F. Aldinger, *J. Ceram. Soc. Jap.* **2006**, *114*, 911.
- [44] M. Yoshimura, J. Livage, *MRS Bulletin* **2000**, *25*, 12.
- [45] T. P. Niesen, M. R. De Guire, *J. Electroceram.* **2001**, *6*, 169.
- [46] T. P. Niesen, M. R. De Guire, *Solid State Ionics* **2002**, *151*, 61.
- [47] N. R. Pavaskar, C. A. Menezes, A. P. B. Sinha, *J. Electroceram. Soc.* **1977**, *124*, 743.
- [48] M. Ristov, G. J. Sinadinovski, I. Grozdanov, M. Mitreski, *Thin Solid Films* **1987**, *149*, 65.
- [49] D. S. Boyle, K. Govender, P. O'Brien, *Chem. Comm.* **2002**, –, 80.

- 
- [50] S. Yamabi, H. Imai, *J. Mater. Chem.* **2002**, *12*, 3773.
- [51] R. Turgeman, O. Gershevitz, O. Palchik, M. Deutsch, B. M. Ocko, A. Gedanken, C. N. Sukenik, *Crystal Growth & Design* **2004**, *4*, 169.
- [52] R. F. Sekerka, *Cryst. Res. Technol.* **2005**, *40*, 291.
- [53] E. Matijevic, *Acc. Chem. Res.* **1981**, *14*, 22.
- [54] P. O'Brien, T. Saeed, J. Knowles, *J. Mater. Chem.* **1996**, *6*, 1135.
- [55] A. Taubert, G. Glasser, D. Palms, *Langmuir* **2002**, *18*, 4488.
- [56] A. Taubert, D. Palms, O. Weiss, M. T. Piccini, D. N. Batchelder, *Chem. Mater.* **2002**, *14*, 2594.
- [57] Y. Yang, X. F. Li, J. B. Chen, H. L. Chen, X. M. Bao, *Chem. Phys. Lett.* **2003**, *373*, 22.
- [58] C. L. Yang, J. N. Wang, W. K. Ge, L. Guo, S. H. Yang, D. Z. Shen, *J. Appl. Phys.* **2001**, *90*, 4489.
- [59] L. Guo, S. H. Yang, C. L. Yang, P. Yu, J. N. Wang, W. K. Ge, G. K. L. Wong, *Appl. Phys. Lett.* **2000**, *76*, 2901.
- [60] L. Guo, S. H. Yang, C. L. Yang, P. Yu, J. N. Wang, W. K. Ge, G. K. L. Wong, *Chem. Mater.* **2000**, *12*, 2268.
- [61] L. Guo, J. X. Cheng, X. Y. Li, Y. J. Yan, S. H. Yang, C. L. Yang, J. N. Wang, W. K. Ge, *Mater. Sci. Eng. C* **2001**, *16*, 123.
- [62] Z. Q. Li, Y. J. Xiong, Y. Xie, *Inorg. Chem.* **2003**, *42*, 8105.
- [63] J. Bill, P. Gerstel, R. C. Hoffmann, L. P. H. Jeurgens, P. Lipowsky, S. Wildhack, F. Aldinger, *Mater. Res. Soc. Symp. Proc.* **2005**, *873E*, K5.3.
- [64] P. Gerstel, R. C. Hoffmann, P. Lipowsky, L. P. H. Jeurgens, J. Bill, F. Aldinger, *Chem. Mater.* **2006**, *18*, 179 (Chapter 2 of this work).
- [65] R. J. Collins, C. N. Sukenik, *Langmuir* **1995**, *11*, 2322.
- [66] J. F. Banfield, S. A. Welch, H. Z. Zhang, T. T. Ebert, R. L. Penn, *Science* **2000**, *289*, 751.
- [67] C. Pacholski, A. Kornowski, H. Weller, *Angew. Chem. Int. Ed.* **2002**, *41*, 1188.
- [68] G. Trejo, R. Ortega, Y. Meas, *Plating and Surface Finishing* **2002**, *89*, 84.
- [69] Y. Zhang, G. H. Yang, X. X. Li, W. Luo, M. Y. Huang, Y. Y. Jiang, *Polym. Adv. Technol.* **1999**, *10*, 108.
- [70] Figure 3.7 and the corresponding paragraph in the text are not part of the original paper, but they were taken from [19]. The experiments were conducted by P. Lipowsky.
- [71] D.W. Bahnemann, C. Kormann, M. R. Hoffmann, *J. Phys. Chem.* **1987**, *91*, 3789.

- 
- [72] K. Morimoto, in: *Phosphor Handbook* (ed. S. Shionoya, W.M. Yen), CRC Press, Boca Raton **1998**, pp. 561 – 580.
- [73] Y. Nakanishi, A. Miyake, H. Kominami, T. Aoki, Y. Hatanaka, G. Shimaoka, *Appl. Surf. Sci.* **1999**, *142*, 233.
- [74] T. Minami, M. Tanigawa, M. Yamanishi, T. Kawamura, *Japan. J. Appl. Phys.* **1974**, *13*, 1475.
- [75] D. M. Bagnall, C. F. Chen, Z. Zhu, T. Yao, S. Koyama, M. Y. Shen, T. Goto, *Appl. Phys. Lett.* **1997**, *70*, 2230.
- [76] H. E. Brown, *Zinc oxide. Properties and Applications*, International Lead Zinc Research Organization, New York **1976**, pp. 26 – 32.
- [77] *Elektronik Industrie* **1974**, *5*, 8.
- [78] L. M. Levinson, H. R. Philipp, *Appl. Phys. Lett.* **1974**, *24*, 75.
- [79] N. F. Foster, G. A. Rozgonyi, *Appl. Phys. Lett.* **1966**, *8*, 221.
- [80] T. Nakazawa, K. Ito, *J. Vac. Soc. Japan* **1983**, *26*, 889.
- [81] H. E. Brown, *Zinc oxide. Properties and Applications*, International Lead Zinc Research Organization, New York **1976**, pp. 10 – 12.
- [82] Ü. Özgür, Ya. I. Alivov, C. Liu, A. Teke, M. A. Reshchikov, S. Doğan, V. Avrutin, S.-J. Cho, H. Morkoç, *J. Appl. Phys.* **2005**, *98*, 41301.
- [83] T. Andelman, Y. Gong, M. Polking, M. Yin, I. Kuskovsky, G. Neumark, S. O'Brien, *J. Phys. Chem. B* **2005**, *109*, 14314.
- [84] P. Lipowsky, S. Jia, R. C. Hoffmann, N. Y. Jin-Phillipp, J. Bill, M. Rühle, *Int. J. Mat. Res.* **2006**, *97*, 607 (Chapter 3 of this work).
- [85] T. Hirano, H. Kozuka, *J. Mat. Sci.* **2003**, *38*, 4203.
- [86] T. Du, O. J. Ilegbusi, *J. Mat. Sci.* **2004**, *39*, 6105.
- [87] Y. Masuda, T. Sugiyama, H. Lin, W. S. Seo, K. Koumoto, *Thin Solid Films* **2001**, *382*, 153.
- [88] G. H. Lee, Y. Yamamoto, M. Kourog, M. Ohtsu, *Thin Solid Films* **2001**, *386*, 117.
- [89] N. Saito, H. Haneda, T. Sekiguchi, N. Ohashi, I. Sakaguchi, K. Koumoto, *Adv. Mater.* **2002**, *14*, 418.
- [90] Y. Masuda, N. Kinoshita, F. Sato, K. Koumoto, *Crystal Growth & Design* **2006**, *6*, 75.
- [91] P. H. F. Hansen, M. Malmsten, B. Bergenståhl, L. Bergström, *J. Colloid Interface Sci.* **1999**, *220*, 269.
- [92] H. Okudera, Y. Yokogawa, *Thin Solid Films* **2001**, *401*, 124.

- 
- [93] J. E. Rodríguez-Paéz, A. C. Caballero, M. Villegas, C. Moure, P. Durán, J. F. Fernández, *J. Europ. Ceram. Soc.*, **2001**, *21*, 925.
- [94] C. S. Dulcey, J. H. Georger, V. Krauthamer, D. A. Stenger, T. L. Fare, J. M. Calvert, *Science* 1991, *252*, 551.
- [95] Z. G. Ji, S. C. Zhao, Y. Xiang, Y. L. Song, Z. Z. Ye, *Chinese Physics* **2004**, *13*, 561.
- [96] S. A. Studenikin, N. Golego, M. Cocivera, *J. Appl. Phys.* **1998**, *84*, 2287
- [97] J. J. Wu, S. C. Liu, *J. Phys. Chem. B* **2002**, *106*, 9546.
- [98] K. Vanheusden, W. L. Warren, C. H. Seager, D. R. Tallant, J. A. Voigt, B. E. Gnade, *J. Appl. Phys.* **1996**, *79*, 7983.
- [99] K. Vanheusden, C. H. Seager, W. L. Warren, D. R. Tallant, J. Caruso, M. J. Hampden-Smith, T. T. Kodas, *J. Lumin.* **1997**, *75*, 11.
- [100] A. B. Djurišić, Y. H. Leung, K. H. Tam, *Appl. Phys. Lett.* **2006**, *88*, 103107.
- [101] G. Strobl, G. *The Physics of Polymers*, 2nd ed., Springer Verlag, Berlin **1997**, pp. 64 – 82.
- [102] N. Balachander, C. N. Sukeinik, *Langmuir* **1990**, *6*, 1621.
- [103] A. Strecker, U. Bader, M. Kelsch, U. Salzberger, M. Sycha, M. Gao, G. Richter, K. van Benthem, *Z. Metallkd.* **2003**, *94*, 290.
- [104] J. Rieger, J. Thieme, C. Schmidt, *Langmuir* **2000**, *16*, 8300.
- [105] R. Becker, W. Döring, *Annalen der Physik* **1935**, *24*, 719.
- [106] D. Turnbull, *J. Chem. Phys.* **1950**, *18*, 198.
- [107] A. Mersmann, K. Bartosch, B. Braun, A. Eble, C. Heyer, *Chem. Ing. Tech.* **2000**, *72*, 17.
- [108] J. Rieger, E. Hädicke, I. U. Rau, D. Boeckh, *Tenside Surf. Det.* **1997**, *34*, 430.
- [109] E. Hädicke, J. Rieger, I. U. Rau, D. Boeckh, *Phys. Chem. Chem. Phys.* **1999**, *1*, 3891.
- [110] T. L. Sounart, J. Liu, J. A. Voigt, J. W. P. Hsu, E. D. Spoeke, Z. (R.) Tian, Y. Jiang, *Adv. Funct. Mater.* **2006**, *16*, 335.
- [111] H. Shin, M. Agarwal, M. R. de Guire, A. H. Heuer, *Acta mater.* **1998**, *46*, 801.
- [112] T. P. Niesen, M. R. de Guire, J. Bill, F. Aldinger, M. Rühle, A. Fischer, F. C. Jentoft, R. Schlögl, *J. Mater. Res.* **1999**, *14*, 2464.
- [113] H. Cölfen, H. Schnablegger, A. Fischer, F. C. Jentoft, G. Weinberg, R. Schlögl, *Langmuir* **2002**, *18*, 3500.
- [114] H. Cölfen, S. Mann, *Angew. Chem.* **2003**, *115*, 2452.
- [115] R. L. Penn, J. L. Banfield, *Science* **1998**, *281*, 969.
- [116] A. P. Alivisatos, *Science* **2000**, *289*, 736.

- 
- [117] M. Yeadon, M. Ghaly, J. C. Yang, R. S. Averback, J. M. Gibson, *Appl. Phys. Lett.* **1998**, *73*, 3208.
- [118] H. Cölfen, M. Antonietti, *Angew. Chem.* **2005**, *117*, 5714.
- [119] S. Weiner, I. Sagi, L. Addadi, *Science* **2005**, *309*, 1027.
- [120] E. Beniash, J. Aizenberg, L. Addadi, S. Weiner, *Proc. R. Soc. Lond. B* **1997**, *264*, 461.
- [121] Y. Politi, T. Arad, E. Klein, S. Weiner, L. Addadi, *Science* **2004**, *306*, 1161.
- [122] I. M. Weiss, N. Tuross, L. Addadi, S. Weiner, *J. Exp. Zool.* **2002**, *293*, 478.
- [123] J. C. Marxen, W. Becker, D. Finke. B. Hasse, M. Epple, *J. Moll. Stud.* **2003**, *69*, 113.
- [124] R. Dillaman, S. Hequembourg, M. Gay, *J. Morphol.* **2005**, *263*, 356.
- [125] K. M. Towe, H. A. Lowenstam, *J. Ultrastruct. Res.* **1967**, *17*, 1.
- [126] H. A. Lowenstam, S. Weiner, *Science* **1985**, *227*, 51.
- [127] P. Lipowsky, R. C. Hoffmann, U. Welzel, J. Bill, F. Aldinger, *Adv. Funct. Mater.* **2007**, *17*, 2151 (Chapter 4 of this work).
- [128] In solutions containing 10 mmol·l<sup>-1</sup> zinc acetate and PVP with a molecular weight of 10 000 g·mol<sup>-1</sup>, the volume fraction of PVP roughly equals one tenth of the quotient of the polymer concentration over the concentration of zinc acetate. Therefore the PVP volume fraction and the ratio [PVP] : [Zn<sup>2+</sup>] are used equivalently here.
- [129] In order to avoid confusion of the two different types of particles, the elongated crystalline particles in PVP-free solutions are called “rod-like”, and the amorphous particles in PVP-containing solutions are called “spicular” or “needle-like”, although their shape is very similar.
- [130] Since the usual deposition solutions were too dilute for <sup>13</sup>C NMR spectroscopic studies, the following concentrations were used: [PVP] = 10 mM, [Zn<sup>2+</sup>] = 470 mM, [TEAOH] = 150 mM, resulting in the formation of amorphous spicular particles at room temperature according to observations using the TEM. This means that this highly concentrated solution is comparable to standard solutions in the regime of “low” polymer concentrations.
- [131] D. A. Weitz, M. Oliveria, *Phys. Rev. Lett.* **1984**, *52*, 1433.
- [132] R. C. Ball, D. A. Weitz, T. A. Witten, F. Leyvraz, *Phys. Rev. Lett.* **1987**, *58*, 274.
- [133] M. Y. Lin, H. M. Lindsay, D. A. Weitz, R. C. Ball, R. Klein, P. Meakin, *Phys. Rev. A* **1990**, *41*, 2005.
- [134] D. A. Weitz, J. S. Huang, M. Y. Lin, J. Sung, *Phys. Rev. Lett.* **1984**, *53*, 1657.



- 
- [135] M. J. Snwoden, S. M. Clegg, P. A. Williams, *J. Chem. Soc. Faraday Trans.* **1991**, *87*, 2201.
- [136] M. Fuchs, K. S. Schweizer, *J. Phys. Cond. Mat.* **2002**, *14*, R239.
- [137] R. Tuinier, J. Rieger, C. G. de Kruif, *Adv. Colloid Interface Sci.* **2003**, *103*, 1.
- [138] J. C. Kim, K. H. Auh, *Modelling Simul. Mater. Sci. Eng.* **1999**, *7*, 447.
- [139] W. C. K. Poon, *J. Phys. Cond. Mat.* **2002**, *14*, R859.
- [140] V. J. Anderson, E. H. A. de Hoog, H. N. W. Lekkerkerker, *Phys. Rev. E* **2001**, *65*, 011403.
- [141] M. D. Haw, M. Sievwright, W. C. K. Poon, P. N. Pusey, *Adv. Colloid Interface Sci.* **1995**, *62*, 1.
- [142] P. Lipowsky, M. Hirscher, R. C. Hoffmann, J. Bill, F. Aldinger, *Nanotechnology* **2007**, *18*, 165603 (Chapter 6 of this work).
- [143] P. Lipowsky, Ž. Burghard, L. P. H. Jeurgens, J. Bill, F. Aldinger, **2007**, *18*, 345707 (Chapter 7 of this work).
- [144] See Chapter 5.1.
- [145] S. Akhter, K. Lui, H. H. Kung, *J. Phys. Chem.* **1985**, *89*, 1958.
- [146] N. Patel, S. A. Egorov, *J. Chem. Phys.* **2005**, *123*, 144916.
- [147] R. I. Cukier, *Macromolecules* **1984**, *17*, 252.
- [148] L. Masaro, X. X. Zhu, *Prog. Polym. Sci.* **1999**, *24*, 731.
- [149] S. Oldenburg, G. Hale, J. Jackson, N. Halas, *Appl. Phys. Lett.* **1999**, *75*, 1063.
- [150] G. B. Sukhorukov, A. Fery, M. Brumen, H. Möhwald, *Phys. Chem. Chem. Phys.* **2004**, *6*, 4078.
- [151] D. J. Leary, J. O. Barnes, A. G. Jordan, *J. Electrochem. Soc.* **1982**, *129*, 1382.
- [152] J. B. L. Martins, E. Longo, C. A. Taft, *Int. J. Quant. Chem.* **1998**, *70*, 367.
- [153] H. J. Fan, R. Scholz, F. M. Kolb, M. Zacharias, U. Gösele, *Solid State Comm.* **2004**, *130*, 517.
- [154] Y. H. Leung, K. H. Tam, A. B. Djurišić, M. H. Xie, W. K. Chan, D. Lu, W. K. Ge, *J. Crystal Growth* **2005**, *283*, 134.
- [155] Z. Y. Jiang, Z. X. Xie, X. H. Zhang, S. C. Lin, T. Xu, S. Y. Xie, R. B. Huang, L. S. Zheng, *Adv. Mater.* **2004**, *16*, 904.
- [156] S. Ravindran, G. T. S Andavan, C. Ozkan, *Nanotechnology* **2006**, *17*, 723.
- [157] J. Duan, X. Huang, E. Wang, H. Ai, *Nanotechnology* **2006**, *17*, 1786.
- [158] Y. He, *Mater. Lett.* **2005**, *59*, 114.

- 
- [159] C. Yan, D. Xue, *J. Phys. Chem. B* **2006**, *110*, 7102.
- [160] C. Yan, D. Xue, *J. Phys. Chem. B* **2006**, *110*, 11076.
- [161] M. C. Neves, T. Trindade, A. M. B. Timmons, J. D. Pedrosa de Jesus, *Mat. Res. Bull.* **2001**, *36*, 1099.
- [162] Y. Wang, S. Supothina, M. R. De Guire, A. H. Heuer, R. Collins, C. N. Sukenik, *Chem. Mater.* **1998**, *10*, 2135.
- [163] H.-J. Butt, B. Cappella, M. Kappl, *Surf. Sci. Rep.* **2005**, *59*, 1.
- [164] J. D. Currey, *Proc. R. Soc. Lond. B* **1977**, *196*, 443.
- [165] A. P. Jackson, J. F. V. Vincent, R. M. Turner, *Proc. R. Soc. Lond. B* **1988**, *234*, 415.
- [166] F. Barthelat, C.-M. Li, C. Comi, H. D. Espinosa, *J. Mater. Res.* **2006**, *21*, 1977.
- [167] K. S. Katti, B. Mohanty, D. R. Katti, *J. Mater. Res.* **2006**, *21*, 1237.
- [168] S. W. Wise jr., *Science* **1970**, *167*, 1486.
- [169] B. L. Smith, T. E. Schäffer, M. Viani, J. B. Thompson, N. A. Frederick, J. Kindt, A. Belcher, G. D. Stucky, D. E. Morse, P. K. Hansma, *Nature* **1999**, *399*, 761.
- [170] A. G. Evans, Z. Suo, R. Z. Wang, I. A. Aksay, M. Y. He, J. W. Hutchinson, *J. Mater. Res.* **2001**, *16*, 2475.
- [171] H. Gao, B. Ji, I. L. Jäger, E. Arzt, P. Fratzl, *Proc. Natl. Acad. Sci.* **2003**, *100*, 5597.
- [172] B. Ji, H. Gao, *J. Mech. Phys. Solids* **2004**, *52*, 1963.
- [173] K. Okumura, P.-G. de Gennes, *Eur. Phys. J. E* **2001**, *4*, 121.
- [174] G. Mayer, *Science* **2005**, *310*, 1144.
- [175] A. Sellinger, P. M. Weiss, A. Nguyen, Y. Lu, R. A. Assink, W. Gong, C. J. Brinker, *Nature* **1998**, *394*, 256.
- [176] Q. L. Feng, F. Z. Cui, G. Pu, R. Z. Wang, H. D. Li, *Mater. Sci. Eng. C* **2000**, *11*, 19.
- [177] S. M. Zhang, Y. J. Gao, Z. J. Zhang, H. X. Dang, W. M. Liu, Q. J. Xue, *Acta Chim. Sin.* **2002**, *60*, 1497.
- [178] X. Zhang, C. Liu, W. Wu, J. Wang, *Mater. Lett.* **2006**, *60*, 2086.
- [179] Ž. Burghard, A. Tucić, L. P. H. Jeurgens, R. C. Hoffmann, J. Bill, F. Aldinger, *Adv. Mater.* **2007**, *19*, 970.
- [180] J. L. He, W. Z. Li, H. D. Li, *Mater. Lett.* **1997**, *30*, 15.
- [181] Ž. Burghard, D. Schön, P. Gerstel, J. Bill, F. Aldinger, *Int. J. Mat. Res.* **2006**, *97*, 1667.
- [182] For an X-ray diffractogram of a monolithic ZnO film see Figure 4.5.
- [183] W. C. Oliver, G. M. Pharr, *J. Mater. Res.* **1992**, *7*, 1564.
- [184] W. D. Nix, *Mater. Sci. Eng. A* **1997**, *237*, 37.

- [185] J. Wang, W. Z. Li, H. D. Li, B. Shi, J. B. Luo, *Thin Solid Films* **2000**, *366*, 509.
- [186] J. S. Koehler, *Phys. Rev. B.* **1970**, *2*, 547.
- [187] M. Salomäki, T. Laiho, J. Kankare, *Macromolecules* **2004**, *37*, 9585.
- [188] L. P. Martin, D. Dadon, M. Rosen, *J. Am. Ceram. Soc.* **1996**, *79*, 1281.
- [189] S. H. Kim, Y. J. Baik, D. Kwon, *Surf. Coat. Technol.* **2004**, *187*, 47.
- [190] K. K. Chawla, *Composite Materials*, 2nd ed., Springer-Verlag, New York **1998**, pp. 305 – 308.
- [191] S. O. Kucheyev, J. E. Bradby, J. S. Williams, C. Jagadish, M. V. Swain, *Appl. Phys. Lett.* **2002**, *80*, 956.
- [192] M. J. Mayo, R. W. Siegel, Y. X. Liao, W. D. Nix, *J. Mater. Res.* **1992**, *7*, 973.
- [193] L. Zini, *Bioinspirierte Herstellung und mechanische Charakterisierung oxidkeramischer Schichten*, Diplomarbeit, Universität Stuttgart, Stuttgart **2007**.



## Curriculum vitae

<i>Name</i>	Peter Lipowsky
<i>Date of Birth</i>	11 <sup>th</sup> February 1981
<i>Place of Birth</i>	Erlangen
<i>School</i>	1987 – 1991 Volksschule Hepberg (Grundschule)
	1991 – 1999 Christoph-Scheiner-Gymnasium Ingolstadt
<i>Higher Education</i>	1999 – 2001 Physics at Technische Universität Dresden
	2001 – 2004 Physics at Technische Universität München
	since 2004 Doctoral candidate at Max-Planck-Institut für Metallforschung and Institut für Nichtmetallische Anorganische Materialien, Universität Stuttgart



## Danksagung

Die vorliegende Arbeit wurde am Max-Planck-Institut für Metallforschung und am Institut für Nichtmetallische Anorganische Materialien der Universität Stuttgart angefertigt.

Mein Dank gilt Herrn Prof. Dr. Fritz Aldinger für die Möglichkeit, diese Arbeit in seiner Abteilung durchzuführen, sowie für das Vertrauen, mich meine Ergebnisse bei den verschiedensten Gelegenheiten öffentlich präsentieren zu lassen.

Herrn Dr. Joachim Bill danke ich für die Übernahme des Mitberichts, für die hervorragende Betreuung und seine Offenheit für Fragen und Diskussionen. Auch Herrn Dr. Rudolf Hoffmann, der während der ersten Hälfte meiner Doktorandenzeit als Mitbetreuer wirkte, danke ich für die rege Anteilnahme am Fortgang der Arbeit und für wertvolle Anregungen.

Herrn Professor Dr. Ir. Eric J. Mittemeijer und Herrn Prof. Dr. Lennart Bergström danke ich für ihre Bereitschaft, als Prüfungsvorsitzender und Mitprüfer zur Verfügung zu stehen.

Herrn Prof. Dr. Lennart Bergström danke ich auch für seine Gastfreundschaft, die es mir ermöglichte, einen Teil dieser Arbeit in seinem Labor an der Universität Stockholm durchzuführen, und dafür, dass er meinen Blick auf neue Aspekte des untersuchten Systems gelenkt hat. Seinem Mitarbeiter Dr. Niklas Hedin danke ich für die gute Betreuung und für wertvolle Diskussionen während der Zeit in Stockholm.

Herrn Peter Gerstel möchte ich für die Beantwortung aller praktischen Fragen des Laboralltags und für seine unermüdliche Hilfsbereitschaft danken. Dankend erwähnt seien auch Frau Sabine Kühnemann, Herr Dr. Udo Welzel, Herr Gerd Maier, Frau Maritta Dudek, Herr Dr. Lars P. H. Jeurgens und Frau Michaela Wieland, die jeweils eine große Anzahl an Proben geduldig mikroskopiert bzw. gemessen haben. Ebenso danke ich allen anderen, die hier nicht namentlich Erwähnung finden können.

Schließlich gilt ein besonderer Dank meinen Eltern, Geschwistern und Anna für die Unterstützung, meinem Vater außerdem für sein fachliches Interesse und anregende Gespräche über das Thema.